RADON REMOVAL FROM GASEOUS XENON FOR THE ENRICHED XENON OBSERVATORY

by

Eric Beauchamp

A thesis submitted in partial fulfillment
of the requirements for the degree of
Master of Science (M.Sc.) in Physics

The School of Graduate Studies
Laurentian University
Sudbury, Ontario, Canada

THESIS DEFENCE COMMITTEE/COMITÉ DE SOUTENANCE DE THÈSE

Laurentian Université/Université Laurentienne
School of Graduate Studies/École des études supérieures

Title of Thesis Titre de la thèse	RADON REMOVAL FROM GASEOUS XENON FOR THE ENRICHED XENON OBSERVATORY
Name of Candidate Nom du candidat	Beauchamp, Eric
Degree Diplôme	Master of Science
Department/Program Département/Programme	Physics
Date of Defence Date de la soutenance	December 05, 2013

APPROVED/APPROUVÉ

Thesis Examiners/Examinateurs de thèse:

Dr. Jacques Farine
(Supervisor/Directeur de thèse)

Dr. Ubi Wichoski
(Committee member/Membre du comité)

Dr. Bruce Cleveland
(Committee member/Membre du comité)

Dr. Wolfgang Rau
(External Examiner/Examinateur externe)

Approved for the School of Graduate Studies
Approuvé pour l'École des études supérieures
Dr. David Lesbarrères
M. David Lesbarrères
Director, School of Graduate Studies
Directeur, École des études supérieures

ACCESSIBILITY CLAUSE AND PERMISSION TO USE

Abstract

Neutrino oscillation experiments have shown definite evidence for non-zero neutrino masses. However, these experiments only tell us about neutrino mass differences, and nothing about the absolute masses themselves. The observation of neutrinoless double-beta ($0\nu\beta\beta$) decay, a hypothetical nuclear transition, would provide the first absolute mass scale measurement of the neutrino outside of cosmology. This decay would imply the neutrino to be a Majorana particle, the first fermion of its kind. $0\nu\beta\beta$ decay would also be the first observation of lepton number violation. The Enriched Xenon Observatory (EXO) is currently searching for $0\nu\beta\beta$ decay in ^{136}Xe with a half-life greater than 10^{25} years.

EXO-200 is the first experiment of the EXO physics program, which has observed two-neutrino double beta decay ($2\nu\beta\beta$) in ^{136}Xe for the first time, with a half-life of $2.165 \pm 0.075 \times 10^{21}$ years [1]. This is the longest measured half-life to date. EXO is now designing a 5-tonne scale detector, nEXO, to be sensitive to the inverted-scale hierarchy. Despite the careful selection of radiopure substances for the detector, the existence of trace levels of ^{222}Rn is inevitable. One of the daughters of ^{222}Rn, ^{214}Bi, can emit photons at the Q-value for $0\nu\beta\beta$ decay, making it a critical background. This dissertation investigates the method of Rn removal from gaseous Xe through the use of a Cu wool trap.

Acknowledgements

Thank you to the members of EXO who are more of an extended family than a collaboration. You have made collaboration meetings and the multiple visits to Carlsbad much more fun than they ought to have been.

Thank you to the EXO Group at Laurentian. Brian, for your wisdom and entertaining all my questions. Dimpal, you are a source of inner strength and calmness that has prevented me from cracking more than once. Thank you especially to Jacques, for your patience and unabated enthusiasm. I hope other students will be so lucky to have you as a supervisor.

Thank you to my thesis committee and the Physics Department at Laurentian for your continued support, and providing me with the resources to pursue this endeavour.

Thank you to my parents. I would obviously not exist without you, but I would also certainly not have made it this far without your unwavering support. There are just not enough ways for me to repay you.

Nancy, Margo and Joe, thank you for tolerating me these past few years and indulging me with board games. I'm free to do the Algorithm Chores again. Nathalie, I still owe you a few rubber balls. The interest on them must be huge by now. Jeff and Beth, even if we move further apart, somehow I know we won't grow apart. This list is far from complete.

Contents

List of Figures

List of Tables

Chapter 1

Neutrinos

1.1 The Elusive Neutrino

Neutrinos have a long and complex history since their introduction in physics. Wolfgang Pauli first proposed the neutrino in 1929 to explain the continuous energy spectrum observed in beta decay by Sir James Chadwick in 1914. In a letter to a conference, Pauli wrote, "Dear Radioactive Ladies and Gentlemen, ... as a desperate remedy to save the principle of energy conservation in beta decay, ... I propose the idea of a neutral particle of spin half [2]". Pauli had originally dubbed his particle the "neutron", but the name was also used by Chadwick when he discovered a neutral baryon in 1932 [3]. To resolve the confusion, Enrico Fermi coined the term "neutrino" in 1933, which borrows from the Italian language to mean "little neutral one [4]". Neutrinos disturbed Pauli. He went on to say "I have done something very bad today by proposing a particle that cannot be detected; it is something no theorist should ever do [5]". In 1934, Enrico Fermi published the model of β-decay, invoking Pauli's

particle to conserve energy and momentum:

$$p \rightarrow n + e^{+} + \nu_e \tag{1.1a}$$

$$n \rightarrow p + e^{-} + \bar{\nu}_e \tag{1.1b}$$

However, the neutrino was still a hypothesis. The first suggestion for indirect detection of neutrinos came from Wang Kan Chang in 1942. Wang suggested measuring the recoil energy of a β^{+}-radioactive atom after it captures a K-shell electron and releases an electron antineutrino [6]. It wasn't until 1956, when the neutrino was detected by Frederick Reines and Clyde L. Cowan, albeit with a different detection principle [7]. This is known as the Reines-Cowan experiment. The experiment used a high antineutrino flux created through beta decay in a nuclear reactor near their detector. The antineutrinos were detected by inverse-beta decay on protons in a water tank:

$$\bar{\nu}_e + p \rightarrow n + e^{+} \tag{1.2}$$

The positron emitted is quickly annihilated by nearby electrons in the medium, producing two 0.51 MeV gamma rays travelling in opposite directions. A scintillator added in the water produces flashes of light from the interactions of the gammas, which can then be collected by photomultiplier tubes (PMTs). The neutron produced is captured by a strong neutron absorber, in this case cadmium, which was dissolved as cadmium chloride in the water. The neutron capture leaves the Cd atom in an excited state which de-excites and emits a few detectable photons totalling 9 MeV (1.3). The time constant between the photons from positron annihilation and photons from neutron capture is 5.5 μs, allowing for discrimination

of background events [8].

$$n + {}^{108}\mathrm{Cd} \rightarrow {}^{109}\mathrm{Cd}^{*} \rightarrow {}^{109}\mathrm{Cd} + \gamma \tag{1.3}$$

By 1962, another type, or "flavour", of neutrino had been discovered. A collaboration headed by Leon Lederman, Melvin Schwartz and Jack Steinberger at the Alternating Gradient Synchrotron (AGS) at Brookhaven National Laboratory used a 15 GeV proton beam striking a beryllium target to produce a pion beam, which then decays into neutrinos [9]. Pion decay occurs analogously to beta decay:

$$\pi^{+} \rightarrow \mu^{+} + \nu_{\mu} \tag{1.4a}$$

$$\pi^{-} \rightarrow \mu^{-} + \bar{\nu}_{\mu} \tag{1.4b}$$

The resulting particle beam was sent through a 13.5-m thick iron shield wall to absorb any strongly-interacting particles and allow only muons and neutrinos through to a 10-ton aluminum spark chamber filled with neon gas. The muons passed through aluminum plates and ionized the interleaving neon gas, causing discharges in the neon, which allowed the muon track to be visualized and photographed. The spark tracks were analysed and confirmed to be caused by muons from pion decay. More interestingly, some muon tracks began within the detector, without originating from the particle beam. This inferred the presence of a muon neutrino interacting with the detector medium and producing a muon through the charged current (CC) interaction. Through a CC interaction, a neutrino can weakly interact with the target quark to produce a charged lepton of the same flavour and a new quark. This mechanism will, for example, convert a neutron to a proton or vice versa. The CC

interaction is mediated by the $W^{\pm}$ boson:

$$\nu_l + d \xrightarrow{W^-} l^- + u \tag{1.5a}$$

$$\bar{\nu}_l + u \xrightarrow{W^+} l^+ + d, \quad l = e, \mu, \tau \tag{1.5b}$$

Following the discovery of the tau lepton in 1975, the existence of a third generation neutrino, the ν_τ, was postulated. The DONuT experiment at Fermilab set out to discover this neutrino by observing CC interactions (1.5) from a neutrino beam, and rejecting muons and electrons at the interaction vertex. The neutrino beam was first created by a 800 GeV proton beam from the Fermilab Tevatron [10], then passed through a tungsten beam dump to shield from other particles. Tau neutrinos were primarily the result of mesons containing charm quarks, decaying into τ and $\bar{\nu}_\tau$. After some magnets, metal shielding and a muon veto, the neutrinos propagated through an emulsion-scintillator target, which recorded the tracks of the charged leptons.

For the DONuT experiment, a neutron was converted to a proton, with a positive lepton emitted (1.5b). The emulsion-scintillator target produced tracks of these charged leptons. The τ being the shortest-lived lepton, it decayed within 2 mm of its creation to another charged lepton. The conversion of energy in τ-decay left a distinctive kink in its track, which could be further analysed along with branching ratios. In their final analysis, DONuT used 3.6×10^{17} protons to observe a total of 578 neutrinos, 9 of which were ν_τ CC events with an estimated 1.5 background events [11].

1.2 Solar Neutrinos

The Standard Solar Model (SSM) characterizes the reactions responsible for energy production in the core of the Sun, effectively through the fusion of hydrogen to helium. Neutrinos are a by-product of this hydrogen burning process. There are two dominating cycles, the "pp-chain" and the "CNO cycle". The pp-chain is composed of four sub-chains. The first sub-chain, named the "pp-I" chain is responsible for nearly 86% of neutrinos from the Sun [2] [12].

$$\begin{aligned} p + p &\rightarrow d + e^{+} + \nu_e && (\mathrm{E}_\nu \leq 0.420 \text{ MeV}) \\ p + e^{-} + p &\rightarrow d + \nu_e && (\mathrm{E}_\nu = 1.442 \text{ MeV}) \\ d + p &\rightarrow \gamma + {}^{3}\mathrm{He} \\ {}^{3}\mathrm{He} + {}^{3}\mathrm{He} &\rightarrow {}^{4}\mathrm{He} + p + p \end{aligned} \tag{1.6}$$

The ^{3}He produced above fuels the next two sub-chains. The first of them, the "hep" chain, only contributes $\sim 10^{-7}$ % of the neutrino flux.

$${}^{3}\mathrm{He} + p \rightarrow {}^{4}\mathrm{He} + e^{+} + \nu_e \qquad (\mathrm{E}_\nu \leq 18.77 \text{ MeV}) \tag{1.7}$$

The second sub-chain following the pp-I is the "pp-II" chain, which produces about 14% of the solar neutrino flux.

$$
\begin{aligned}
{}^3\mathrm{He} + {}^4\mathrm{He} &\rightarrow {}^7\mathrm{Be} + \gamma \\
{}^7\mathrm{Be} + e^- &\rightarrow {}^7\mathrm{Li} + \nu_e \qquad (\mathrm{E}_\nu = 0.861\ \mathrm{MeV}[90\%], 0.303\ \mathrm{MeV}[10\%]) \\
{}^7\mathrm{Li} + p &\rightarrow {}^4\mathrm{He} + {}^4\mathrm{He}
\end{aligned} \tag{1.8}
$$

The last subchain in the pp-chain contributes $1.5 \times 10^{-4}\%$ of the neutrino flux and is called the "pp-III" chain. This small proportion may seem dwarfed by the rest of the neutrino production cycles, but these neutrinos are of direct interest for solar neutrino detection experiments such as the Kamiokande experiment and Homestake experiment. The pp-III chain is supplied by ^{7}Be from the pp-II chain as follows:

$$
\begin{aligned}
{}^7\mathrm{Be} + p &\rightarrow {}^8\mathrm{B} + \gamma \\
{}^8\mathrm{B} &\rightarrow {}^8\mathrm{Be}^* + e^+ + \nu_e \qquad (\mathrm{E}_\nu \leq 14.06\ \mathrm{MeV}) \\
{}^8\mathrm{Be}^* &\rightarrow {}^4\mathrm{He} + {}^4\mathrm{He}
\end{aligned} \tag{1.9}
$$

The second major neutrino-production mechanism is the CNO cycle, so named for requiring carbon, nitrogen and oxygen as catalysts. This cycle dominates over the pp-chain in hotter, more massive stars, but for the Sun it only contributes 1.5% of the total neutrino flux.

$$
\begin{aligned}
&{}^{12}\mathrm{C} + p \rightarrow {}^{13}\mathrm{N} + \gamma \\
&\quad {}^{13}\mathrm{N} \rightarrow {}^{13}\mathrm{C} + e^{+} + \nu_e \qquad (\mathrm{E}_\nu \leq 1.2 \text{ MeV}) \\
&{}^{13}\mathrm{C} + p \rightarrow {}^{14}\mathrm{N} + \gamma \\
&{}^{14}\mathrm{N} + p \rightarrow {}^{15}\mathrm{O} + \gamma \\
&\quad {}^{15}\mathrm{O} \rightarrow {}^{15}\mathrm{N} + e^{+} + \nu_e \qquad (\mathrm{E}_\nu \leq 1.73 \text{ MeV}) \\
&{}^{15}\mathrm{N} + p \rightarrow {}^{12}\mathrm{C} + \alpha \\
&{}^{15}\mathrm{N} + p \rightarrow {}^{16}\mathrm{O} + \gamma \\
&{}^{16}\mathrm{O} + p \rightarrow {}^{17}\mathrm{F} + \gamma \\
&\quad {}^{17}\mathrm{F} \rightarrow {}^{17}\mathrm{O} + e^{+} + \nu_e \qquad (\mathrm{E}_\nu \leq 1.74 \text{ MeV}) \\
&{}^{17}\mathrm{O} + p \rightarrow {}^{14}\mathrm{N} + \alpha
\end{aligned} \tag{1.10}
$$

The low interaction cross-sections of neutrinos make them the only reaction products of the SSM that can be directly observed on Earth. Atoms remain in the solar core and photons are persistently absorbed and re-emitted before they escape the surface ∼170,000 years after their creation [14]. The detection of solar neutrinos is the only method that can directly prove the mechanism that powers the stars.

1.3 The Solar Neutrino Problem

The first experiment to detect solar neutrinos, led by Ray Davis Jr., began in the late 1960s [15]. The detector was located underground at the Homestake Gold Mine in South Dakota, using a 100,000 gallon tank of perchloroethylene (C_2Cl_4) as a target. Interaction with neutrinos were made possible by inverse beta-decay:

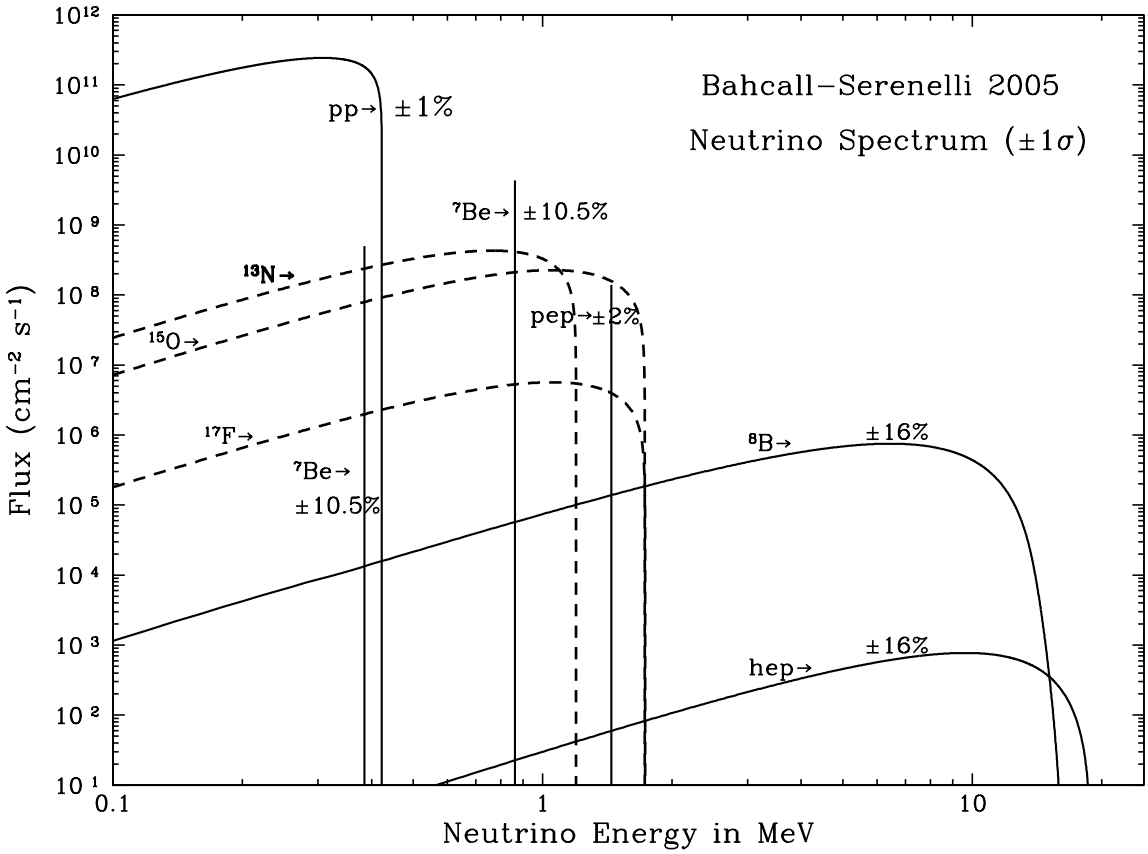

Figure 1.1: Solar neutrino spectrum on Earth's surface according to the Bahcall and Serenelli Standard Solar Model of 2005 [13]. Flux units for continuous distributions are actually in $\mathrm{cm}^{-2}\ \mathrm{s}^{-1}\ \mathrm{MeV}^{-1}$.

$$\begin{aligned} \nu_e + {}^{37}\mathrm{Cl} &\rightarrow e^- + {}^{37}\mathrm{Ar}^* \\ {}^{37}\mathrm{Ar}^* &\rightarrow {}^{37}\mathrm{Ar} + \gamma \end{aligned} \tag{1.11}$$

Radioactive ^{37}Ar was periodically collected from the tank and its activity measured, allowing to determine a solar neutrino flux rate. The Homestake experiment measured

a solar neutrino flux rate consistently at one third of what was expected from flux rate calculations predicted by John N. Bahcall [13] (among others). This neutrino deficit came to be known as the "Solar Neutrino Problem".

Other solar neutrino experiments were conducted and each one found a similar neutrino deficit, despite using different experimental techniques. Two experiments running through the 1990s, SAGE and GALLEX, detected solar neutrinos from inverse beta decay of gallium:

$$\nu_e + {}^{71}\mathrm{Ga} \rightarrow e^- + {}^{71}\mathrm{Ge}^* \tag{1.12}$$

The germanium product was extracted from gallium and counted. Gallium is sensitive to each neutrino-producing reaction of the SSM due to a lower energy threshold, an improvement over chlorine (233 keV vs. 814 keV, respectively). The SAGE collaboration measured a neutrino capture rate of $65.4^{+5.7}_{-5.8}$ Solar Neutrino Units (SNU, or $\times 10^{-36}$ captures per target atom per second) [16], similar to GALLEX who measured $77.5^{+10.5}_{-10.9}$ SNU [17]. GALLEX's successor, the Gallium Neutrino Observatory (GNO), measured 65.2 ± 9.4 SNU [18]. All of these experiments were in agreement with each other, yet consistently short of the SSM prediction of 129^{+8}_{-6} SNU for ^{71}Ga.

The Kamiokande experiment was the first in a series of Cherenkov detectors, using a different technique to detect neutrinos. The detector material was water. Neutrinos entering the detector scattered off of electrons in the hydrogen and oxygen atoms. Since the neutrinos have energies in the MeV range, the atomic binding energies are negligible and the scattering can be treated as elastic scattering (ES) of neutrinos off free electrons:

$$\nu_l + e^- \rightarrow \nu_l + e^-, \quad l = e, \mu, \tau \qquad \text{(ES)} \tag{1.13}$$

Following some ES interactions, the scattered electron's speed, v, will exceed the speed

of light in the medium, c/n, where n is the refractive index in the medium. When a charged particle exceeds the speed of light in a medium, the charged particle emits a cone of photons, called Cherenkov radiation. This radiation is analogous to the shock wave and associated "sonic boom" created by objects travelling at supersonic speeds. The Cherenkov light cone will be seen as a ring during consecutive instances of time in a Cherenkov detector. The Cherenkov angle, θ_C, is the angle of emission of the Cherenkov light from the path of the charged particle,

$$\cos\theta_C = \frac{c}{vn} \tag{1.14}$$

The Cherenkov method posed a great advantage for Kamiokande in terms of signal reconstruction. After a neutrino ES event, a ring of light was detected by the ∼1,000 PMTs attached along the inside walls of the 3-kton, cylindrical water tank. The observed Cherenkov rings can be fit for which point the ES interaction is most likely to have occurred, with the added benefit of directionality. Thus, it could be determined on a statistical basis whether or not the neutrino flux came from the Sun. Their result confirmed the Solar Neutrino Problem with a measured neutrino flux $45.1^{+2.1}_{-1.9}$ % of the calculated SSM prediction [19].

In a following Kamiokande experiment, the Super-K detector began observing solar and atmospheric neutrinos in 1998. Super-K was a larger scaled version of its predecessor, now with 50 ktons of water and 11,146 PMTs. The collaboration found their observations of atmospheric neutrinos consistent with the prediction from two-flavour oscillation: $\nu_\mu \leftrightarrow \nu_\tau$ [20]. This was the first evidence of neutrino oscillations, a process which would apply to solar neutrinos as well. While previous experiments until now had observed the solar neutrino deficit, it was unclear whether the Standard Solar Model was in need of correction, or the Standard Model neutrino.

It took a few more years until 2001, when the Sudbury Neutrino Observatory (SNO) in Canada discovered that oscillations are also the explanation of the Solar Neutrino Problem [21]. The SNO detector used heavy water (D_2O) as its target. The advantage of D_2O was the possibility of detecting neutrinos by three mechanisms, each with a different dependence on the flavour composition of the neutrino flux. Just like Kamiokande, SNO detected neutrinos by Cherenkov radiation via the ES interaction (1.13). The other two interactions were made possible by the presence of the deuteron nucleus. First, an incoming neutrino could undergo a charged current (CC) interaction, with a mediating W^- boson:

$$\nu_e + \mathrm{D} \xrightarrow{\mathrm{W}^-} p + p + e^- \qquad \text{(CC)} \tag{1.15}$$

The resulting electron was detected by Cherenkov radiation. Second, the incoming neutrino could interact by a neutral current (NC) interaction, mediated by the Z^0 boson:

$$\nu_l + \mathrm{D} \xrightarrow{\mathrm{Z}^0} \nu_l + n + p, \quad l = e, \mu, \tau \quad \text{(NC)} \tag{1.16}$$

The emitted neutron was captured on deuterium, emitting 6.25 MeV γ rays, which were detectable via Cherenkov radiation. Notice how the CC interaction (1.15) is only sensitive to the ν_e, whereas the ES and NC interactions (1.13, 1.16) allow the detection of all three flavours of neutrinos. Not only this, but the ES interaction has a different cross-section for ν_e and $\nu_{\mu,\tau}$, whereas the NC interaction has equal cross-section for all flavours, due to there being no charged lepton product. This made direct comparison of the neutrino flux contents possible between the three different channels, all on the same data set from the same detector.

The first results from SNO in 2001 [21] reported neutrino fluxes from two of these reactions, the ES and CC reactions. Although earlier experiments had already measured these

fluxes by the same channels, none of them have been able to use both channels in the same experiment. For SNO, this meant being able to directly compare the results from each channel. The fact that SNO had a flux measurement from two different channels, one sensitive to $\nu_{\mu,\tau}$ and the other not, meant that a $\nu_{\mu,\tau}$ component in the total neutrino flux could be deduced.

The second SNO result [22] added new information about the NC channel. Using rates from each reaction channel, they reported an electron neutrino flux of $\phi_{\mathrm{e}} = 1.76 \pm 0.14 \times 10^6$ cm^{-2} s^{-1} and a non-electron neutrino flux of $\phi_{\mu,\tau} = 3.41 \pm 0.90 \times 10^6$ cm^{-2} s^{-1}.

Moreover, the total flux measurement from the NC channel was completely consistent with the SSM predictions. This led to the conclusion that neutrino oscillations are the explanation and solution for the solar neutrino problem. As outlined in Section 1.2, neutrinos are only created as ν_e in the Sun. However, during a neutrino's journey from the Sun to the Earth, it transforms flavours and causes an apparent disappearance of ν_e on Earth. As will be shown in the next section, neutrino oscillations require neutrinos to be massive, a finding which was not included in the Standard Model of particle physics.

1.4 Neutrino Oscillations

The concept of neutrinos converting from one type to another, named "oscillation", was suggested by Bruno Pontecorvo [23][24]. Pontecorvo thought of neutrino oscillation as analogous to the neutral kaon oscillation ($\mathrm{K}^0 \leftrightarrow \bar{\mathrm{K}}^0$) and proposed to test his hypothesis with solar neutrinos [25]. Neutrinos can be represented as three mass eigenstates, $|\nu_1\rangle$, $|\nu_2\rangle$, $|\nu_3\rangle$, which are also related to the three weak eigenstates, $|\nu_e\rangle$, $|\nu_\mu\rangle$, $|\nu_\tau\rangle$. They are related to each other via a unitary matrix, $U_{\alpha i}$, known as the Pontecorvo-Maki-Nakagawa-Sakata (PMNS) matrix [2]:

$$|\nu_\alpha\rangle = \sum_i U_{\alpha i}|\nu_i\rangle \tag{1.17a}$$

$$|\nu_i\rangle = \sum_\alpha U^*_{\alpha i}|\nu_\alpha\rangle \tag{1.17b}$$

where α indexes the flavour eigenstates, $\alpha = e, \mu, \tau$, and i indexes the mass eigenstates, $i = 1, 2, 3$.

The PMNS matrix is so named for its introduction in 1962 by Maki, Nakagawa, and Sakata [26] to describe Pontecorvo's idea of neutrino oscillations. A parameterized form of the PMNS matrix is as follows:

$$U = \begin{pmatrix} 1 & 0 & 0 \\ 0 & c_{23} & s_{23} \\ 0 & -s_{23} & c_{23} \end{pmatrix} \begin{pmatrix} c_{13} & 0 & s_{13}e^{-i\delta_{\mathrm{CP}}} \\ 0 & 1 & 0 \\ -s_{13}e^{i\delta_{\mathrm{CP}}} & 0 & c_{13} \end{pmatrix} \begin{pmatrix} c_{12} & s_{12} & 0 \\ -s_{12} & c_{12} & 0 \\ 0 & 0 & 1 \end{pmatrix} \tag{1.18}$$

where $c_{ij} \equiv \cos\theta_{ij}$ and $s_{ij} \equiv \sin\theta_{ij}$, δ_{CP} is non-zero if neutrino oscillations violate CP symmetry, and θ_{ij} are the mixing angles between the i and jth eigenstates.

If we assume for simplicity that the momentum, $\vec{p}$, associated with each of the three mass components are equal in the initial flavour eigenstate, and we know the masses are different, then so would the energies, E_i, of each mass component. The relativistic energy-momentum relation can be applied with the assumption that neutrinos are ultra-relativistic, $|\vec{p}_i^{\,2}| = p_i \gg m_i$, and natural units $c = \hbar = 1$ for convenience. Therefore,

$$E_i = \sqrt{p_i^2 + m_i^2} \simeq p_i + \frac{m_i^2}{2p_i} \tag{1.19}$$

After applying the time evolution operator using E_i, our wavefunction describing the neutrino flavour eigenstates becomes as follows:

$$|\nu_\alpha(t)\rangle = \sum_i e^{-iE_i t} U_{\alpha i} |\nu_i\rangle \tag{1.20}$$

It's easier to see from (1.19) and (1.20) how the flavour eigenstate begins to change in proportion of mass eigenstates as it propagates over time. The probability of starting with a neutrino of flavour α and finding a neutrino of flavour β afterwards can be calculated:

$$\begin{aligned} P_{\nu_\alpha \to \nu_\beta}(t) &= |\langle \nu_\beta | \nu_\alpha(t) \rangle|^2 \\ &= \left| \sum_{\beta=e,\mu,\tau} \sum_i^3 \langle \nu_\beta | U^*_{\beta i} e^{-iE_i t} U_{\alpha i} | \nu_\beta \rangle \right|^2 \\ &= \left| \sum_i^3 e^{-iE_i t} U_{\alpha i} U^*_{\beta i} \right|^2 \end{aligned} \tag{1.21}$$

The neutrino is purely composed of one flavour α at $t = 0$, but after $t > 0$, the state can be a superposition of different flavours. Expanding (1.21) produces the most general form of probability of oscillation at any time t:

$$P_{\nu_\alpha \to \nu_\beta}(t) = \sum_{i,j} |U_{\alpha\beta ij}| \cos\left[(E_\alpha - E_\beta)t - \arg(U_{\alpha\beta ij})\right] \tag{1.22}$$

where $U_{\alpha\beta ij} \equiv U_{\alpha i} U^*_{\beta i} U^*_{\alpha j} U_{\beta j}$. The probability for a neutrino to oscillate after travelling a distance x is:

$$P_{\nu_\alpha \to \nu_\beta}(x) = \sum_{i,j} |U_{\alpha\beta ij}| \cos\left(\frac{\Delta m^2_{ij}}{2E} x - \arg(U_{\alpha\beta ij})\right) \tag{1.23}$$

where $\Delta m^2_{ij} \equiv m^2_i - m^2_j$. It is sometimes sufficient to consider a system where there are only two oscillating neutrinos, due to θ_{13} being very small. In Daya Bay's proposal for the measurement of θ_{13} [27], the Daya-Bay Collaboration makes a very close approximation by only considering the case of an electron antineutrino oscillating to a superposition of muon and tau antineutrinos ($\bar{\nu}_e \to \bar{\nu}_{\mu,\tau}$; this can also be regarded as simply $\bar{\nu}_e$ disappearance). However, it should be noted that Daya Bay goes on to treat the problem as a three-state system for completeness. The two-neutrino case reduces the PMNS matrix (1.18) to a simple 2×2 unitary matrix:

$$U = \begin{pmatrix} \cos\theta & \sin\theta \\ -\sin\theta & \cos\theta \end{pmatrix} \tag{1.24}$$

The probability of oscillation (1.23) can be reduced to one of two probabilities: that the measured neutrino has *survived*, remaining the same as when it started ($P_{\text{surv}}(x)$); or the neutrino has *converted*, since it is measured as another flavour ($P_{\text{conv}}(x)$).

$$P_{\text{conv}}(x) = \sin^2 2\theta \sin^2\left(\frac{\Delta m^2}{4E}x\right) \tag{1.25a}$$

$$P_{\text{surv}}(x) = 1 - P_{\text{conv}}(x) \tag{1.25b}$$

There are some important points to make from these oscillation probabilities (1.23, 1.25). First, if neutrinos did not have differing masses, flavour oscillations would not occur. Second, any neutrino oscillation experiment will only ever measure a squared mass difference, Δm^2_{ij}, between any two neutrino mass eigenstates. This probability does not give a measurement for the absolute mass scale of the neutrino on its own.

1.5 The Absolute Mass Scale

Despite the successes of neutrino oscillation experiments, little is known of the absolute masses of the neutrinos.

The order in which these mass eigenstates are arranged are known as the mass hierarchy. There are three viable mass hierarchy models:

$$\begin{aligned} \text{normal} &: m_1 \sim m_2 \ll m_3 \\ \text{inverted} &: m_3 \ll m_1 \sim m_2 \\ \text{degenerate} &: m_1 \sim m_2 \sim m_3 \end{aligned}$$

Certain processes such as β-decay, cosmological structures, and neutrinoless double beta decay ($0\nu\beta\beta$) can tell us which arrangement the neutrinos follow.

The β-decay of tritium (^{3}H) is one of the most direct attempts to measure the mass of $\bar{\nu}_e$. This is done by measuring the spectrum of electrons near the end point of the ^{3}H β-decay spectrum. The most stringent upper bound to date was set by the Troitsk experiment, combined with a result from the Mainz experiment: $m_{\bar{\nu}_e} < 2.05$ eV at 95% CL [28]. The KATRIN experiment plans to improve this result and achieve a better sensitivity by an order of magnitude [29].

Cosmological observations, such as the distribution of galaxies and the Cosmic Microwave Background (CMB) from WMAP and Planck, put an upper limit on the sum of neutrino masses in order to have structure formation in the early Universe: $\sum m_\nu < 0.17$eV at 95% CL [30], although this limit is highly model-dependent and perhaps not the most reliable [31].

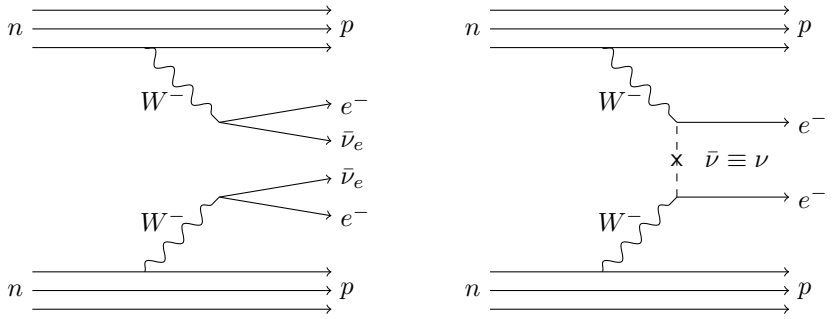

(a) $2\nu\beta\beta$ decay (b) $0\nu\beta\beta$ decay

Figure 1.2: Feynman diagrams of both $\beta\beta$-decay modes, which gives a prescription for calculating the differential cross section, $\frac{d\sigma}{d\Omega}$.

1.6 Double-Beta Decay

Double-beta decay is a second-order electroweak process where a nucleus with charge Z decays to a nucleus with charge $Z + 2$ while the mass number A remains the same. Two electrons are emitted, and either two neutrinos are emitted or none at all. These two modes are called two neutrino double-beta decay ($2\nu\beta\beta$) and neutrinoless, or zero-neutrino, double-beta decay ($0\nu\beta\beta$), respectively. Both processes are illustrated in Figure 1.2 and described here:

$$(A, Z) \rightarrow (A, Z + 2) + 2e^- + 2\bar{\nu}_e \tag{1.26a}$$

$$(A, Z) \rightarrow (A, Z + 2) + 2e^- \tag{1.26b}$$

Both $\beta\beta$-decay processes involve the conversion of two d quarks to two u quarks mediated by two W^- bosons. Thus, two neutrons become two protons, and each W^- boson decays to an electron and an $\bar{\nu}_e$. In the special case of $0\nu\beta\beta$, the antineutrino emitted from one

nucleon is absorbed as a neutrino by the other nucleon.

It is possible to detect $2\nu\beta\beta$ in certain even-even nuclei, for which pairing forces make the isotope's ground state energy more stable than if it were to single β-decay (see Figure 1.3). If the β-decay binding energy is higher than the ground state, β-decay is forbidden. In this case, only $\beta\beta$-decay is allowed. $2\nu\beta\beta$ decay makes for isotopes with half-lives upwards of 10^{21} years.[1]

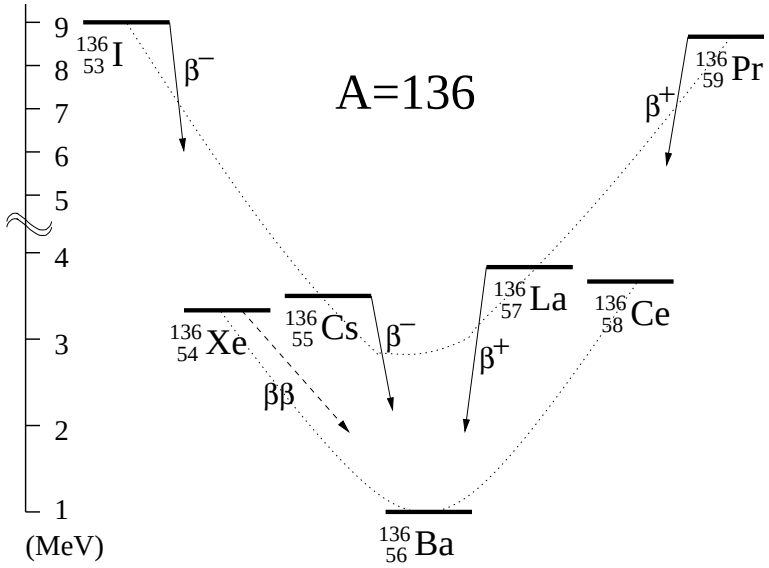

Figure 1.3: Mass parabolae for isobars of A=136. Notice that the ground state energy of ^{136}Cs is higher than that of ^{136}Xe, making it impossible for ^{136}Xe to simply β-decay (Figure obtained from [32]).

If the neutrino is a Majorana particle ($\nu \equiv \bar{\nu}$), and is massive, then $0\nu\beta\beta$ is also possible for a fraction of these $\beta\beta$-decays. In $0\nu\beta\beta$, all the energy released is transferred to the emitted electrons, as opposed to $2\nu\beta\beta$, where some energy is shared with neutrinos. Measuring the energy spectrum of the released electrons can therefore show a continuous $2\nu\beta\beta$ spectrum, along with a peak at the endpoint for $0\nu\beta\beta$ (Figure 1.4). The decay energy is known as the

[1]For perspective, these half-lives are order of billions of times the age of the universe.

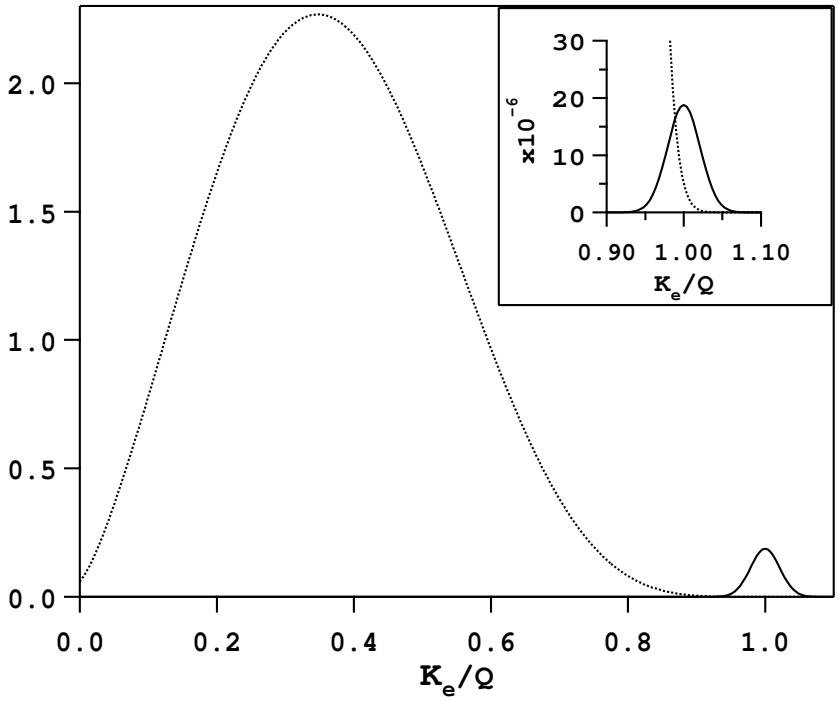

Figure 1.4: Spectrum of the sum of K_e, the electron energies normalized to the $Q_{\beta\beta}$-value. The dotted line represents $2\nu\beta\beta$ and the solid line represents $0\nu\beta\beta$. Both spectra are convoluted with an energy resolution of 5%. The 0ν mode is normalized to 10^{-2} in the main window and 10^{-6} in the inset, which illustrates how $2\nu\beta\beta$ constitutes a background for $0\nu\beta\beta$ (Figure obtained from [33]).

Q-value, which is $Q_{\beta\beta}$= 2457.83 $\pm$ 0.37keV for ^{136}Xe [34]. Obtaining a measurement of the $0\nu\beta\beta$ half-life would tell us the effective neutrino mass given by the following relation:

$$\left(T^{0\nu}_{1/2}\right)^{-1} = G^{0\nu} \cdot \left|M^{0\nu}\right|^2 \cdot \langle m_{\beta\beta}\rangle^2, \quad \text{where} \quad \langle m_{\beta\beta}\rangle^2 = \left|\sum_i U^2_{\alpha i} m_{\nu_i}\right|^2 \tag{1.27}$$

where $G^{0\nu}$ is the phase space factor and can be precisely calculated depending on the Q-value and nuclear charge, and $M^{0\nu}$ is the nuclear matrix element (NME) which carries some uncertainty. Comparison between nuclear models shows a factor $\sim$2 spread in the calculated NMEs [35]. $\langle m_{\beta\beta}\rangle$ is the effective Majorana mass which relates to the $0\nu\beta\beta$ half-life. It

contains the sum of complex CP-phases in U (1.18). The value of $\langle m_{\beta\beta} \rangle$ is constrained by double-beta decay experiments, and the absolute mass of the lightest neutrino is constrained by cosmological observations. Figure 1.5 demonstrates how the effective Majorana mass relates to the absolute mass of the lightest neutrino, along with current imposed limits.

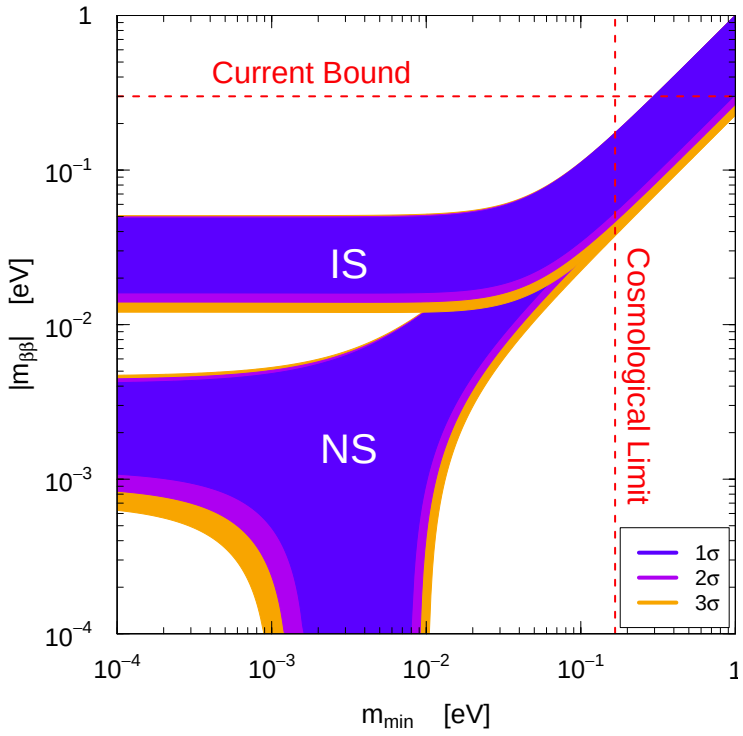

Figure 1.5: The effective Majorana mass $\langle m_{\beta\beta} \rangle$ as a function of the absolute mass of the lightest neutrino for the normal (NS, $m_{\text{min}} = m_1$) and inverted (IS, $m_{\text{min}} = m_3$) mass scale hierarchy. The bands of uncertainty reflect uncertainties on oscillation parameters (Figure obtained from [36]).

1.6.1 Experimental Endeavours

There are 35 known isotopes that can undergo $\beta\beta$-decay. Only 11 of these isotopes have a $Q_{\beta\beta}$-value greater than 2000 keV. Of these isotopes, 9 have now been observed to $\beta\beta$-decay by the 2ν mode (see Table 1.1). The challenge now lies in searching for a $0\nu\beta\beta$ signal, by

Isotope	$T_{1/2}^{2\nu\beta\beta}$(years)	Method	Experiment
^{48}Ca	$(4.4^{+0.5}_{-0.4} \pm 0.4) \times 10^{19}$	T & C	NEMO-3
^{76}Ge	$(1.74 \pm 0.01^{+0.18}_{-0.16}) \times 10^{21}$	Enriched HPGe	Heidelberg-Moscow[2]
^{82}Se	$(9.6 \pm 0.3 \pm 1.0) \times 10^{19}$	T & C	NEMO-3
^{96}Zr	$(2.35 \pm 0.14 \pm 0.16) \times 10^{19}$	T & C	NEMO-3
^{100}Mo	$(7.11 \pm 0.02 \pm 0.54) \times 10^{18}$	T & C	NEMO-3
^{116}Cd	$(2.8 \pm 0.1 \pm 0.3) \times 10^{19}$	T & C	NEMO-3
^{130}Te	$(7.0 \pm 0.9 \pm 1.1) \times 10^{20}$	T & C	NEMO-3
^{136}Xe	$(2.165 \pm 0.016 \pm 0.058) \times 10^{21}$	Liquid Xe scintillator	EXO-200 [1]
^{150}Nd	$(9.11^{+0.25}_{-0.22} \pm 0.63) \times 10^{18}$	T & C	NEMO-3

Table 1.1: $2\nu\beta\beta$ half-life measurements, all sourced from [35] except for [1]. T is abbreviated for "tracking", and C for "calorimetry".

increasing detector sizes, run times and signal resolution, while simultaneously minimizing background rates (cosmic rays, radioactive impurities, and the $2\nu\beta\beta$ signal itself).

In 2001, The Heidelberg-Moscow Collaboration placed a lower limit on the $T_{1/2}^{0\nu\beta\beta}$ using a 71.7 kg·years exposure of ^{76}Ge [37]. Meanwhile using the same dataset, Klapdor-Kleingrothaus et al. (a subset of the Heidelberg-Moscow Collaboration) made a claim for the discovery of $0\nu\beta\beta$ [38]. The authors substantiated their analysis on an observed peak in the energy spectrum, caused by 11 events near the Q-value. This claim has drawn a lot of criticism, with several concerns raised regarding the analysis method [39][40]. This lead one of the authors to retract [41]. Further analyses have strengthened the authors' confidence that they have observed $0\nu\beta\beta$ for an effective neutrino mass of $\langle m_{\beta\beta} \rangle = 0.32 \pm 0.03$ eV with more than 6σ certainty [42].

[2]Reanalysis of Heidelberg-Moscow data by Klapdor-Kleingrothaus and Dörr [43].

Regardless of the validity of the claim, an independent experiment should be carried out with the same isotope to reproduce the results. The first $0\nu\beta\beta$ results from GERDA in 2013 present a limit of $T_{1/2}^{0\nu\beta\beta} > 2.1 \times 10^{25}$ years (90 % C.L.), rejecting the Klapdor-Kleingrothaus et al. claim with a confidence of 90 % [44]. The first $0\nu\beta\beta$ limit from the EXO-200 detector, which was measured in 2011, also excludes the discovery claim at 68% CL. (90% CL.) for all (most) nuclear matrix element calculations [45]. EXO will be further discussed in Chapter 2.

Several experiments are increasing their sensitivities in order to potentially discover $0\nu\beta\beta$. A summary of half-life limits is listed in Table 1.2.

1.6.2 Implications of Discovery

No elementary fermion has yet been observed to exhibit the properties of a Majorana particle. That is, a fermion which acts as its own antiparticle. If $0\nu\beta\beta$ is observed, it would prove that $\nu \equiv \bar{\nu}$, the first fermion with a Majorana mass term. Seeing $0\nu\beta\beta$ would also mean that the total lepton number is not a conserved quantity. Also from (1.27), we would be able to measure the effective neutrino mass.

Isotope	$T_{1/2}^{0\nu\beta\beta}(10^{21}$ years)	Method	Experiment
^{48}Ca	> 58	CaF_2 scintillator	ELEGANT VI
^{64}Zn	> 0.22	$ZnWO_4$ scintillator	DAMA-INR
^{76}Ge	> 21000	Enriched HPGe	GERDA [44]
^{82}Se	> 360	T & C	NEMO-3
^{96}Zr	> 9.2	T & C	NEMO-3
^{100}Mo	> 1100	T & C	NEMO-3
^{112}Sn	> 1.06	γ Ge detector	Modane Underground Laboratory
^{116}Cd	> 170	$^{116}CdWO_4$ scintillator	Solotvina Underground Laboratory
^{128}Te	> 110	Cryogenic calorimeter	Precursor to CUORICINO
^{130}Te	> 3000	TeO_2 bolometer	CUORICINO
^{136}Xe	> 16000	Liquid Xe TPC	EXO-200 [45]
^{136}Xe	> 19000	Liquid Xe scintillator	KamLAND-Zen [46]
^{136}Xe	> 34000	Liquid Xe scintillator	EXO-200/KZ Combined [46]
^{150}Nd	> 18.0	T & C	NEMO-3
^{160}Gd	> 1.3	Gd_2SiO_5:Ce	Solotvina Underground Laboratory
^{186}W	> 1.1	$CdWO_4$ scintillator	Solotvina Underground Laboratory

Table 1.2: The most competitive limits of $0\nu\beta\beta$ half-lives [35]. T = tracking, C = calorimetry.

Chapter 2

The Enriched Xenon Observatory

^{136}Xe is an attractive isotope for the search for $0\nu\beta\beta$. Its high Q-value is at an energy relatively low in naturally-occurring radioactive backgrounds. The Enriched Xenon Observatory (EXO) is a broad program aimed at building an enriched Xe experiment to detect $0\nu\beta\beta$ in one or more tons of ^{136}Xe. The EXO Collaboration is composed of about 100 researchers from 19 institutions in 7 nations. EXO-200 is the first experimental phase of the EXO program. It is a prototype experiment located at the Waste Isolation Pilot Plant (WIPP) near Carlsbad, New Mexico, with a 200-kg stockpile of liquid xenon enriched to 80.6% in ^{136}Xe. The EXO Collaboration is also planning the next-generation detector, nEXO, which aims at reaching sensitivities on the order of $\langle m_{\beta\beta} \rangle \approx 10$ to 15 meV. Such a low sensitivity would effectively confirm or rule out the inverted mass scale hierarchy (Figure 1.5).

2.1 Detection of Double Beta Decay with Liquid Xenon

There are several benefits to a detector with liquid xenon (LXe) such as EXO-200:

- Isotopic enrichment is relatively easy. Since xenon is a gas a room temperature, it can

be enriched by gas centrifuge without involving any chemistry.

- Xenon is transferable and reusable. Samples of xenon can be taken for testing. The entire volume of gas can be recovered and reused in a larger scale detector.

- Xenon is scalable. Most other $\beta\beta$-decay candidates (such as ^{76}Ge and ^{130}Te) are limited in their size because they require the growth of crystals. Xenon can be deployed in a large, monolithic detector, taking advantage of self-shielding, though this also increases photon attenuation.

- Since it is a gas at room temperature, and easily condensed to a liquid, xenon can be purified continuously and *in situ*.

- Xenon cannot be cosmogenically activated to produce any long-lived isotopes, though the shorter-lived ^{137}Xe ($T_{1/2} = 3.8$ min) can be created.

- Any external background can be excluded through the use of barium daughter tagging. Either $\beta\beta$-decay mode produces a daughter Ba ion which could be identified on an event-by-event basis. If this were the case, only the $2\nu\beta\beta$ signal would remain as a background.

- A known correlation between scintillation and ionization in xenon can be exploited to improve energy resolution [47].

The main disadvantage of a liquefied noble gas detector compared to a crystalline detector is the energy resolution. For example, other $\beta\beta$-decay experiments using Ge and Te crystals have shown an energy resolution of order $\sigma/E \sim 0.1\%$ [48] [49]. An earlier LXe search for $0\nu\beta\beta$ measured scintillation light only and observed $\sigma/E \sim 8.4\%$ at the Q-value [50]. EXO-200 has addressed the issue of resolution by recording both scintillation and ionization

signals, combining them, and improving the resolution to $\sigma/E = 1.67\%$ [45]. While this is not as good as the best detectors, the EXO-200 detector is very competitive in the search for $0\nu\beta\beta$, by making use of further background reduction and rejection, and the other reasons discussed above.

2.2 EXO-200

The EXO-200 experiment is a prototype detector, a first iteration in preparation for a larger-scale detector that can improve sensitivity to the effective Majorana mass. It is the first phase in the EXO program, and it has already led to some world-leading results: the 2011 observation of $2\nu\beta\beta$ in ^{136}Xe [51], the most competitive limit for $0\nu\beta\beta$ in the summer of 2012 [45], and the most precisely measured half-life of all $2\nu\beta\beta$ decays [1].

The EXO-200 detector is composed of a TPC divided into two nearly identical, cylindrical drift regions. There is one cathode grid held at negative high voltage in the centre of the two halves. Each half of the TPC (Figure 2.1) records the ionization and scintillation signals at the base of the cylinder. Ionization is measured from electrons drifting from the cathode until they are collected on two sets of wire planes, each virtually grounded, and rotated at 60° with respect to each other. At the end of each TPC half, scintillation light is measured with an array of large area avalanche photodiodes (LAAPDs) behind both charge collection wires. Polytetrafluoroethylene (PTFE or Teflon®) tiles along the TPC walls reflect photons to the TPC ends. The LAAPDs were custom-chosen instead of using PMTs for EXO-200 to improve the quantum efficiency and minimize radioactive contamination [52].

The TPC is housed in a vessel with 1.37-mm thick walls of ultra-pure copper enclosing the 110-kg active volume of LXe (Figure 2.2). The Cu vessel was designed to minimize activity nearest the LXe, yet still reliably withstand a 35 kPa pressure differential. The xenon is

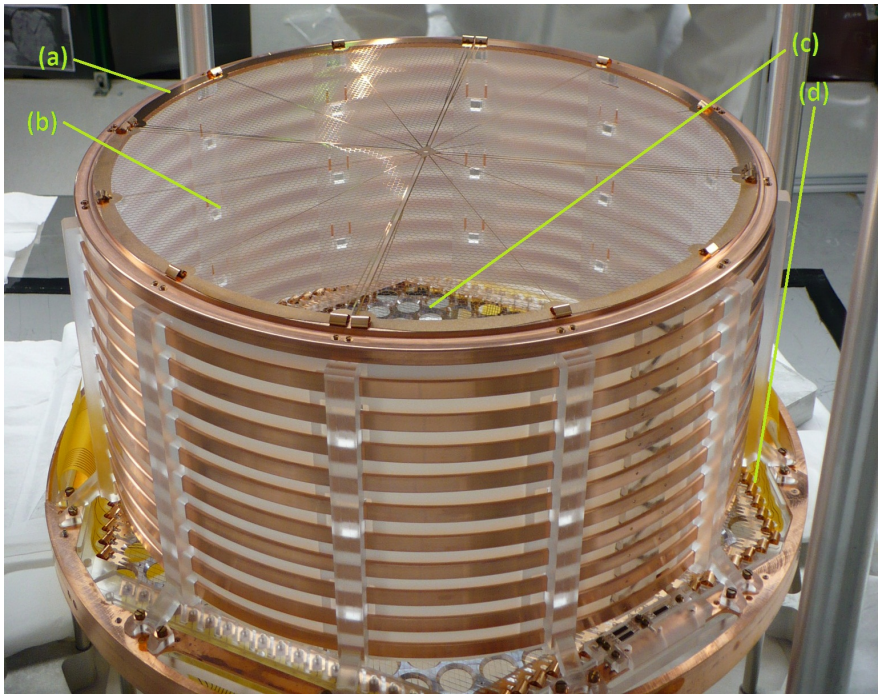

Figure 2.1: One half of the EXO-200 TPC before completion. The cathode grid (a) is common to both TPC halves. PTFE tiles (b) line the walls of the cylinder to reflect the scintillation light. The aluminum-plated LAAPD plane (c) can be seen, without the LAAPDs installed. The two sets of wire grids (d) can be seen, one rotated at 60° from the other (Photo by Nicole Ackerman).

maintained at 167 K using a heat exchanger fluid, HFE-7000 [53], in thermal contact with the Cu vessel inside a cryostat. The cryostat has a 1" thick inner wall made of copper, which contains the HFE, and an outer wall with vacuum insulation in between. A 25-cm thick lead wall surrounds the cryostat for additional shielding. All of this is located inside a class 1000 clean room. Surrounding the clean room is a muon veto counter made of plastic scintillators. A cutaway view of the clean room module containing these components can be seen in Figure 2.3. A detailed description of the detector's design can be found in [54].

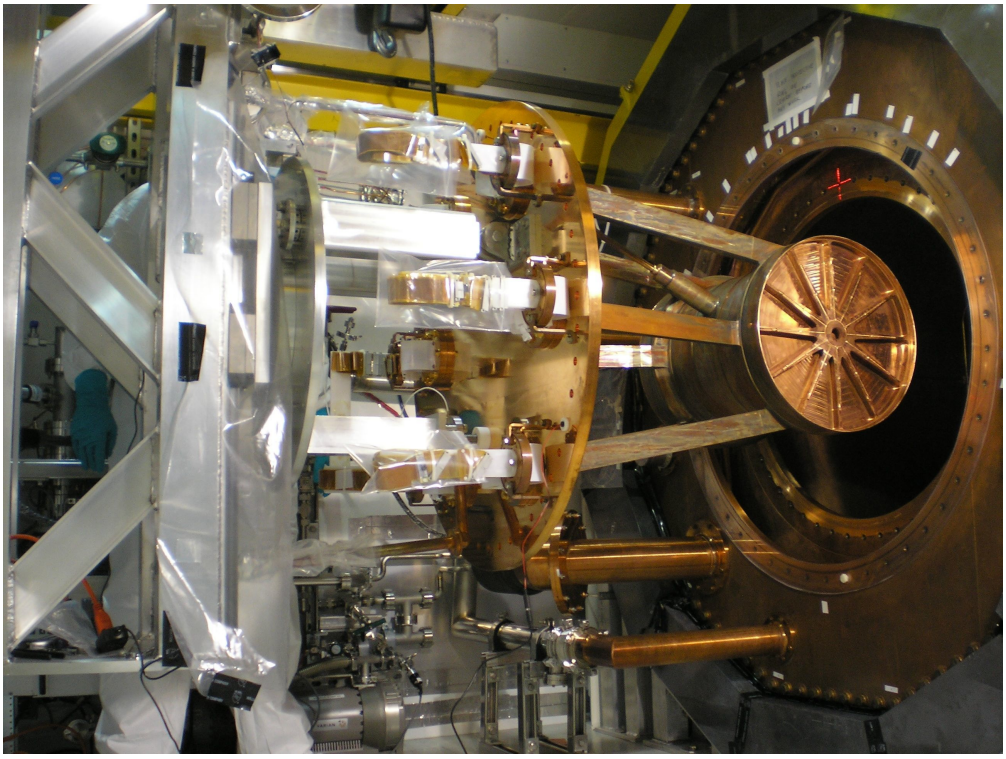

Figure 2.2: TPC being inserted into the cryostat.

2.2.1 Background Reduction

EXO-200 was designed to be sensitive to $T_{1/2}^{0\nu\beta\beta} = 6.4 \times 10^{25}$ yr (90% C.L.) after two years of live time. For this to be accomplished, a limit of 40 background events in a $\pm 2\sigma$ window around the $2\nu\beta\beta$ end-point was imposed. This is assuming a fiducial mass of 140 kg in the active Xe, although the final design was 110 kg [54].

Several steps are taken to minimize background contributions: screening the materials going into the detector, cleaning of surface contaminants before installing materials, shielding the detector (e.g. from ^{222}Rn in the air), and limiting cosmic ray activation. An extensive study was carried out to quantify backgrounds from all the components of the EXO-200 detector [55].

One of the most critical volumes to control for background is the LXe itself. The re-

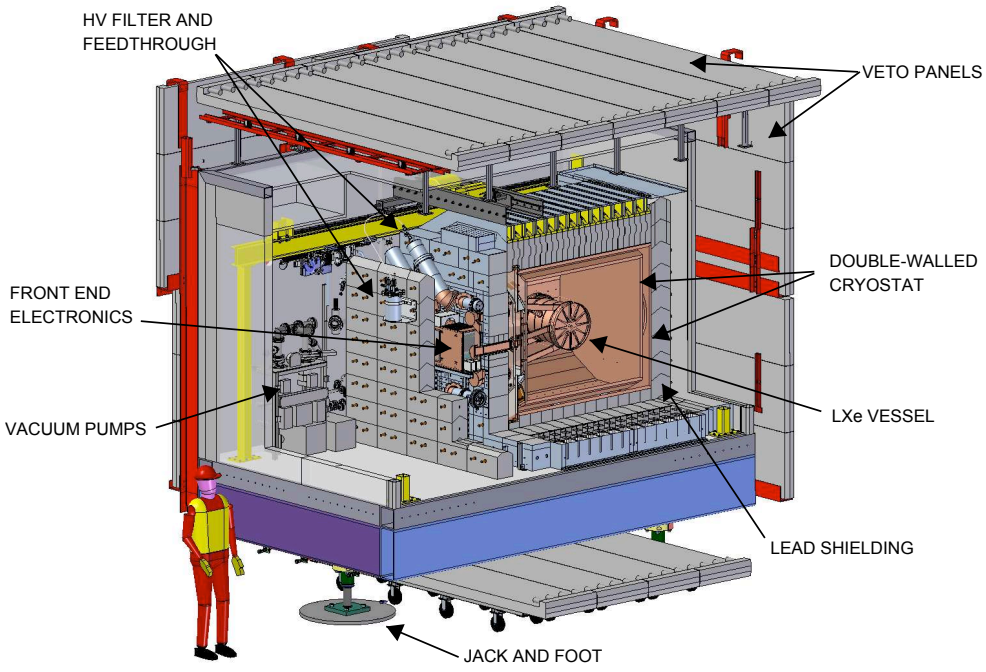

Figure 2.3: Cutaway view of the clean room module containing the EXO-200 detector [54].

strictions discussed above allow internal TPC components to contribute only a maximum of 1% of the total allowable $0\nu\beta\beta$ background rate. ^{214}Bi is particularly nefarious when it β^--decays because the excited ^{214}Po daughter emits 1.5 % of its photons at a peak of 2.448 MeV [56]. This corresponds to 0.996 K_e/Q in Figure 1.4 and lies within a 1σ window of the Q-value with EXO-200's current energy resolution.

The production of ^{214}Bi is supported by ^{222}Rn which is known to be produced in certain parts of the EXO-200 detector (piping, Mott filter, gas purity monitors, Kapton cables, etc.). Despite the extreme care taken to prevent radioactive isotopes to enter the EXO-200, trace amounts of ^{238}U are inevitable. ^{238}U leads to ^{222}Rn, which supports ^{214}Bi. ^{222}Rn was found to have a steady-state activity of 428 ± 12 μBq in 107.7 kg of LXe, corresponding to 200 Rn atoms. Without analysis and fiducial cuts, this translates to an expected background rate of 0.26 events per year in the $\pm 2\sigma$ windows around the Q-value [57].

Chapter 3

Radon Removal in Xenon

Radon and xenon are both chemically inert noble gases, and so there are few small physical differences between them that can be exploited in order to separate Rn from Xe. XMASS has shown radon removal to be possible by physical adsorption on activated charcoal [58]. This might be worth considering, however activated charcoal has its drawbacks: it produces particulates which could be dangerous for the high voltage in EXO-200 and affect the electron drift. Presented here is the idea of Rn removal by physical adsorption on large surfaces of transition metals, particularly Cu wool.

3.1 Physical Adsorption

Physical adsorption is the result of weak van der Waals forces between atoms. It is possible for a solid material to attract passing atoms with sufficiently low kinetic energy to be bound temporarily to the surface of the solid, trapping material. The trapped atom releases an adsorption enthalpy, which relates to the mean residence time, or "sojourn time", of each atom [59]:

$$\tau = \frac{1}{\nu_b} \exp\left(\frac{-\Delta H_{\text{ads}}}{RT}\right) \tag{3.1}$$

where ν_b is the maximum phonon frequency of the metal lattice in Hz; ΔH_{ads} is the adsorption enthalpy in J/mol; R is the ideal gas constant, $R = 8.31446$ J/mol·K; and T is the temperature in K.

For trapping Rn on a Cu surface, the maximum phonon frequency is $\nu_b = 6.7 \times 10^{12}$ Hz. The adsorption enthalpy depends on any pre-conditioning to the Cu surface. Without surface treatment, the negative adsorption enthalpy is $-\Delta H_{\text{ads}} = 30$ kJ/mol. With the treatment of the Cu surface with a mixture of $H_2 + N_2$ gas, the adsorption enthalpy becomes $-\Delta H_{\text{ads}} = 41$ kJ/mol. This treatment involves heating the trap to 1000 K for 2 hours, flowing a mixture of $N_2 + H_2$ (90 : 10 vol%) for 100 mL/min. The hot gas removes oxides from the Cu surface, thereby reducing it.

Figure 3.1 illustrates the effect of surface treatment on sojourn time. It also shows the capacity of Cu to retain Rn much longer as the kinetic energy of the Rn atoms decrease. If 1000 mbar of Xe carrier gas is cooled to just above condensation point at 166 K, we have a sojourn time of $\tau = 7.44 \times 10^{-4}$ s for untreated Cu and $\tau = 2.15$ s for reduced Cu. This demonstrates how a slight increase in adsorption enthalpy leads to over three orders of magnitude increase in sojourn time due to the exponential term.

3.2 Trap Design Criteria

The principle of Rn removal for the EXO-200 detector begins by exploiting Rn adsorption on the microscopic scale. With each adsorption event, a Rn atom is bound temporarily before it is released back to the flowing gas. The goal is for the Rn atom to meet another Cu surface

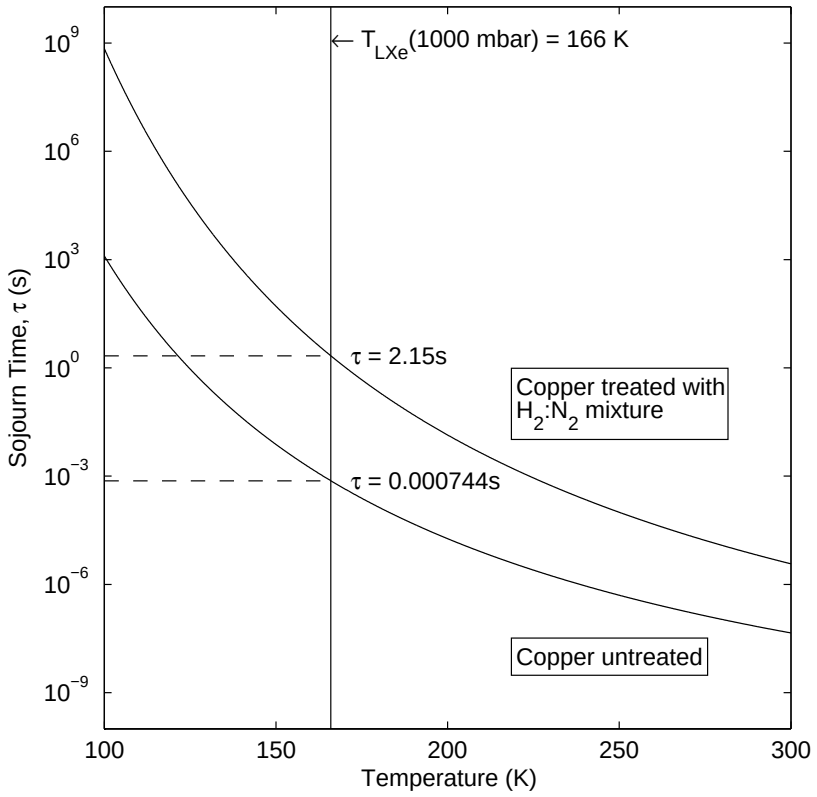

Figure 3.1: Sojourn time of radon on copper.

before being released, and captured, and so on until the atom decays, before it has the chance to leave the trap and enter the TPC.

Early Monte Carlo simulations of the EXO-200 detector assumed a 140 kg fiducial volume of LXe, with an energy resolution of 1% at the Q-value. Assuming $\langle m_\nu \rangle = 0.39$ eV from the discovery claim [38], and using the most-limiting NME calculation from [60], we would expect 34 $0\nu\beta\beta$ events per year at a half-life of $T_{1/2}^{0\nu\beta\beta} = 1.5\times10^{25}$ years. For EXO-200 to be sensitive to these events, the total background contribution from any source within a $\pm2\sigma$ window was set to be less than 10% of the expected event rate. Monte Carlo simulations determined that the maximum allowable steady state of Rn in the LXe is 11 atoms. However, an extensive measurement of detector components prior to assembly determined a constant production of

200 atoms/day of ^{222}Rn [55]. A margin of safety to allocate for components installed after the study and backgrounds introduced during assembly (e.g. welds) would make it safer to assume up to 1000 atoms/day. To maintain a steady state population of 11 Rn atoms at all times in the TPC, there can be a maximum of ∼2 Rn atoms produced in the TPC per day. Another twenty-fold safety margin is added because the internal components of the TPC are likely to contribute Rn as well. Therefore, we allow an ingress of 0.1 atom/day. To achieve a reduction of 1000 to 0.1 atom/day means a target efficiency of 99.99% for the trap.

Knowing the desired efficiency of the trap, we know how much time the average Rn atom needs to be confined in the trap. This "total residency" t is different from the aforementioned sojourn time. Total residency is the cumulative time for each adsorption event followed by the transport time after each adsorption. From radioactive decay, we know the desired total residency to be:

$$\begin{aligned} N_t &= N_0 e^{-\lambda t} \\ t &= \frac{-\ln \frac{N_t}{N_0}}{\lambda_{\mathrm{Rn}}} \\ t &= 50.8 \text{ days} \end{aligned} \tag{3.2}$$

where λ_{Rn} is the decay constant for ^{222}Rn and N_0 and N_t are the Rn populations before and after flowing through the trap, respectively. To operate on the EXO-200 detector, the Rn trap must also work for a flow rate of 20 LPM with a maximum ΔP of 1 psi. We also know from Section 3.1 to operate the trap at 166 K.

Building a trap to test for Rn removal requires choosing between different transition metals, different metal geometries, and different packing densities. Two traps were constructed by Murray Wilson and Jared Johnson during their 4$^{\text{th}}$ year Honours thesis. The first is

Trap Material	Substance Mass (g)	Packed Length (cm)	Linear Packing Density (g/cm)	Packed Volume (cm^3)	Tubing Volume (cm^3)	Porosity (%)	Total Area (cm^2)
Cu Wool	40.0	40.64	0.98	4.47	31.5	85.8	7050
Cu Sphere	258.0	40.64	6.35	29.44	31.5	6.6	3395
Ni Wool #1	16.3	12.04	1.35	1.82	9.3	80.5	1030
Ni Wool #2	22.9	23.34	0.98	2.57	18.1	85.8	1450

Table 3.1: Comparing a Cu trap built for testing by Murray Wilson and Jared Johnson with two new Ni traps

the Cu wool trap, which was chosen for testing in this thesis for a few reasons. Cu has a relatively high affinity for Rn [59] and low cost. Cu wool was preferred over spheres for its high porosity, which reduces impedance, and its high surface area. Different packing densities were measured for impedance before packing the trap to 0.98 g/cm [61]. The second trap is the Cu spheres trap, which contains 258 g of spheres. The Cu spheres trap had an additional 1 g of Cu wool packed over 2.54 cm at each end of the trap to prevent the spheres from escaping during operation. The specifications of both traps are shown in Table 3.1.

The packing density is chosen on the grounds of maximizing the amount of contact area available in the trap, while minimizing the impedance and resulting ΔP. 0.98 g/cm was chosen for the Cu Wool trap as a compromise between the two. Two new Ni wool traps were built, with the goal to build one trap with a similar packing density which would allow a direct comparison between the two metals, and another Ni wool trap with improved contact area. The disadvantage with the current Ni wool material is a thicker wire diameter in comparison to Cu (7.11×10^{-3} vs. 2.54×10^{-3} cm, respectively), which limits the amount of surface that can be packed without affecting impedance severely. The Cu wool trap is tested in this thesis and the specifications of the other traps are provided in Table 3.1 for future

use.

3.3 Methodology

A system is needed to test Rn removal. It requires the following main components (Figure 3.2, starting clockwise from top-right): a supply of Xe gas; a way of recovering/resupplying Xe gas; a detector for Rn atoms (more specifically, charged daughters of Rn decay); a Rn source to spike the Xe gas; a purifier for the gas; and the trap itself. An elaborate plumbing system was built to test Rn removal from Xe, with these main components branching off a recirculation loop. This is from here on out called the "XeRn System".

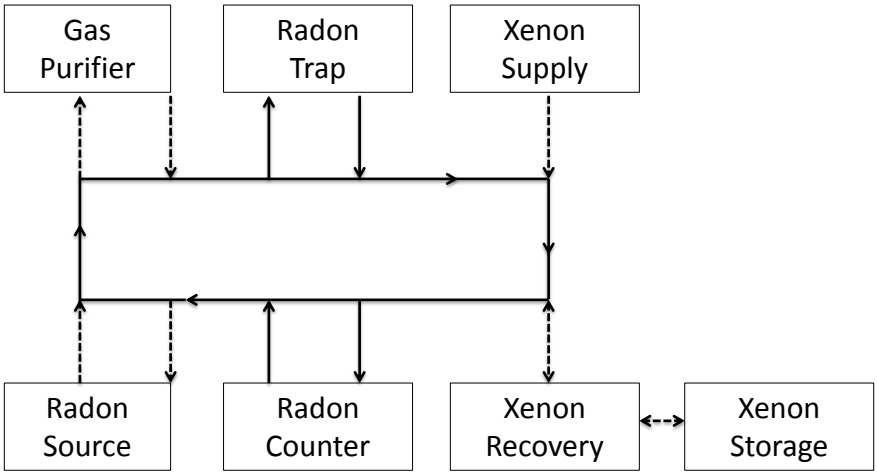

Figure 3.2: Hardware required to test Rn removal. The solid lines mark the components mainly in use during a data run; the dashed lines are components used in preparation for a data run.

When testing any trap, a "RnRun" is planned and carried out. A RnRun is the term used when controlling the XeRn system, recording data from sensors on the system (on the LabView PC), as well as collecting count rates on the DAQ PC. Individual RnRuns are enumerated by Roman numerals. The general outline of a RnRun goes as follows:

1. Inject the Xe with Rn by flowing through a ^{222}Rn source.
2. Purify the gas to remove impurities which would affect Rn trapping and ^{218}Po detection efficiencies.
3. Start the DAQ data run and LabView data run.
4. Count over an interval of time to establish an initial baseline for the Rn concentration.
5. Cool the trap to close to condensation point, flowing through the trap, to attempt Rn removal.
6. Warm up and count again to reestablish baseline conditions and see if any Rn was removed.

This was the general plan of each run. However with the results of each run, the methodology was adapted to decouple independent variables such as flow and impurity of the gas.

Chapter 4

The XeRn System

4.1 Introduction & Purpose

The purpose of this chapter is to list the hardware used during RnRuns, and explain the principles of operation. The complete flowsheet of the XeRn System, with all its subcomponents, is shown in Appendix A. Figure 4.1 shows the XeRn System with the main flow path highlighted and the pressure and flow sensors most relevant for analysis.

4.2 Xenon Supply Bottle

A bottle of Xenon 5.0 (99.999% pure) feeds through XRV-43 and XRV-45, with regulator valve XRV-44 in between. A needle valve feeds the Xe into the main recirculation loop (main rectangle in Figure 3.2). For most of the RnRuns, no gas is actually taken from this supply since new Xe for each data run would be too expensive.

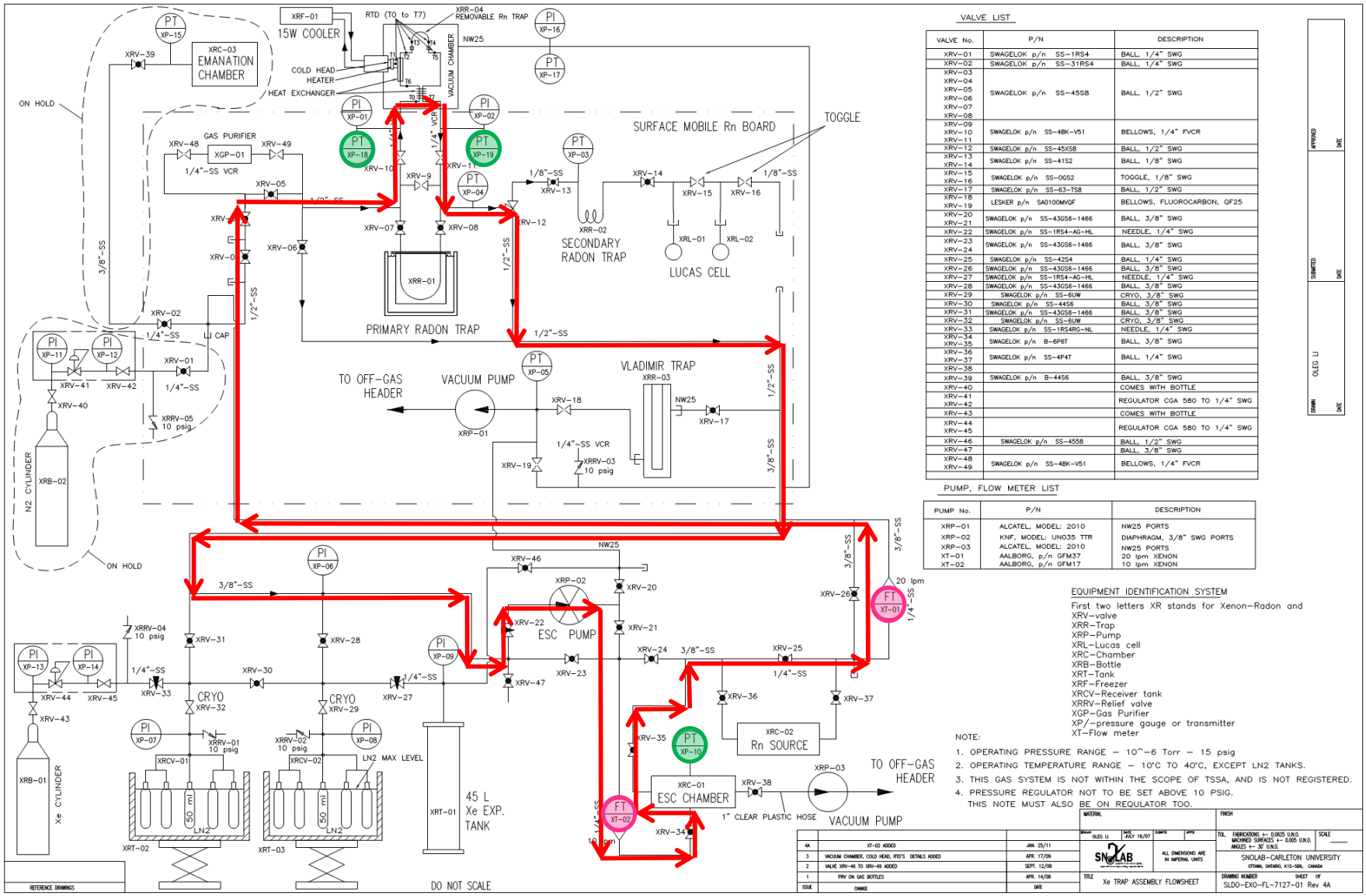

VALVE LIST

VALVE No.	P/N	DESCRIPTION
XRV-01	SWAGELOK p/n SS-1RS4	BALL, 1/4" SWG
XRV-02	SWAGELOK p/n SS-31RS4	BALL, 1/4" SWG
XRV-03 XRV-04 XRV-05 XRV-06 XRV-07 XRV-08	SWAGELOK p/n SS-45S8	BALL, 1/2" SWG
XRV-09 XRV-10 XRV-11	SWAGELOK p/n SS-4BK-V51	BELLOWS, 1/4" FVCR
XRV-12	SWAGELOK p/n SS-45XS8	BALL, 1/2" SWG
XRV-13	SWAGELOK p/n SS-41S2	BALL, 1/8" SWG
XRV-14		
XRV-15 XRV-16	SWAGELOK p/n SS-0GS2	TOGGLE, 1/8" SWG
XRV-17	SWAGELOK p/n SS-63-TS8	BALL, 1/2" SWG
XRV-18 XRV-19	LESKER p/n SA0100MVQF	BELLOWS, FLUOROCARBON, QF25
XRV-20 XRV-21	SWAGELOK p/n SS-43GS6-1466	BALL, 3/8" SWG
XRV-22	SWAGELOK p/n SS-1RS4-AG-HL	NEEDLE, 1/4" SWG
XRV-23 XRV-24	SWAGELOK p/n SS-43GS6-1466	BALL, 3/8" SWG
XRV-25	SWAGELOK p/n SS-42S4	BALL, 1/4" SWG
XRV-26	SWAGELOK p/n SS-43GS6-1466	BALL, 3/8" SWG
XRV-27	SWAGELOK p/n SS-1RS4-AG-HL	NEEDLE, 1/4" SWG
XRV-28	SWAGELOK p/n SS-43GS6-1466	BALL, 3/8" SWG
XRV-29	SWAGELOK p/n SS-6UW	CRYO, 3/8" SWG
XRV-30	SWAGELOK p/n SS-44S6	BALL, 3/8" SWG
XRV-31	SWAGELOK p/n SS-43GS6-1466	BALL, 3/8" SWG
XRV-32	SWAGELOK p/n SS-6UW	CRYO, 3/8" SWG
XRV-33	SWAGELOK p/n SS-1RS4RG-NL	NEEDLE, 1/4" SWG
XRV-34 XRV-35	SWAGELOK p/n B-6P6T	BALL, 3/8" SWG
XRV-36 XRV-37	SWAGELOK p/n SS-4P4T	BALL, 1/4" SWG
XRV-38		
XRV-39	SWAGELOK p/n B-44S6	BALL, 3/8" SWG
XRV-40		COMES WITH BOTTLE
XRV-41 XRV-42		REGULATOR CGA 580 TO 1/4" SWG
XRV-43		COMES WITH BOTTLE
XRV-44 XRV-45		REGULATOR CGA 580 TO 1/4" SWG
XRV-46	SWAGELOK p/n SS-4558	BALL, 1/2" SWG
XRV-47		BALL, 3/8" SWG
XRV-48 XRV-49	SWAGELOK p/n SS-4BK-V51	BELLOWS, 1/4" FVCR

PUMP, FLOW METER LIST

PUMP No.	P/N	DESCRIPTION
XRP-01	ALCATEL, MODEL: 2010	NW25 PORTS
XRP-02	KNF, MODEL: UNO35 TTR	DIAPHRAGM, 3/8" SWG PORTS
XRP-03	ALCATEL, MODEL: 2010	NW25 PORTS
XT-01	AALBORG, p/n GFM37	20 lpm XENON
XT-02	AALBORG, p/n GFM17	10 lpm XENON

EQUIPMENT IDENTIFICATION SYSTEM

First two letters XR stands for Xenon-Radon and
XRV-valve
XRR-Trap
XRP-Pump
XRL-Lucas cell
XRC-Chamber
XRB-Bottle
XRT-Tank
XRF-Freezer
XRCV-Receiver tank
XRRV-Relief valve
XGP-Gas Purifier
XP/-pressure gauge or transmitter
XT-Flow meter

NOTE:
1. OPERATING PRESSURE RANGE - 10^-6 Torr - 15 psig
2. OPERATING TEMPERATURE RANGE - 10°C TO 40°C, EXCEPT LN2 TANKS.
3. THIS GAS SYSTEM IS NOT WITHIN THE SCOPE OF TSSA, AND IS NOT REGISTERED.
4. PRESSURE REGULATOR NOT TO BE SET ABOVE 10 PSIG. THIS NOTE MUST ALSO BE ON REQULATOR TOO.

ISSUE	CHANGE	DATE
4A	XT-02 ADDED	JAN. 25/11
3	VACUUM CHAMBER, COLD HEAD, RTD'S DETAILS ADDED	APR. 17/09
2	VALVE XRV-46 TO XRV-49 ADDED	SEPT. 12/08
1	PRV ON GAS BOTTLES	APR. 14/08

SNOLAB
SNOLAB-CARLETON UNIVERSITY
OTTAWA, ONTARIO, K1S-5B6, CANADA
TITLE: Xe TRAP ASSEMBLY FLOWSHEET
DRAWING NUMBER: SLDO-EXO-FL-7127-01 Rev 4A

Figure 4.1: Main flow path used during RnRuns. Pressure and flow sensors most relevant to analysis are highlighted.

4.3 Xenon Recovery Vessels and Storage

Most of the Xe actually in use is recovered, stored, and reused. There are two recovery vessels, XRCV-01 and XRCV-02, each with 5×50 mL recovery bottles. Two cold baths, XRT-02 and XRT-03, respectively, are LN_2 tanks that are raised to the recovery vessels.

During cryopumping of the system's gas, the LN_2 is typically only raised to touch the bottom of the recovery bottles so as not to plug the top of the bottles with Xe. The pressure inside these bottles is read on analog Swagelok gauges XP-07 and XP-08. If these bottles are filled, isolated and allowed to warm up, the gas expansion poses a risk. Thus each bath is fitted with pressure relief valves XRRV-01 and XRRV-02, rated to 10 psig. This makes monitoring XP-07 and XP-08 crucial during cryopumping, since we do not want to blow costly Xe into the clean room. A 45 L expansion tank is connected to XRT-01 and, optionally XRT-02 (via XRV-30), for longer term storage.

4.4 Recirculation Pump

The direction of flow in the XeRn system is determined by the recirculation pump, XRP-02, which is a Teflon-coated diaphragm pump. It has a bypass valve, XRV-23, which is typically left closed, and outlet valve, XRV-21, which is left open. A needle valve at the inlet, XRV-22, is used to adjust the inlet pressure and keep it within the pump's specifications.

4.5 Electrostatic Counter

Immediately downstream of the recirculation pump is the Electrostatic Counter (ESC), which collects and records the decay of positively-charged Po ions, the progeny of Rn decay. Only ^{222}Rn from the uranium chain is of interest to us here, although the ESC is also sensitive

to Po isotopes from ^{220}Rn in the thorium chain. The ESC is essentially a hemispherical drift chamber designed to maximize the counting efficiency of $^{216}Po^{+}$ ions from the Th chain [62]. A voltage supply provides a negative bias of 1000 V that establishes an electrostatic field in the 10 L chamber, effectively drifting Po^{+} ions towards a silicon PIN photodiode at the top of the detector. The collected Po^{+} ions α-decay and deposit a distinct energy for each isotope. The charge signal goes through a pre-amplifier, followed by a multi-channel analyzer (MCA) which bins the signal by pulse height into a spectrum stored in a multi-channel buffer (MCB). The MCA and MCB are integrated in a two-wide NIM module made by EG&G ORTEC (part number 920-16). The spectrum is transferred at predetermined intervals to the controlling PC, the DAQ PC, for analysis. A complete description of the ESC is provided in [62]. The counting efficiencies of the ESC is discussed in Chapter 5.

To help us understand the effects of flow and pressure on counting efficiencies of the ESC, we have an Aalborg® 10 SLPM mass flowmeter (MFM, part number GFM-17), which we label XT-02, installed in the inlet, and a Pirani Capacitance diaphragm gauge by Inficon (part number PCG400), labelled as XP-10, on the ESC chamber.

4.6 Radon Source

Downstream of the ESC is the Rn source, a 62 Bq source of ^{222}Rn, which emanates from a 567 Bq sample of ^{238}U (Autinite crystal). It was approved for use in the Low-Background Room at SNOLAB as source #SRS-10-001. Just after the source is another mass flowmeter, XT-01, which monitors the "system" flow (flow along the main recirculation loop). This MFM can read up to 20 SLPM (part number GFMS-013435).

4.7 Gas Purifier

Next in the recirculation loop is the NuPure Eliminator-600CG Purifier, XGP-01 on the XeRn flowsheet. This is a getter that operates at room temperature and was in fact shown to be a non-negligible source of Rn [63]. Therefore, the gas is not purified *in situ* for RnRuns, but only for a sufficient number of flushes before isolating the purifier and measuring the first baseline of ^{218}Po.

4.8 Heat Exchanger

When cooling during a RnRun, the heat exchanger (isolated in a vacuum) is actively cooled by a PolyCold CryoTiger refrigeration unit, with a High Performance PT-30 cold head. The cold head is in thermal contact with a cylindrical Cu spool, which in turn is screwed onto 13.625-inch long Cu plates. The Cu plates have grooves in which the stainless steel tubing weaves in and out to optimize contact surface area and transfer heat away from the plumbing. The stainless steel tubing leaving the trap also travels through the plates so as to return heat to the gas as it leaves the enclosure. Full engineering diagrams are found in [64].

4.9 Cryogenics and Temperature Control

Cooling to $-110\,^{\circ}$C is achieved by first having the refrigerator on. The refrigerator's cooling power peaks near this temperature at ~ 30 W (see commercial flyer in [65]), which is more than enough power to reach the setpoint. The excess power is compensated by controlling a heater on the Cu spool. The heater is controlled by reading a process variable, T1, into LabView (which is discussed in Section 4.12). T1 is input into a PID loop in

LabView along with the desired setpoint to determine a binary value whether the heater should be ON (1) or OFF (0). This binary value is output as 3 or 0 V respectively, which is sent to a relay box on the XeRn cart. If the relay box is sent 3 V, it switches on, powering a variable AC power outlet (VariAC), which powers the heater, a Kapton Flexible Heater (part number KHLV-105/10). The Kapton heater wraps around the cylindrical Cu spool for thermal contact. This heater strip plays a balancing act with the refrigerator in order to find and maintain the setpoint. The VariAC has a notched setting of 18 V on the dial from previous experiments, however in RnRuns we have had to go up to a measured 29 V AC. Near 29 V AC, the heater behaviour needs to be closely monitored (e.g. rate of change in the PID, and T11). Beyond 29 V AC, the heater strip runs a risk of getting destroyed (although this varies with Xe pressure, flow rate through heat exchanger, and quality of insulating vacuum).

4.10 Radon Trap

The Rn trap that is used for the RnRuns in this thesis is a section of stainless steel tubing packed to 0.98 g/cm (Table 3.1). The trap is bent in a U-shape and tapered on one end so as to meet two fittings facing downwards in the vacuum enclosure (see Figures 4.2a and 4.2b).

Two Ni wool traps have also been prepared, each with a different packing density. The first Ni trap has 16.25 g packed over 12.04 cm, equating to a linear packing density of 1.35 g/cm. The second Ni trap has 22.9 g packed over 23.34 cm of tubing, or a linear packing density of 0.98 g/cm (see Figure 4.2c).

(a) Packed Cu wool piece, inserting into trap (photo by Jared Johnson).

(b) Cu Wool trap. Full tubing length is 18" (photo by Jared Johnson).

(c) Packed Ni wool piece, before inserting into trap.

Figure 4.2: Radon trap builds

4.11 Vacuum Enclosure and Temperature Sensors

A vacuum enclosure fitted with reflective superinsulation provides thermal insulation of cryogenic components (heat exchanger, temperature control and Rn trap). The enclosure is pumped down by an Edwards system involving a turbomolecular pump, backed by a BOC Edwards XDS10 scroll pump.

Just outside of the vacuum enclosure, we have three pressure sensors that are recorded digitally, XP-18 for pressure upstream of the trap, XP-19 downstream, and XP-04 as an indicator of the local system pressure. XP-18 and -19 help us estimate the condensation point of Xe near the cold head by interpolating between the gauges. These are all Cole-Parmer Vacuum Pirani-Type sensors (model #68801-53).

There are several temperature sensors found inside the vacuum enclosure. The sensors are Resistance Temperature Detectors (RTDs) by Omega® (part number RTD-2-1PT100KN1515-36-T). The RTDs are placed at strategic points around the heat exchanger, heater block and Rn trap. The RTDs are bonded onto the plumbing using StyCast® Epoxy 2850 FT, Catalyst 9. A diagram of the RTD locations is found in Figure 4.3. Their locations on the vacuum enclosure feedthroughs are provided as reference in Appendix D. The RTDs most used in this thesis are T1 (as the temperature control process variable), T11 (to monitor the Kapton heater), T2, T5, and T8 (upper inlet, bottom, and upper outlet of the trap, respectively).

4.12 Instrumentation

The various sensors installed on the XeRn system were already mentioned earlier in order of proximity to other components on the XeRn system. Each sensor is wired into a programmable automation controller (the “Compact FieldPoint” by National Instruments)

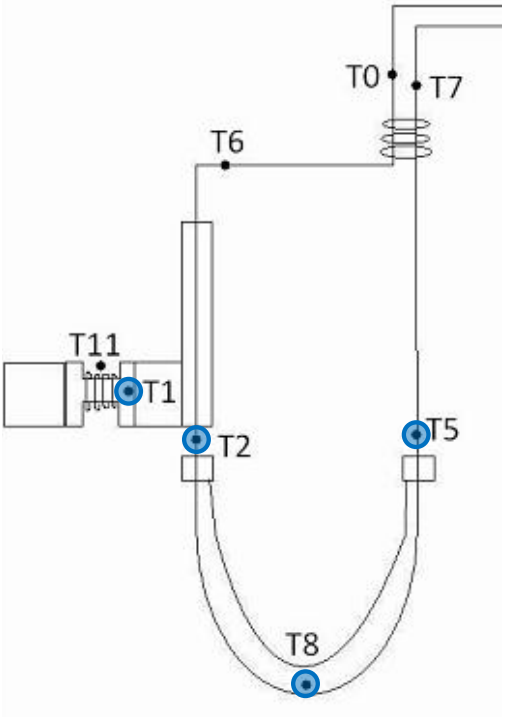

Figure 4.3: RTD locations inside the vacuum enclosure. The RTDs most relevant for analysis are highlighted.

which interfaces the sensors with LabView, which is running on a PC with Windows XP operating system. An 8-channel analog output module by NI, cFP-AO-210, is used to transmit either 0 or 3 V to the relay box, which powers the heater (via the VariAC).

Temperature data from the RTDs are sent to LabView through an 8-channel input module specifically for three-wire RTDs, called cFP-RTD-122.

Another 8-channel input module, cFP-AI-100, exists for the pressure and flow sensors. This module is flexible in that it can either provide power to the sensor or accept sensors with external power supplies.

Each of these modules is wired through their own connector block, cFP-CB-1.

Pressures, temperatures and flows are read out onto the LabView PC and written to file in 5 s intervals. Temperature control parameters, such as T1, setpoint, and the PID output

are written to their own file in 1 s intervals. A 1 s feedback loop is critical for the responsive control of the heater element. The current version in use for the LabView control panel is `TPF_Readings_V13.vi`. This version has seen a few improvements to help streamline data collection: directories and files are automatically created and named along with a timestamp. A parameter in the block diagram can be altered to create new data files at different rates. It is currently set to create new heater and Pressure/Temperature/Flow (PTF) files every hour, which makes transferring data easier if a user wishes to analyze data before the RnRun is over.[1]

The LabView control panel can also be monitored and controlled remotely if configured properly on the user's PC. Instructions on using the control panel are provided on [66].

4.13 Data Analysis (ESC)

The ESC data are read onto a different DAQ entirely. The aforementioned energy spectrum that is read through the MCA is relayed to a Multi Tasker program, run by MAESTRO®-32 on a DOS PC. The script running on the DOS PC (or "DAQ PC") can be altered to save the total accumulated spectrum in different time intervals. In this thesis the ESC runs are mostly saved in 20 min intervals, although 5 min intervals were also used.

The data is zipped and transferred by floppy disk onto the "DAN PC" (a third PC running Windows XP 2000), where the `READESC` program is called to process the data. `READESC` takes a directory containing all the spectra files, fits a probability distribution function (PDF) to data inside four energy windows (one for each Po isotope), for each spectrum file, while accounting for some overlap such as a slight ^{212}Bi tail from ^{212}Po which

[1] Copying and pasting LabView data files while they are still being written will result in LabView crashing, which is especially undesirable when the heater is under PID control!

overlaps on the ^{218}Po peak. The incremental number of counts are then integrated in each energy window, for each spectrum. `READESC` outputs this into a `.SUM` file which contains the index of each spectrum file, start and stop times, ESC live times, and number of new counts for each isotope, as well as the incremental sum of counts over time.

Chapter 5

Drift of Polonium Ions in the Electrostatic Counter

The ESCs were designed primarily to maximize the detection efficiency of ^{216}Po from the decay of ^{220}Rn in the Thorium chain. The other Po^+ ions were also of secondary interest. The shape of the chamber was chosen based on what was feasible for fabrication and to minimize the dead volume where ions could evade detection. It was also designed to be tested by circulating dry N_2 [62]. It is unclear what effect a mixture of gases would have on the counting efficiency of the ESC, such as impurities of polar atoms like H_2O and NO_2. Previous work has been done to model the progression of Po^+ ions in the ESC [67], but not for Po^+ in Xe gas.

5.1 Field Model of the ESC

To get an idea of the ESC's counting efficiency as a function of carrier gases, an understanding of the electrostatic field in the ESC is needed. The field can be obtained from

Gauss's law in a vacuum,

$$\nabla \cdot \mathbf{E} = 0 \tag{5.1}$$

Knowing the field to be the gradient of electrostatic potential, we have the Laplace equation,

$$\mathbf{E} = -\nabla V \tag{5.2}$$

$$\nabla^2 V = 0 \tag{5.3}$$

It is easier to first numerically solve the Laplace equation to find the potential, and from there compute the electric field. A model of the electric field in the ESC is constructed using MATLAB. The field in the ESC is established by applying High Voltage across the PIN photodiode, which is kept at a constant negative potential (typically 1000 V). The walls of the ESC are kept at ground potential. The dimensions used in the model are shown in Figure 5.1. Knowing the ground and applied voltage as our boundary values, the Laplace equation can be solved. The method chosen here is the relaxation method, which is explained in detail in Chapter 19 of [68].

The general idea of the relaxation method is to construct a grid of points within the space of interest. An update algorithm is used to iterate through the grid points, and take weighted averages of the surrounding grid points. The update algorithm depends on the partial differential equations to be solved, which in this case is the Laplace equation in cylindrical coordinates (5.4). Taking advantage of the counter's rotational symmetry about the axis through the centre of the PIN diode, the Laplace equation is reduced to a two-

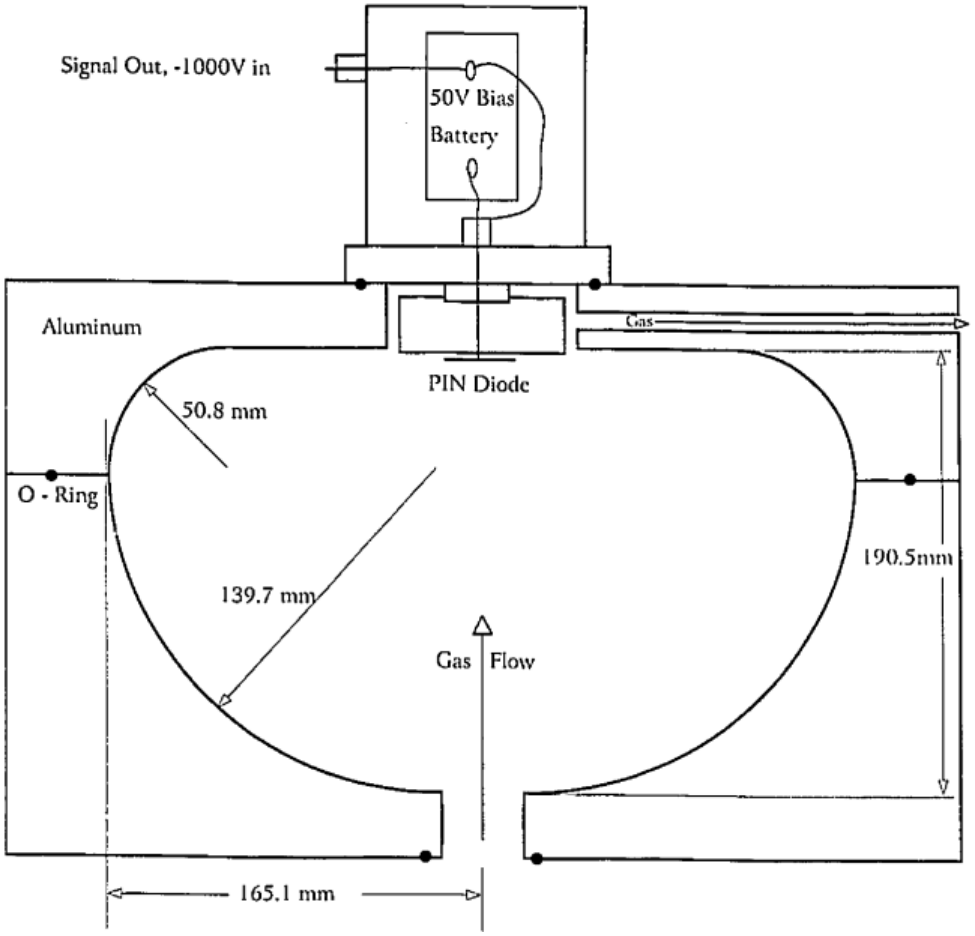

Figure 5.1: Design and dimensions of the ESC Chamber, taken from [67]. Note that the hole holding the diode is 2.5″ in diameter, and the PIN diode is a square with 18 mm edges. The field model approximates the diode to a disc with the same surface area.

dimensional problem,

$$\frac{1}{\rho}\frac{\partial}{\partial\rho}\left(\rho\frac{\partial V}{\partial\rho}\right)+\frac{1}{\rho^2}\frac{\partial^2 V}{\partial\phi^2}+\frac{\partial^2 V}{\partial z^2}=0 \tag{5.4}$$

$$\frac{1}{\rho}\frac{\partial}{\partial\rho}\left(\rho\frac{\partial V}{\partial\rho}\right)+\frac{\partial^2 V}{\partial z^2}=0 \tag{5.5}$$

The partial derivatives are approximated through the use of finite differences.

$$\frac{V(\rho+\Delta\rho,z)-V(\rho,z)}{\rho\Delta\rho}+\frac{V(\rho+\Delta\rho,z)-2V(\rho,z)+V(\rho-\Delta\rho,z)}{\Delta\rho^2} + \frac{V(\rho,z+\Delta z)-2V(\rho,z)+V(\rho,z-\Delta z)}{\Delta z^2}=0 \tag{5.6}$$

where $\Delta\rho$ and Δz are grid spacings (we set $\Delta\rho = \Delta z = 0.5$ mm here). For ρ spanning from 0 to 175.0 mm and z from 0 to 229.0 mm, this makes our grid of size 351×459 points. The MATLAB script uses an index notation for programming purposes. It also helps to use this index notation as a short-hand. The spatial coordinates are replaced by indices i and j such that:

$$\rho_i = i\Delta\rho \tag{5.7}$$

$$z_j = j\Delta z \tag{5.8}$$

Given this convention the grid of potentials can be written as

$$V_{i,j} = V(\rho, z) \tag{5.9}$$

Due to our usage of cylindrical coordinates, we have ρ in the denominator in the first part of (5.6). For the case of $\rho = 0$, we take the limit as i approaches 0 to avoid a discontinuity. We now see that the potential simply takes on the value of its nearest neighbour in ρ (for the case of $\rho_i = 0$).

$$\lim_{i\to 0}\left\{\frac{1}{i\Delta\rho^2}\left(V_{i+1,j}-V_{i,j}\right)+\frac{1}{\Delta\rho^2}\left(V_{i+1,j}-2V_{i,j}+V_{i-1,j}\right)+\frac{1}{\Delta z^2}\left(V_{i,j+1}-2V_{i,j}+V_{i,j-1}\right)\right\}=0$$
$$\lim_{\imath\to 0}\left\{\frac{1}{\Delta\rho^2}\left(V_{i+1,j}-V_{i,j}\right)+\frac{i}{\Delta\rho^2}\left(V_{i+1,j}-2V_{i,j}+V_{i-1,j}\right)+\frac{i}{\Delta z^2}\left(V_{i,j+1}-2V_{i,j}+V_{i,j-1}\right)\right\}=0$$
$$V_{i,j}=V_{i+1,j}\quad(\text{Case }\rho_i=0) \tag{5.10}$$

Otherwise,

$$V_{i,j}=\frac{1}{a_i}\left(b_iV_{i+1,j}+c_iV_{i-1,j}+d_iV_{i,j+1}+d_iV_{i,j-1}\right)\quad(\text{Case }\rho>0), \tag{5.11}$$
$$\text{where}\quad a_i=\Delta\rho\Delta z^2+2i\Delta\rho\Delta z^2+2i\Delta\rho^3,$$
$$b_i=\Delta\rho\Delta z^2+i\Delta\rho\Delta z^2,\quad c_i=i\Delta\rho\Delta z^2,\quad d_i=i\Delta\rho^3$$

The electrostatic potential, $V_{i,j}$, is computed for each point in the grid, except for the diode and ESC walls where potential is kept at constant -1000 V and ground, respectively. The algorithm continues to recalculate $V_{i,j}$ and reiterate through the grid until the grid reaches a stable state and does not change within a desired accuracy. For a grid of size $N \times N$, this method requires order of N^2 iterations through the matrix before it converges to a solution [68].

In order to increase the speed of convergence to a solution, the method of *Successive Overrelaxation* (SOR) with Chebyshev acceleration is applied. SOR introduces the *overrelaxation parameter*, ω such that $1 < \omega < 2$. The overrelaxation parameter is a scalar factor for the updated $V_{i,j}$ which overcorrects in order to converge to the solution quicker. For the first pass through all the grid points, ω is initially 1 (no correction), and it increases gradually with each pass through the grid. SOR shrinks the required number of iterations

to order of N, which is a significant improvement for large grid sizes. The algorithm is explained in more depth in Chapter 19 of [68]. For reference the MATLAB code calculating the potential is provided in Appendix B. A log scale plot of the equipotential lines are shown in Figure 5.2a.

The electric field is then simply the gradient of the potential, and is computed using finite differences on the grid of potentials,

$$\begin{aligned} \mathbf{E} &= -\nabla V \\ \mathbf{E} &= -\left(\frac{\partial V}{\partial \rho}\hat{\boldsymbol{\rho}} + \frac{1}{\rho}\frac{\partial V}{\partial \phi}\hat{\boldsymbol{\phi}} + \frac{\partial V}{\partial z}\hat{\mathbf{z}}\right) \\ E_\rho &= \frac{V_{i,j} - V_{i+1,j}}{\Delta\rho}; \quad E_z = \frac{V_{i,j} - V_{i,j+1}}{\Delta z} \end{aligned} \tag{5.12}$$

Lines indicating direction of field and the modulus field strength from this model are shown in Figures 5.2b and 5.2c respectively.

5.2 Simulation of Polonium Ions in Gas

5.2.1 Generation and Losses to the ESC Walls

The α-decay of ^{222}Rn results in ^{218}Po, of which $65 \pm 5\%$ are positively charged ions [67]. In the ESC model, the position of a ^{222}Rn atom α-decaying is chosen at random in Cartesian coordinates until the values lie within the ESC chamber. If the $^{218}Po^{+}$ ion is successfully created within the ESC chamber, its position is converted to Cylindrical coordinates and allowed to recoil in a random direction.

The ions are released with 100.48 ± 0.30 keV of recoil energy [56]. The recoil of the

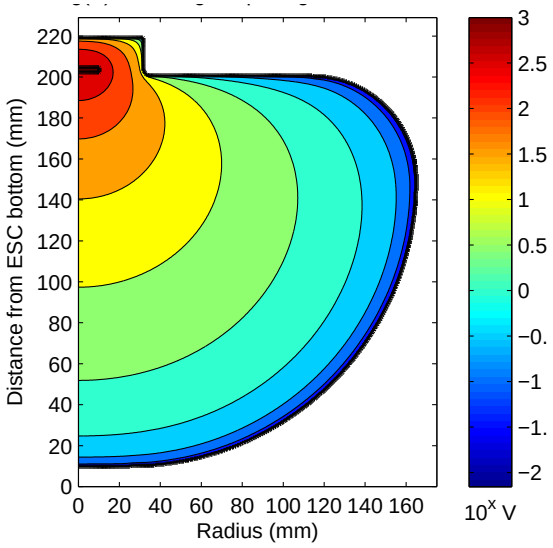

(a) Logarithm of electric potential in Volts.

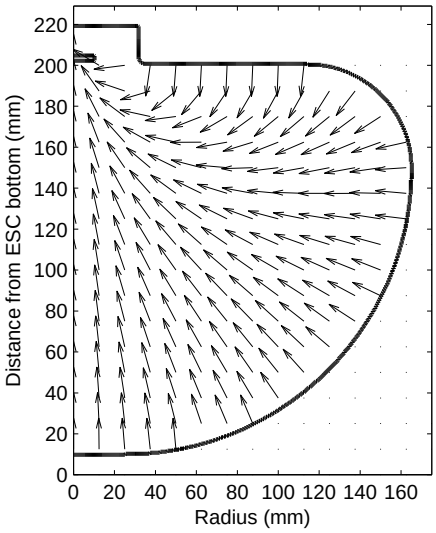

(b) Vectors indicating direction of electric field (not magnitude).

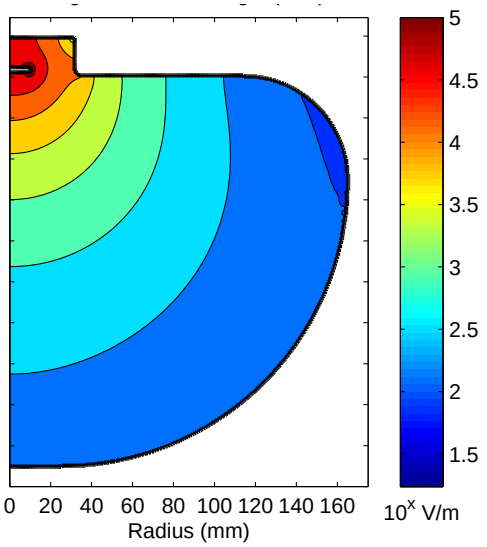

(c) Logarithm of field strength in V/m.

Figure 5.2: Electric potential and field inside the ESC. Due to cylindrical symmetry, this cross-section is the same for all ϕ.

progeny could send some ions to the ESC wall before they have a chance to thermalize and drift towards the diode. Information in the literature is sparse for the recoil range for ions of such low energy in gas. The Bethe formula could be attempted to calculate the stopping power, but the formula breaks down for energies below ∼10 MeV. Reviews from Chapter 30 of [35] suggest Lindhard and Scharff's model to be a fairly accurate representation of stopping power in the 100 keV region. From Lindhard and Scharff, stopping power decreases to approximately 20 MeV cm^2/g, which translates to a recoil range of 1 mm for $^{218}Po^+$ in 1 atm of N_2 gas. The range decreases further for Xe gas due to it's nearly five-fold increase in density. The model estimates a 1 mm recoil range for both carrier gases. This makes for very few ions to be lost from recoiling into the ESC wall. The effect is marginal, although it would be noticeable at lower pressures.

5.2.2 Losses by Decay-In-Flight

The ^{218}Po ion produced has a half-life of $T_{1/2} = 3.098 \pm 0.012$ min [56]. This is incorporated in the simulation by generating an exponentially-distributed random number for each ion produced. This pre-determined lifetime is checked after each time-step in the simulation to verify that the ion has not yet decayed before reaching the diode (Figure 5.3). If it has decayed before reaching the diode, the ion is counted as having "decayed-in-flight" and the simulation starts over for a new ion.

5.2.3 Losses by Neutralization

There is also the chance of neutralization of $^{218}Po^+$ on its trajectory towards the diode, which would render it undetectable. There are at least three mechanisms that have been observed to cause neutralization [69]. First, $^{218}Po^+$ will recombine with small negative ions

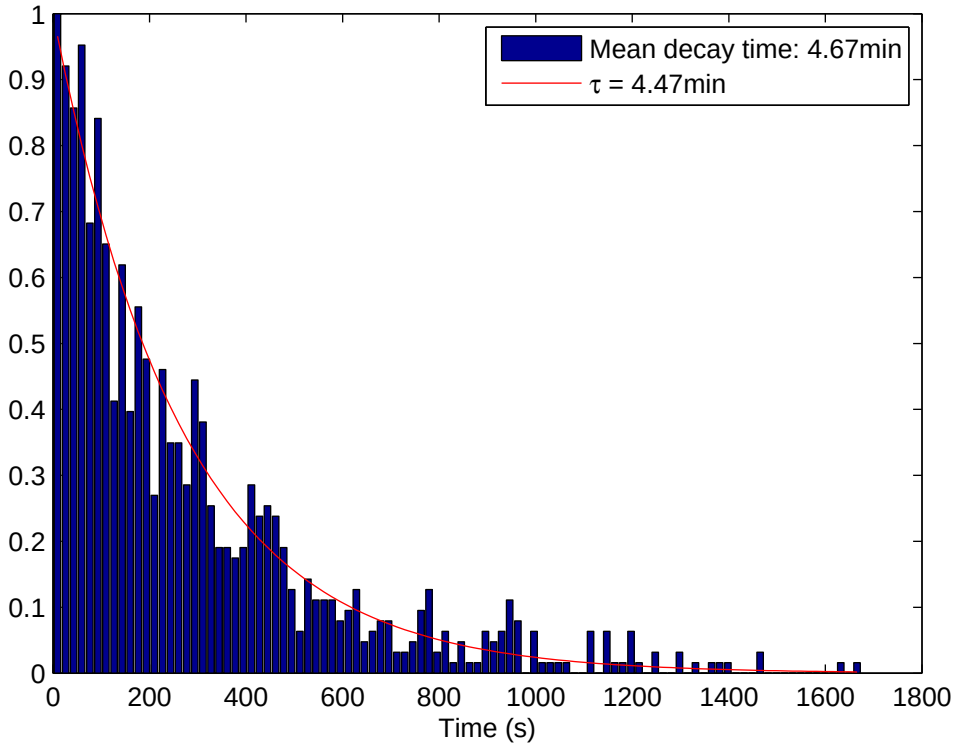

Figure 5.3: A sample of 1000 ^{218}Po ions produced in the simulation, with their lifetimes generated at random based on the half-life. The histogram shows the decay time of the ions, normalized to the highest occurrence. The red line is simply $e^{-t \ln 2/\mathrm{T}_{1/2}}$.

from Rn-decay. Chu and Hopke measured the neutralization rate of $^{218}Po^{+}$ to increase proportionally to the square-root of the concentration of radon. Second, Po ions can be neutralized by water vapour or NO_2 in nitrogen, as well as in air. The cause of this neutralization is attributed to trace gas molecules which scavenge electrons from the Po recoil path and transfer the electrons to the ion. The presence of water vapour in the system would allow hydroxyl radicals to form from radiolysis and the following reaction would occur:

$$\begin{aligned} H_2O &\rightarrow H\bullet + \bullet OH \\ \bullet OH + e^- &\rightarrow \bullet OH^- \\ \bullet OH^- + Po^+ &\rightarrow Po + \bullet OH \end{aligned} \tag{5.13}$$

The last observed mechanism for neutralization of $^{218}Po^+$ comes from the presence of oxygen, which rapidly binds to Po, forming PoO_2^+. This PoO_2^+ then has a higher ionization potential (IP = 10.440 ± 0.054 eV [69]) for removing an electron from other nearby impurities in the gas (e.g. from NO_2 which has an IP = 9.586 ± 0.002 eV [70]).

The last two neutralization mechanisms highlight the importance of purifying the carrier gas before counting Po in the ESC. However, if we assume that we have pure N_2 or Xe gas in the ESC, there is still the chance of recombination of free e^- with $^{218}Po^+$ if the concentration of radon is high enough. Howard and Strange observed neutralization times upwards of 10 s for $^{218}Po^+$ for a range of Rn concentrations, electric field strengths, and carrier argon and helium gas pressures [71]. If we were to take the lowest measured time of 10 s as a worst-case scenario, this still gives ample time for $^{218}Po^+$ ions to drift to the diode ($^{218}Po^+$ ions took on average 2.3 s to drift in 1 atm and -1000 V in the simulation).

5.2.4 Drift

The drift velocity of an ion depends on the ion's mobility which is unique to each ion and carrier gas combination. The ion mobility is defined as [72]:

$$\mu = \frac{q}{k_B T} D \tag{5.14}$$

where q is the charge of the ion, k_B is Boltzmann's constant, T is the gas temperature, and D is the diffusion coefficient of the ion in gas. The diffusion coefficient depends on the diffusional mean free path, λ, and the root-mean-square speed of the atom, ν,

$$D = \frac{1}{2}\lambda\nu \tag{5.15}$$

The mean free path between the two species relates their collisional cross-section, σ, with the number density of the carrier gas, N. The rms speed of the gas ties together Boltzmann's constant, temperature of the gas, and the mass of the drifting ion. Putting these definitions together, we get the following expression:

$$\lambda = (\sigma N)^{-1}, \tag{5.16}$$

$$\nu = \sqrt{\frac{3k_B T}{m}}, \tag{5.17}$$

$$\mu = \frac{q}{2N\sigma}\sqrt{\frac{3}{mk_B T}} \tag{5.18}$$

$$\mu = \frac{qM_{\text{gas}}}{2\rho_{\text{STP}} N_{\text{A}}\sigma}\sqrt{\frac{3}{mk_B T}} \tag{5.19}$$

Equation 5.19 produces a value for mobility of $^{218}Po^{+}$ in N_2 gas of 1.88 cm^2 V^{-1} s^{-1}. This value is in good agreement with the calculation of 1.87 cm^2 V^{-1} s^{-1} from [67], and the value of 2 cm^2 V^{-1} s^{-1} used by [71]. We can thus use this formula for $^{218}Po^{+}$ in Xe gas to obtain μ = 2.68 cm^2 V^{-1} s^{-1}. The drift velocity is now simply the product of the ion mobility μ and the electric field **E**. For each moment in time in the simulation, the nearest grid point to the ion's current position is chosen to represent its electric field before allowing the ion to drift to a new position, closer towards the diode. Time steps in the code are set to 0.1 μs if the ion is within 0.05 m of the diode, 1 μs within 0.1 m of the diode, and 10 μs

otherwise.

5.2.5 Diffusion

Following every step of the Po ion's drift in the electric field, the ion is subject to movement in a random direction in accordance with diffusion theory. For diffusion in three dimensions, the particle's new position is determined by:

$$\sigma^2 = 6Dt \tag{5.20}$$

where σ is the mean squared displacement (MSD), D is the aforementioned diffusion coefficient, and t is the time step. The square root of the MSD tells us how many Gaussian widths the particle will move away from its current position. To find this, a random number is chosen with normal distribution, using the particle's current position as the mean, and the MSD as the standard deviation (the built-in `normrnd()` function in MATLAB comes in handy here). This new position is chosen in terms of radius, r, in Spherical coordinates, with angles θ and ϕ chosen at random. The coordinates are converted back to Cylindrical, which we have been using thus far.

The diffusion coefficients were calculated using Equation 5.14 again. The values obtained were $D = 4.76 \times 10^{-2}$ cm^2/s for $^{218}Po^+$ in 1 atm of N_2, and $D = 6.76 \times 10^{-2}$ cm^2/s for $^{218}Po^+$ in 1 atm of Xe.

5.3 Results and Discussion

With all the transport mechanisms of $^{218}Po^+$ implemented, the simulation was run for ions in 1 atm of each, N_2 and Xe, and with the high voltage held at -1000 V. A sample

Ion Outcome	Buffer gas	
	N_2	Xe
Ions collected (%)	94.5	95.9
Lost on recoil (%)	0.8	0.7
Lost on diffusion (%)	3.4	2.5
Decayed-in-flight (%)	1.2	0.8
Neutralized-in-flight (%)	0.1	0.0
Mean drift time (s)	3.3	2.3

Table 5.1: Ion balance after a simulation of 100,000 $^{218}Po^{+}$ ions generated in the ESC. Simulation performed under a constant −1000 V applied across the PIN diode, and 1 atm of carrier gas. The term "lost" refers to an ion hitting the ESC wall, where it binds and can no longer drift to the diode.

of 100 ions is shown in Figure 5.4. A larger simulation was carried out (without tracking of individual ions) for 100,000 ions in each case. Table 5.1 shows the results of this larger simulation. It's clear that in both instances, the ESC shows a high collection efficiency, 95% for N_2 and 96% for Xe. The two carrier gases show no significant difference. The Xe gas did appear better by one metric though: the mean drift time of ions that reached the diode was 2.3 s versus 3.3 s in the N_2. This would explain the slight discrepancy in decays in flight between the two gases.

The Xe gas performing slightly better is likely due to the faster diffusion and drift constants. One might expect a larger, heavier gas like Xe to cause a *reduced* drift speed, but this was not the case.

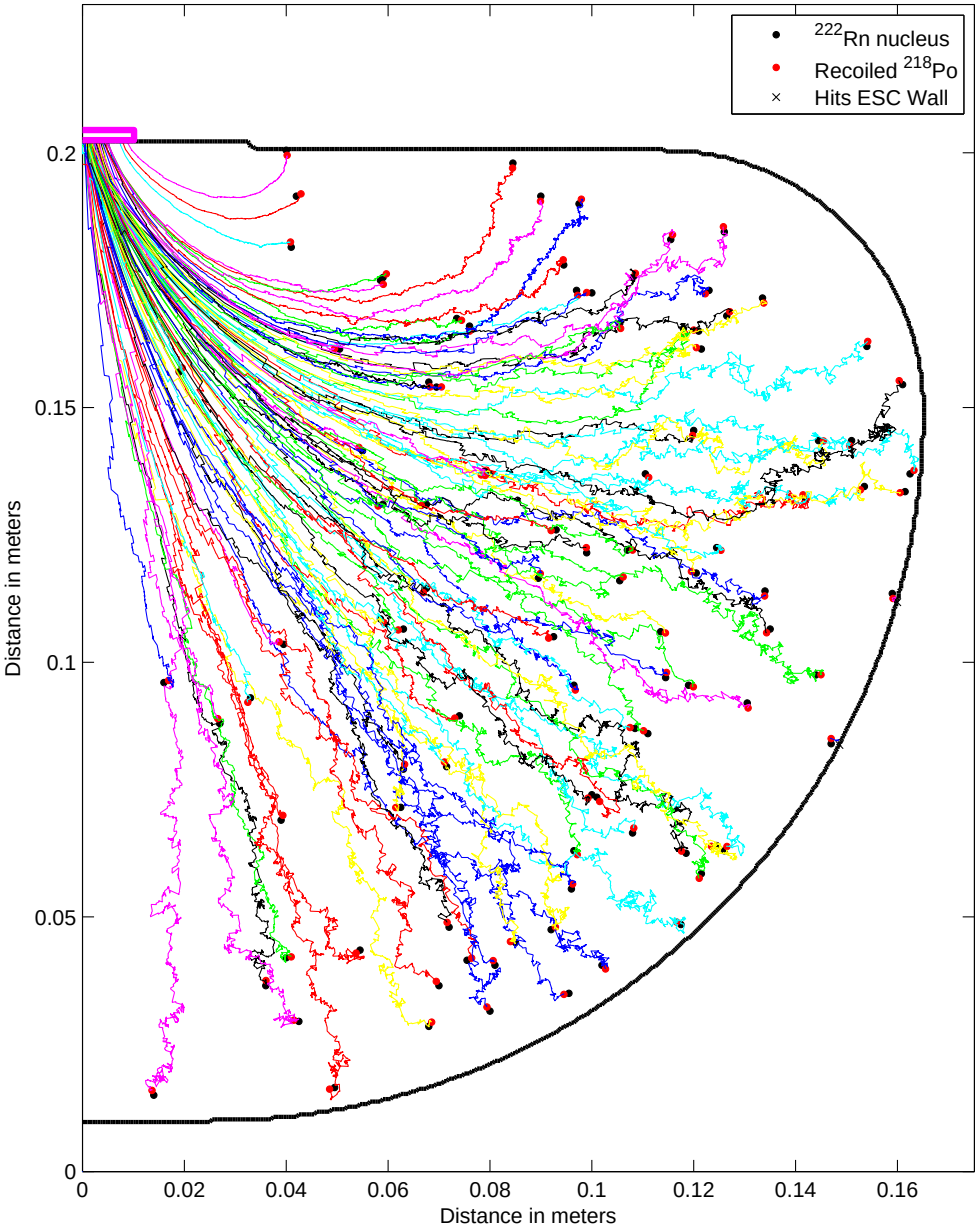

Figure 5.4: The tracks of a sample 100 $^{218}Po^{+}$ ions drifting towards the photodiode (pink rectangle) in the ESC, with the added effect of diffusion. The black dots represent the parent ^{222}Rn nuclei, with the red dots for the recoiled ^{218}Po. "x"s show ions that diffused or recoiled into the ESC wall. However the statistics of 100 ions does not allow any decay-in-flight events here. The coloured lines are the tracks of each ion.

Chapter 6

Processing RnRun Data

6.1 Time Synchronization

Having ESC and LabView data recorded on separate PCs with unrelated clocks implies a time synchronization is needed if we wish to compare the two data sets. There are two offsets that have to be accounted for.

First, due to the DAQ PC not being on any network, and its BIOS battery probably dying, its clock is often drifting forwards and backwards from actual local time. For this reason, a simultaneous reading of the two clocks (and the wall clock too, for good measure) is advisable at the start of any RnRun. The simultaneous times read on the DAQ and LabView PCs are called $t_{\mathrm{DAQ,sync}}$ and $t_{\mathrm{LV,sync}}$, respectively. Both of these times represent the same local lab time, so the absolute difference between them is the first offset:

$$t_{\mathrm{offset,sync}} = |t_{\mathrm{DAQ,sync}} - t_{\mathrm{LV,sync}}| \tag{6.1}$$

$t_{\mathrm{offset,sync}}$ will be added to the dataset from the PC that recorded an earlier time (e.g.

if the DAQ clock is falling behind the LabView clock, the `.SUM` file will have the added offset). The second offset accounts for different relative start times on each PC. The ESC and LabView data runs are not started simultaneously, and when they are started, they each start with their own $t = 0$. The second offset is the time difference between each run start:

$$t_{\text{offset,start}} = |t_{\text{DAQ,start}} - t_{\text{LV,start}}| \tag{6.2}$$

where $t_{\text{DAQ,start}}$ is the first time stamp recorded on the DAQ PC, and $t_{\text{LV,start}}$ is the first time stamp recorded on the LabView PC. The offset is added to whichever PC began their run last. This makes the (chronologically) first PC the reference $t = 0$ for both PCs in the RnRun.

6.2 Rebinning LabView data

A MATLAB script called `rebinLabView.m` was written in order to rebin LabView data to have the same array size as the ESC data. This allows ESC and LabView data sets to be combined or convolved if necessary. This is especially useful, for example, when applying a correction on count rates as a function of pressure from XP-10. Essentially, the script calculates an average around a time window of $\pm\frac{1}{2}$ the width of an ESC interval, and assigns this average as the new binned LabView data. For example, if the count rates were recorded in 20-minute intervals, `rebinLabView.m` will calculate a mean value starting from 10 mins prior to an ESC interval and ending 10 mins later. This will be done for each ESC interval, and for each LabView parameter. The script is provided in Appendix C, along with a diagram of some of the variable names in Figure 6.1.

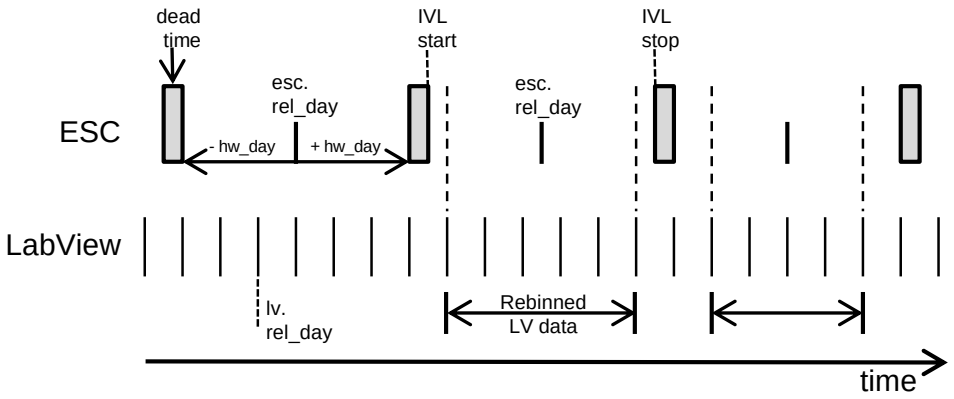

Figure 6.1: Diagram representing variables defined in `rebinLabView.m`. New LabView (LV) bin sizes are chosen to be an average just within the start and stop of each ESC counting interval.

6.3 Corrections

Some corrections have to be applied in order to obtain Rn activities and determine Rn removal efficiencies. The correction for Rn decay is obvious. Another correction is also needed for ESC pressure (XP-10) to account for changes in ϵ_{cntg} during pressure fluctuations.

6.3.1 Radon Decay

Given the ^{222}Rn half-life of $t_{1/2} = 3.8235(3)$ days [73] and XeRn runs that often take several weeks, a correction must be made for the exponential loss of the sample. The correction is made by dividing the count rate by the fraction of sample that should remain after exponential decay, with respect to the relative time since the start of the ESC run.

$$\text{CR}(^{218}\text{Po})_{\text{cor}} = \frac{\text{CR}(^{218}\text{Po})}{e^{-t\lambda}} \tag{6.3}$$

where t represents relative days since start of the ESC run, and λ is the decay constant for ^{222}Rn, related to its half-life by $\lambda = \frac{\ln 2}{t_{1/2}}$. Figure 6.2 demonstrates how we obtain an activity

of Rn after applying this correction.

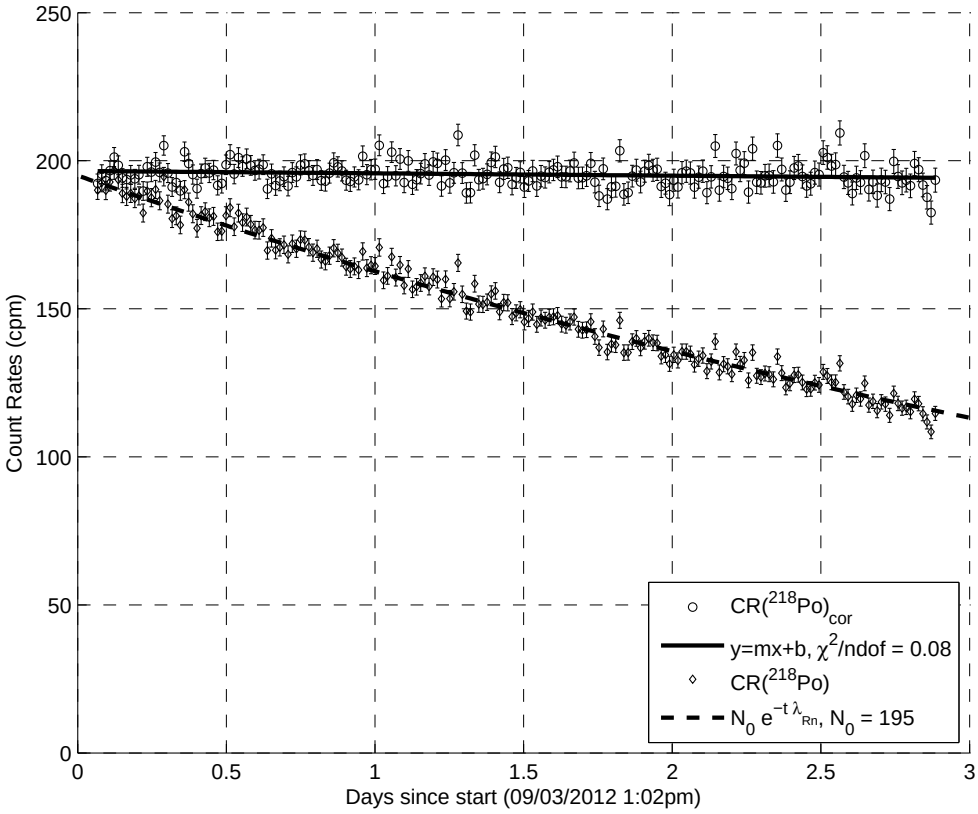

Figure 6.2: Sample baseline from "RnRun CuWool-IX", with and without correction for Rn decay.

6.3.2 Pressure Variation

Changes in pressure were already known to affect the ESC's detection efficiency [62], although the efficiency as a function of pressure was only characterized using a N_2 buffer gas, and not Xe. Data obtained from Dr. Brian Mong and Paul Lamothe shows the change in efficiency as a function of pressure for Xe gas (Figure 6.3). Pressure correction is obtained by fitting the data for pressures greater or equal to 300 mbar, which gives the following:

$$\epsilon_{\mathrm{P}} = \mathrm{A}\log(\mathrm{XP\text{-}10}) + \mathrm{B} \tag{6.4}$$

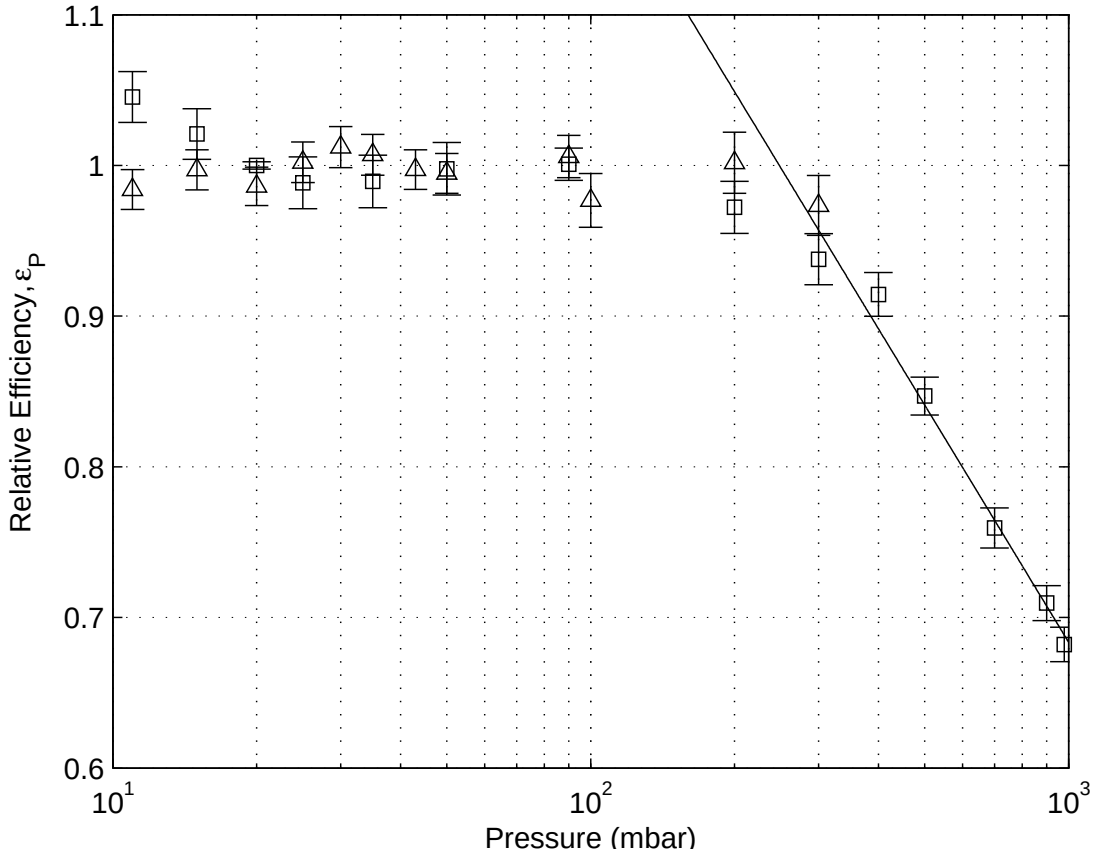

Figure 6.3: Relative counting efficiency of ^{218}Po as a function of pressure. Data was obtained from Paul Lamothe (triangles) and Dr. Brian Mong (squares), and normalized to 20 mbar. The resulting exponential fit applies for ESC Pressures XP-10 $\geq$ 300 mbar. Pressures below 300 mbar are currently not of interest due to our design criteria from Section 3.2.

with $\mathrm{A} = -0.52 \pm 0.03$ and $\mathrm{B} = 2.3 \pm 0.1$. The correction is applied to the ^{218}Po count rate, CR(^{218}Po), by dividing it by ϵ_{P}.

$$\mathrm{CR}(^{218}\mathrm{Po})_{\epsilon_{\mathrm{P}}} = \frac{\mathrm{CR}(^{218}\mathrm{Po})}{\epsilon_{\mathrm{P}}} \tag{6.5}$$

To better understand the drift of ^{218}Po ions in the ESC, it would be beneficial to investigate counting efficiencies for ^{214}Po, which is a progeny of ^{218}Po. However, the time constant from ^{218}Po to ^{214}Po is approximately 3 hours and such a data run would require more time. This would be useful in future work. For the purposes of this work, ^{218}Po counting efficiencies are sufficient.

Chapter 7

Experimental Data

7.1 Early Runs

The first few XeRn Runs for the Cu Wool trap were disregarded from analysis of Rn removal due to early commissioning of the system and hardware upgrades. "RnRun CuWool I" was the first run to test the simultaneous data acquisition of the LabView and ESC systems. Temperature data was sparse in this run, due to flaky barrel connectors that needed replacing. The XeRn gas was also condensed fairly early in the run, which defeats the purpose.

Runs II and III suffered from heater failures on the Cu Spool. The heaters are 5" long flexible polyamide resistive strips by Omega® (model no. KHLV-105/10 08/07). One heater was found to be fried in two places, both where it overlaps on itself, and where the hose clamps were holding it in place (Figure 7.1). The heater was found to have exceeded the maximum operating temperature of 200 °C, most likely due to poor thermal contact with the Cu spool and pressure points introduced by the differential expansion of the Cu spool and stainless steel hose clamps. The surrounding super insulation, which is used to reflect

radiant heat, was also found melted and charred. This could have accelerated heat loss from the heater and further worsened the transfer of heat to the spool. The following actions were taken to prevent this from happening again:

- The heater strip was wrapped staggeringly across the Cu spool to minimize the amount of overlap on itself.
- Cu wire was used instead of stainless steel hose clamps. Having both the spool and clamp made of the same material might eliminate pinch points arising from having different coefficients of thermal expansion. This should also help maintain consistent thermal contact regardless of the temperature of the heater.
- A new RTD, dubbed T11, was installed on top of the securing wire to monitor for the heater not to exceed specified limits. Good thermal contact is necessary for an accurate RTD signal, but this is sufficient for a relative temperature reading. From following runs with the current configuration, a soft limit for T11 was found to be no more than 60 °C (hard limit no more than 100 °C), otherwise there is a risk of frying it again.
- Pink glass wool (building insulation) was used to wrap around the heater, wire and thermocouple since the previous super insulation was found melted.
- The LabView PID control parameters for the heater relay signal were tuned for the fastest response to T1. They were set to be $\mathrm{K_c} = 100.0$, $\mathrm{T_i} = 0.001$, $\mathrm{T_d} = 0.0$, where $\mathrm{K_c}$, $\mathrm{T_i}$, and $\mathrm{T_d}$ represent the PID proportional gain, integral time and derivative time, respectively. More on this below.

The PID Algorithm toolkit in LabView works in principle from the combined gains K_c, T_i, and T_d which help determine the timing of a response to a change in the process variable [74].

Figure 7.1: Heater damage due to poor thermal contact with the copper spool (photo from Dr. Jacques Farine).

For an observed error $e = SP - PV$ between the Setpoint (SP) and Process Variable (PV), The PID calculates the next action for the heater status, $u(t)$,

$$u(t) = K_c \left(e + \frac{1}{T_i} \int_0^t e \, \mathrm{d}x + T_d \frac{\mathrm{d}e}{\mathrm{d}t} \right) \tag{7.1}$$

In practice, the proportional gain K_c is just a linear factor which propagates through each response, always acting in direct and opposite response to the error with the setpoint. The action taken with the integral term, T_i, is actually computed using a trapezoidal sum,

$$u_l(k) = \frac{K_c}{T_i} \sum_{i=1}^{k} \left[\frac{e(i) + e(i-1)}{2} \right] \Delta t \tag{7.2}$$

The motivation behind K_c is to avoid sharp changes in the integral action $u_l(k)$ in an effort to avoid overshooting the setpoint. The derivative term, T_d, only looks to the process variable and computes the next action to take using finite differences,

$$u_D(k) = -K_c \frac{T_d}{\Delta t}(PV_f(k) - PV_f(k-1)) \tag{7.3}$$

The new heater properly installed on the spool is shown in Figure 7.2. Some suggestions for future work:

- A better understanding of the temperature control would be useful. A thermodynamic model of the heat exchanger system along with its interactions with the cold head, heater and temperature control could help prevent future heater failures and for the next point.

- A revamp of the heater block and heater element system. The current design is only meant to operate the system at 1000 mbar of gas. A new design could not only prevent any failures like this from happening, but also allow us to test the trap at lower pressures (order of ∼100 mbar). [1]

- A heater element wire (e.g. from Thermocoax Inc.). The main advantage from one of these is a much higher temperature limit, up to 600 °C, and it can be brazed onto the heating surface for excellent thermal contact. Such a heater element would be sufficient for counteracting the refrigerator's power and testing the Rn trap at low pressures.

7.2 First Copper Wool Trap Test (Run IV)

"RnRun CuWool IV" is a short run which was carried out over March 14 and 15, 2011. The purpose of this run was to lower the temperature of the XeRn gas as much as possible

[1] The option of testing at lower pressure would be useful if we want to improve the efficiency of Rn removal. If we cannot see Rn removal at low pressures, then we will not see it at 1 atm either.

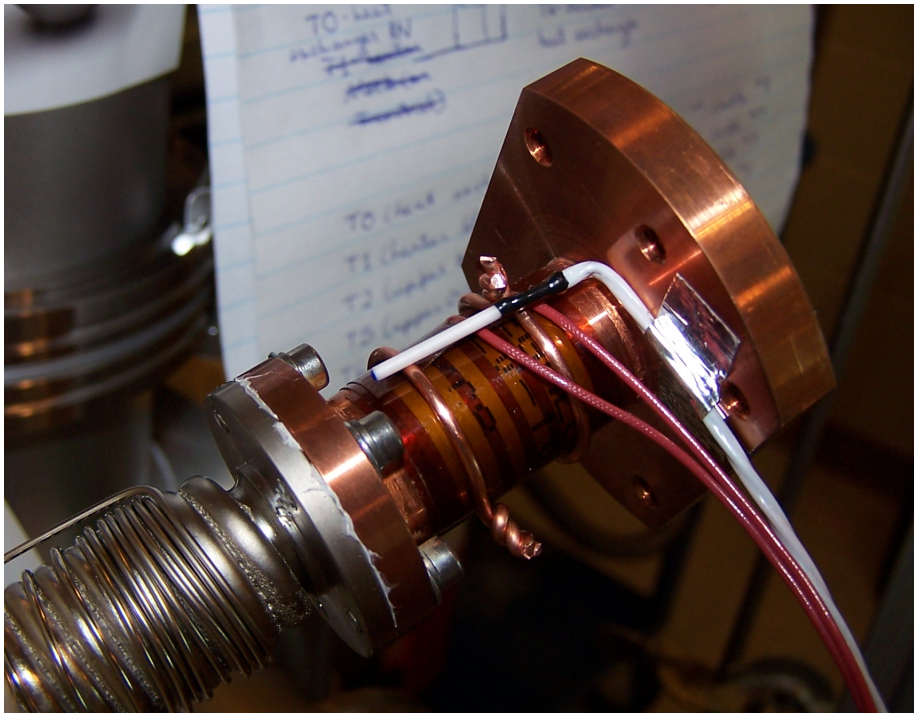

Figure 7.2: New heater tightly wrapped and tied with Cu wire and new RTD used to monitor heater temperature. Super insulation around this ensemble not shown.

without condensing it. The phase diagram of Xe is consulted to determine the condensation point (see Figure 7.3).

Actions performed during the run are provided in Appendix F.1. A summary of relevant actions for RnRun CuWool IV goes as follows:

- Start data acquisition on DAQ and LabView PCs.
- Mix Rn injection into 1000 mbar of Xe.
- Flow through purifier for 26 mins.
- Cool trap to $-100\,^{\circ}\mathrm{C}$, then count first baseline for analysis, called "Region I".
- Cool to $-107.5\,^{\circ}\mathrm{C}$, throttle trap inlet (XRV-11), and count Region II.
- Cool to $-112\,^{\circ}\mathrm{C}$, throttle ESC inlet, and count Region III once ^{218}Po activity stabilizes.
- Re-establishing previous flow, warming up to $-110\,^{\circ}\mathrm{C}$, and count final baseline, Region

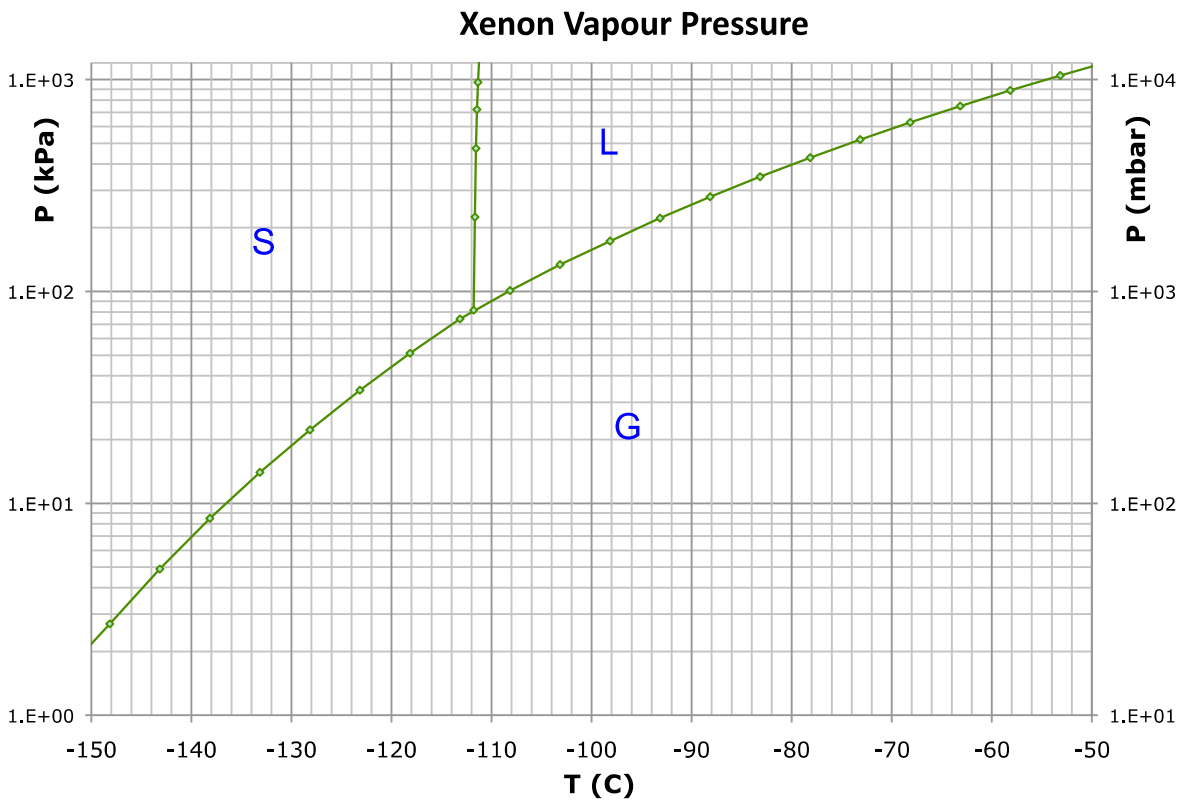

Figure 7.3: Xenon phase diagram

IV.

The most relevant measurements are plotted together with four vertical axes over the same period of time (Figure 7.4). This makes finding correlations simpler. In the first window, ^{218}Po count rates are shown in 5-minute bins after correction for ESC Pressure, as well as the ESC Pressure (XP-10). In the second window, temperatures at the trap inlet (T2), outlet (T5), bottom (T8) and Cu Spool of the heater block (T1) are shown, along with mass flow of the XeRn System (XT-01) and the ESC (XT-02). Appendix A shows the XeRn System Flowsheet with all the aforementioned gauges labelled. Appendix D provides a rough schematic of the plumbing inside the vacuum chamber, with RTD locations labelled.

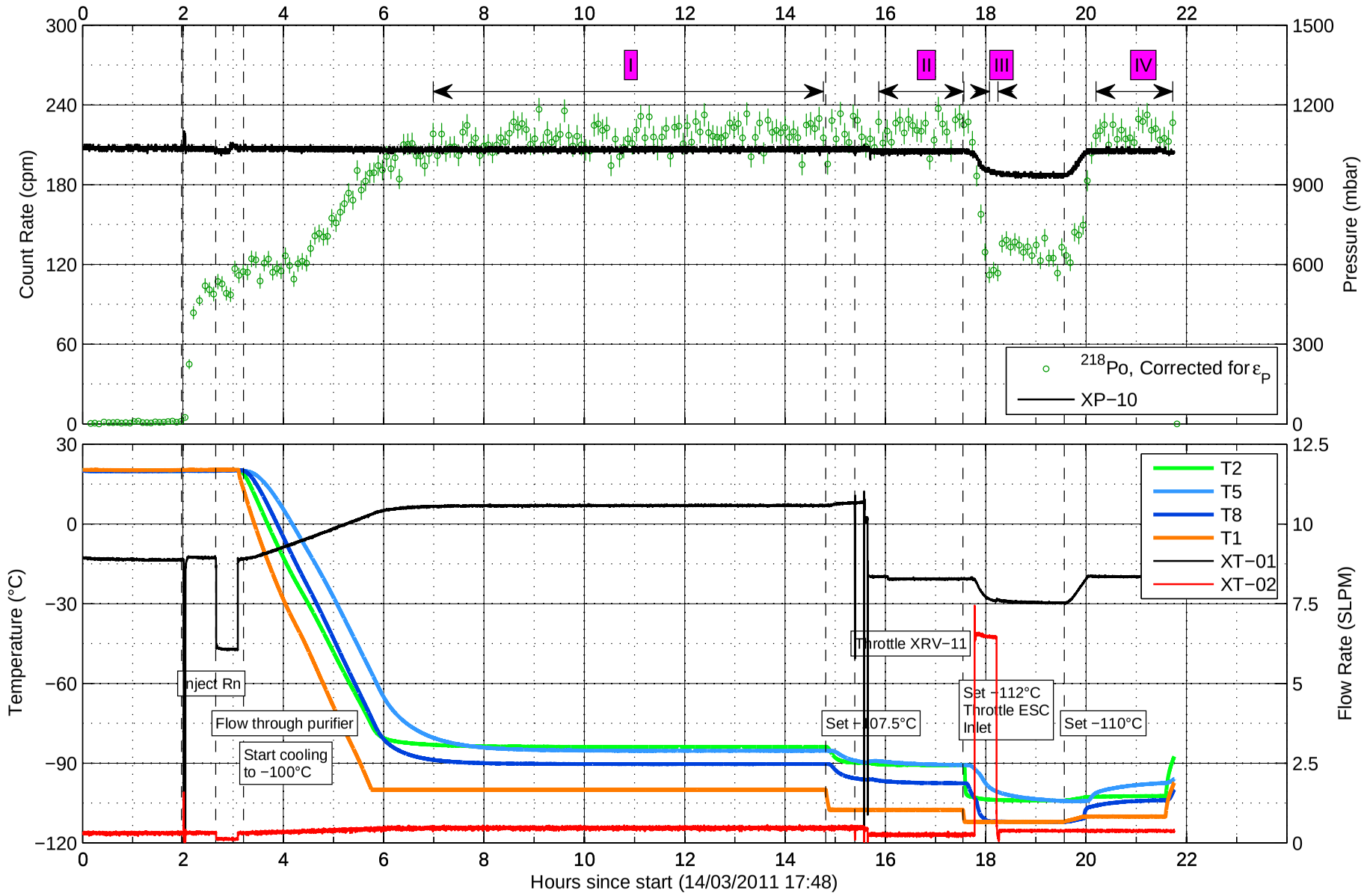

Figure 7.4: Run IV - Trap Test at 1000 mbar

Region	Setpoint (°C)	ESC Pressure (mbar)	ESC Flow (SLPM)	Count Rate (cpm)	Comments
I	−100.0	1030	0.466	216.6 ± 0.9	
II	−107.5	1030	0.254	221.5 ± 1.9	Trap outlet throttled
III	−112.0	950	5.471	113.7 ± 3.5	ESC flow increased
IV	N/A	1030	0.377	219.7 ± 2.0	ESC flow re-established

Table 7.1: Run IV Results

There are four distinct regions of interest in this data run. The regions are selected where all system parameters are stable. There is often a waiting period after a change made to the system before the start of an analysis region due to trap RTDs which slowly reach equilibrium. An analysis region ends whenever a change occurs in the system, such as the operation of a valve or sudden pressure drops from condensation of Xe. Count rates during these regions are shown in Table 7.1.

There is no significant change in ^{218}Po count rates throughout the run, except by Hour 18 (Region III). For this region, the setpoint was lowered to −112.0 °C which could have caused the Xe to condense. A closer look at T8 in Figure 7.5 supports this idea. The setpoint was decreased by 4.5 °C, and T1, our temperature process variable, reacted accordingly. Meanwhile, T8, which is located at the bottom of the trap, decreased by nearly 15 °C, and now reads −112 °C, just like T1. This suggests that T8 is now reading the temperature of the xenon more accurately, as a result of a phase change of the gas, and liquid xenon is resting at the bottom of the trap.

A decrease in amount of Xe can be quantified from the ideal gas law:

$$\Delta n = \frac{\Delta PV}{RT} \tag{7.4}$$

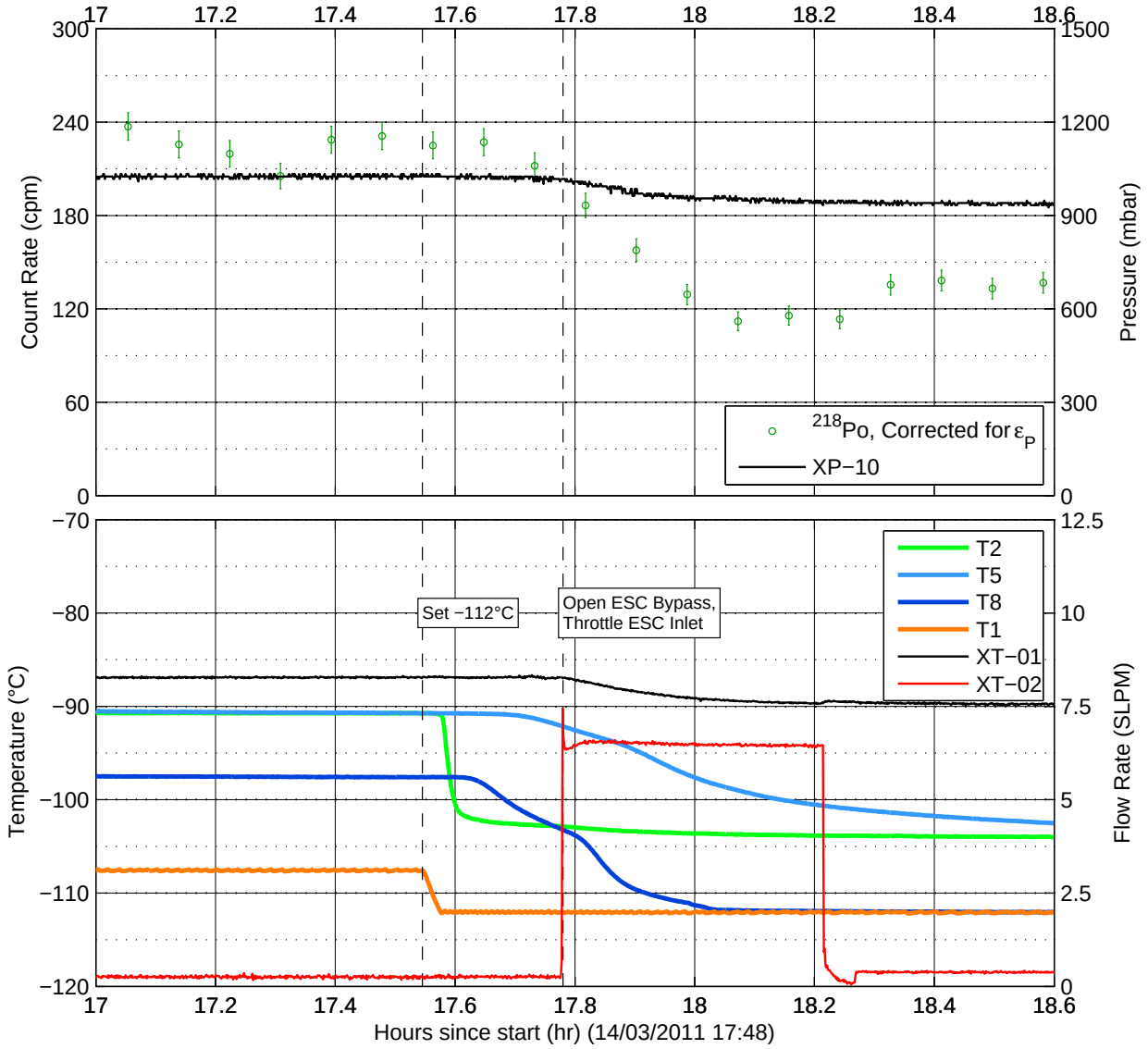

Figure 7.5: Run IV - Condensation of xenon after 17.6 hours

where ΔP is taken from XP-10 since this is a closed system and the change in overall volume of the gas in the system is assumed to be negligible. Using $V = 11$ L, $T = 161$ K, and $\Delta P = 80$ mbar, we can tell that the amount of Xe condensed was 64 mmol. Given the density of liquid xenon of $\rho_{\mathrm{LXe,b.p.}} = 3057$ g/L, this equates to a volume of 2.8 mL, which

is negligible compared to the volume of the XeRn system. Assuming the remainder of the gaseous Xe has a density of $\rho_{\mathrm{GXe}}(15\,^{\circ}\mathrm{C}, 950\ \mathrm{mbar}) = 5.235\ \mathrm{g/L}$, and thus the XeRn system contains 439 mmol, the percent amount of Xe condensed is 15 %. This is not enough to account for the 49 % decrease in ^{218}Po count rate.

The best way to verify whether any Rn was actually removed is by restoring initial conditions and comparing count rates before and after. Comparing count rates from Regions I and IV, where setpoints were $-100.0\,^{\circ}\mathrm{C}$ and $-110.0\,^{\circ}\mathrm{C}$, before and after condensing Xe, we see there was -1.4 ± 3.4 % Rn removal.

To rule out Rn removal from condensation or from loss in counting efficiency, a new run was performed, controlling for flow of the gas through the ESC inlet and approaching the condensation point of Xe more cautiously.

7.3 Second Attempt with the Copper Wool Trap (Run V)

"RnRun CuWool V" was carried out from April 4 to 8, 2011. Data was collected for longer time intervals in order to acquire better statistics on count rates as the condensation point was approached. Actions performed during the run are listed in Appendix F.2. In short RnRun CuWool V went as such:

- Start data acquisition on DAQ and LabView PCs.
- Mix Rn injection into 1000 mbar of Xe.
- Flow through purifier for 15 mins.
- Cool to $-100\,^{\circ}\mathrm{C}$, and count Region I.
- Suspected Xe condensation after setting setpoint to $-120\,^{\circ}\mathrm{C}$.

- Warmed and cool again to $-112\,^{\circ}\mathrm{C}$, count Region II.
- Cool to $-113\,^{\circ}\mathrm{C}$ and count Region III.
- Count final baseline, Region IV, after re-establishing previous flow and warming up to $-110\,^{\circ}\mathrm{C}$.
- Warm up to room temperature and count final baseline, Region IV.

The bulk of data for this run is shown in Figure 7.6. It may appear that Rn is being removed progressively with each decrease in setpoint (the count rates of ^{218}Po are certainly falling accordingly). However, it is worth mentioning that there were a few instances where Xe was condensed (notice brief drops in XP-10). See Table 7.2 for a summary of results.

The final comparison for Rn removal is between Regions I and III and we find there was 31.1 ± 0.7 % Rn removal, with an 40 mbar decrease in pressure. This equates to 7.5 % Xe condensation, using the same calculation as in the previous run. Refrigeration was turned off by Region IV to ensure that nominal count rates could be recovered, and it was not necessarily the case. 4.1 ± 2.9 % Rn was not recovered from Regions I to IV. There was some unaccounted loss somewhere, although the statistics is also poor on the last region.

The Rn removal from Regions I to III looks promising, although not without its caveats. Some Rn removal may be attributed to condensation, and some Rn was not recovered in the end. Nonetheless, there was 19.5 ± 3.6 % indicative of Rn removal by adsorption.

This is still far from the desired 99.99 % efficiency. From here it was decided it was not worth testing with the Cu spheres trap due to the spheres having the same surface quality as the wool, unless the Cu spheres are first reduced. An increase in adsorption enthalpy of Cu by $\sim$10 kJ/mol was shown to be possible by Eichler and Schädel, which would increase the sojourn time of Rn [59]. Their method involves heating the trap to 1000 K for 2 hours, flowing a mixture of $N_2 + H_2$ (90 : 10 vol%) at 100 mL/min.

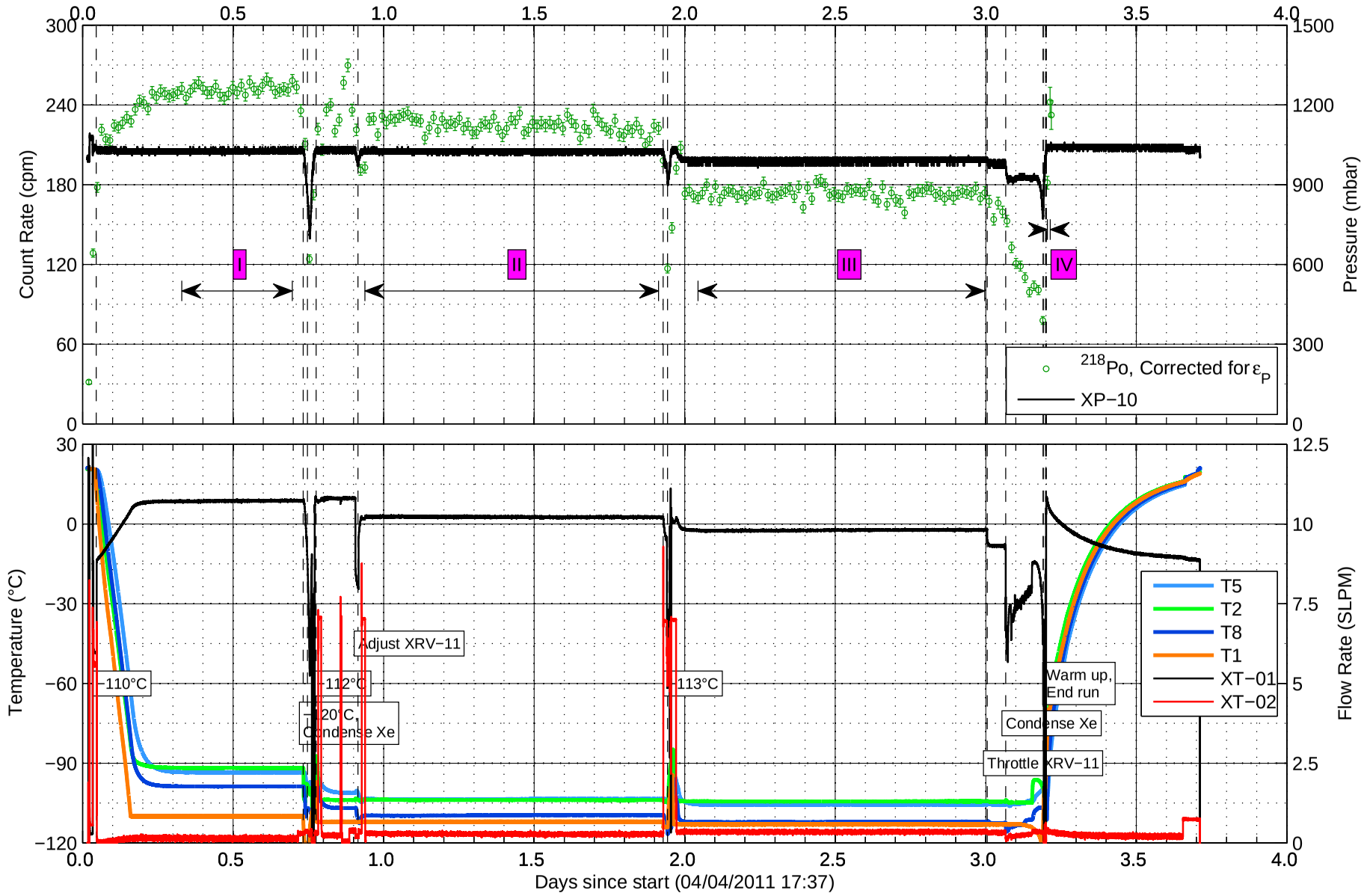

Figure 7.6: Run V - Trap Test at 1000 mbar

Region	Setpoint (°C)	ESC Pressure (mbar)	ESC Flow (SLPM)	Count Rate (cpm)	Comments
I	−100.0	1030	0.136	251.9 ± 0.9	
II	−112.0	1020	0.283	224.8 ± 0.6	Trap outlet throttled
III	−113.0	990	0.346	173.4 ± 0.5	
IV	−110.0	1040	0.346	241.5 ± 6.4	Trap warming up
19.5 ± 3.6 % removal from adsorption (Region I → III)					

Table 7.2: Run V Results

While a reduction system is being set-up, in the meantime, the current Cu wool trap can be conditioned without removing it from the XeRn system. This will be explained in the next section.

7.4 Trap Conditioned with Helium (Run VI)

With the trap still mounted in the vacuum enclosure, the vacuum enclosure was opened and a heater sleeve was wrapped around the trap. The gas in the XeRn system was evacuated and the trap was flushed with He gas. The temperature sensor on the heating sleeve read 191 °C (464 K) at its highest. He gas was flushed for 2 hours, 45 minutes before turning off the heater, removing the heater, and re-enclosing the vacuum enclosure.

"RnRun CuWool VI" was carried out from May 9 to 18, 2011. The goal of this run was to observe Rn removal from the Cu wool trap as before, and to see if the He conditioning had any effect. The conditioning procedure was not expected to remove oxides from the Cu wool, but possibly anneal the Cu surfaces slightly to have a higher adsorption enthalpy for Rn. The full actions are provided in Appendix F.3. In short, these actions were performed:

- Start data acquisition on DAQ and LabView PCs.

- Same Rn injection from previous run used, in 1100 mbar of Xe.
- Flow through purifier for 20 mins.
- Cool to $-100\,^{\circ}$C, and count Region I.
- Cool to $-113\,^{\circ}$C, and trigger condensation.
- Warm up in small increments to boil off Xe, but ice plug continues to cause flow interruptions.
- Warm to $-100\,^{\circ}$C to fully boil off Xe, and count Region II.
- Cool to $-110.9\,^{\circ}$C and count Region III.
- Cool to $-111.0\,^{\circ}$C and count Region IV.
- Cool to $-111.1\,^{\circ}$C and count Region V.
- Warm up and count Region VI with trap at room temperature.

The plan was not initially to trigger a condensation. However, it's clear that after the first 23 hours of the run, shortly after changing the setpoint to $-113\,^{\circ}$C and throttling the trap outlet, that Xe starts to condense. We can see this in Figure 7.7 when the ESC Pressure (XP-10) starts to fall, along with similar changes in temperatures and flows. Setpoint was changed back to $-112\,^{\circ}$C to reverse the condensation, but XP-10 did not recover to initial values.

Following the setpoint change, we suspected the setpoint to be very close to re-evaporating the xenon. The voltage readings for pressure upstream of the trap read 127 mV at their highest, corresponding to 680 mbar. The condensation point of Xe at this pressure would be no higher than $-113\,^{\circ}$C, according to the Xe phase diagram (Figure 7.3). Adding to this, the pressure at the coldest point in the plumbing of the vacuum enclosure must also be lower than the pressure upstream. A linear interpolation of the pressure between the gauges would reveal a pressure closer to $\sim$530 mbar, or a T_{cond} of $-116\,^{\circ}$C. Nonetheless, ESC pressure

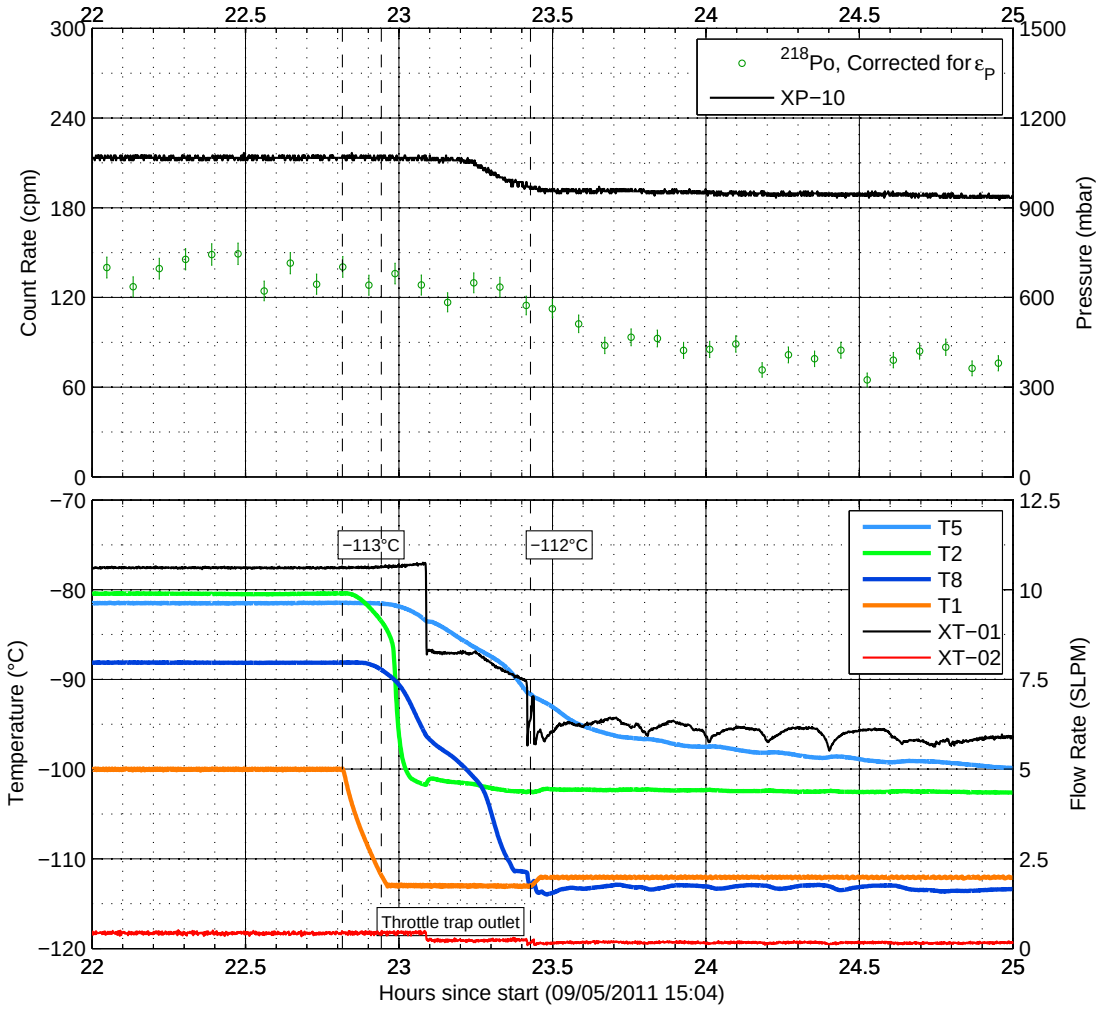

Figure 7.7: Condensation of xenon after 23.2 hours

did not yet recover after warming up to −112 °C and irregularities in flow began shortly thereafter.

The plan for the run was re-adapted to this idea that we must be very close to the condensation point, just barely in the liquid phase. The goal was to increase the setpoint in small increments until full re-evaporation of the liquid occurs, and we would know empirically what setpoint to approach from the gas phase. Until then, periodic flow interruptions

persisted from days 1 through 3, where flow would surge, followed by a sharp collapse, and recovery. Similar effects were observed with RTDs on the gas flow tubing (see run summary in Figure 7.8).

These flow interruptions are interesting for the purposes of understanding the operation of the XeRn system, since they were unprecedented. The first of these events is shown in Figure 7.9. Looking at correlation plots for the same period of time (Figure 7.10) helps us establish the causality chain. XT-01 (system flow) is the first parameter to be affected: spiking and collapsing before XT-02 (ESC flow) takes a similar route. The temperature sensors rise and slowly fall back to previous values in response. The first RTD to react is T2, followed by T8, and lastly T5, all in the direction of flow of the gas.

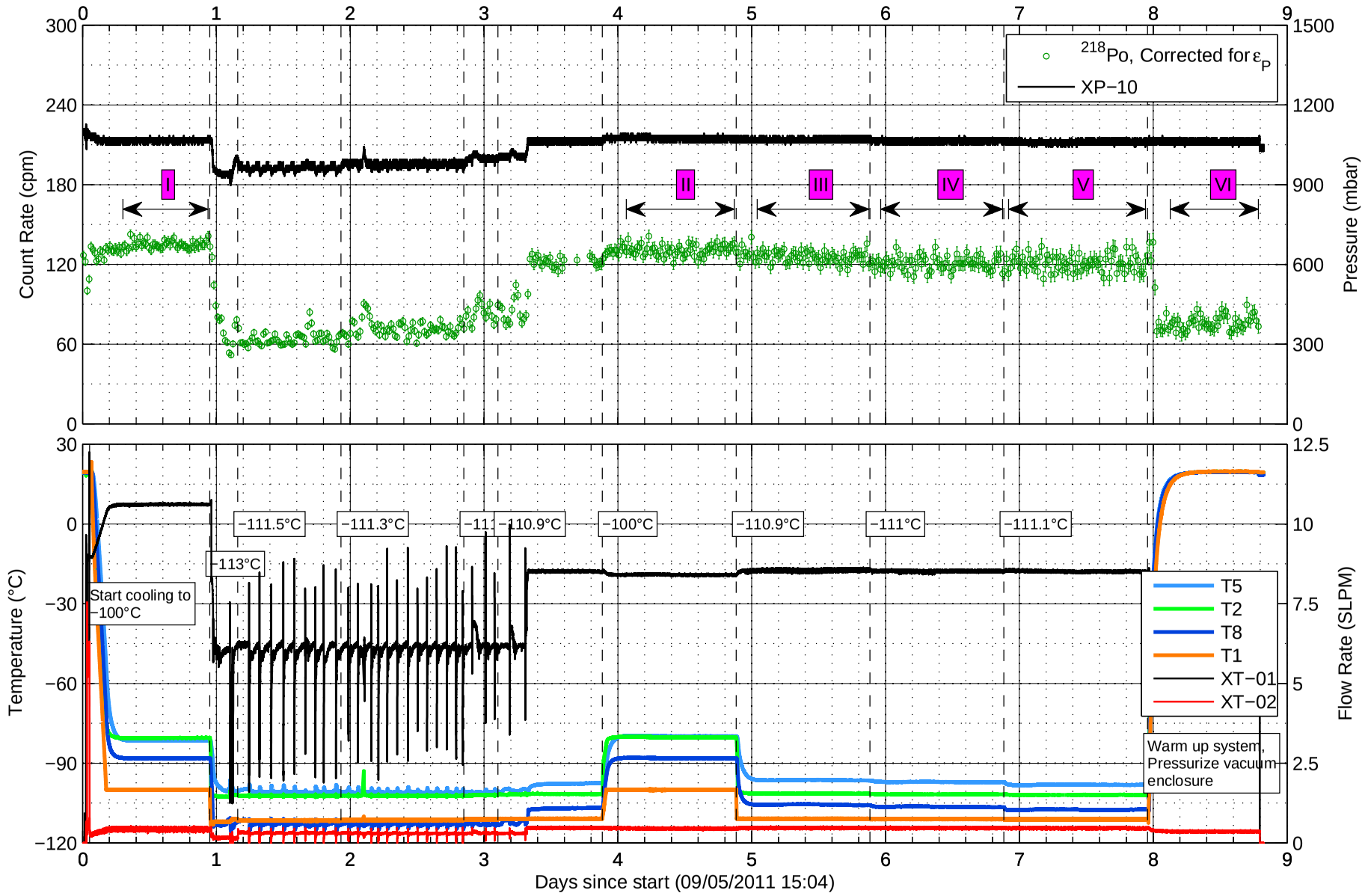

Figure 7.8: Run VI - Trap Conditioned with He

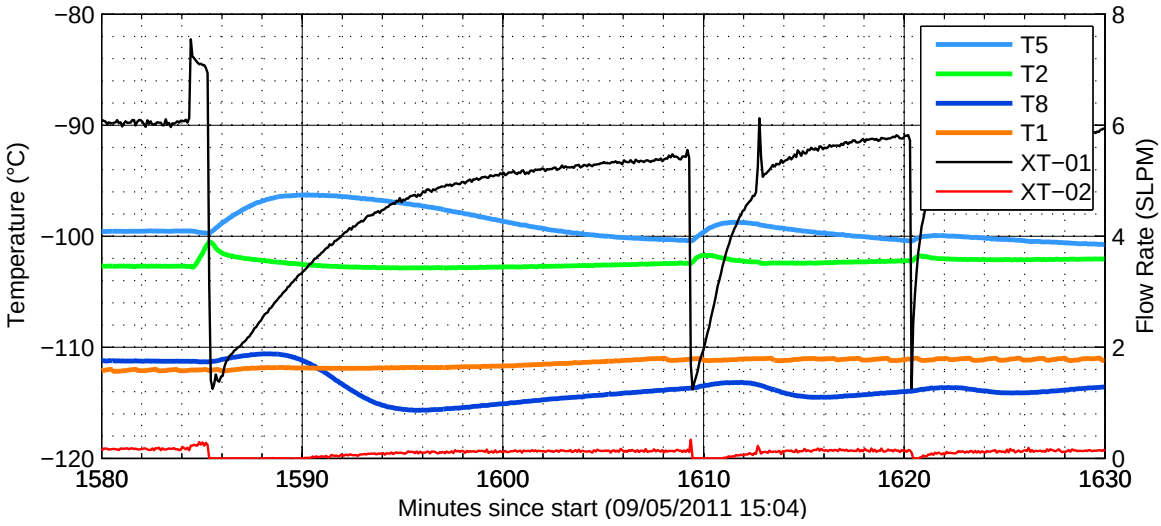

Figure 7.9: The first of several flow interruptions, shortly after the first day elapsed.

It is likely that these flow interruptions were the result of solid Xe formed in the plumbing near the Cu spool, just before the trap inlet (closest RTD is T2). For days 1 through 3, the build-up of ice was enough to cause a plug periodically, which took a pressure build-up upstream to dislodge. The result is then seen in the RTDs downstream as the surge of XeRn travels through the trap. The periodicity of approximately 1 hr, 40 min for these events is uncanny. These flow interruptions hint that the XeRn system may not be suitable in its current configuration to test Rn removal in the liquid phase, since solid ice might form too easily. However, future tests could prove otherwise.

The remaining Xe is presumed to be boiled off after the setpoint is set to $-110.9\,^{\circ}\mathrm{C}$ following day 3. For the purpose of Rn removal from gaseous Xe, the run was able to continue with the knowledge that $-110.9\,^{\circ}\mathrm{C}$ is the new condensation point to approach. A baseline was counted again to establish Rn levels at a nominal $-100\,^{\circ}\mathrm{C}$. The remaining analysis regions were then counted for several setpoints around the condensation point. The resulting count rates for analysis regions are shown in pink in Figure 7.8 and quantified in

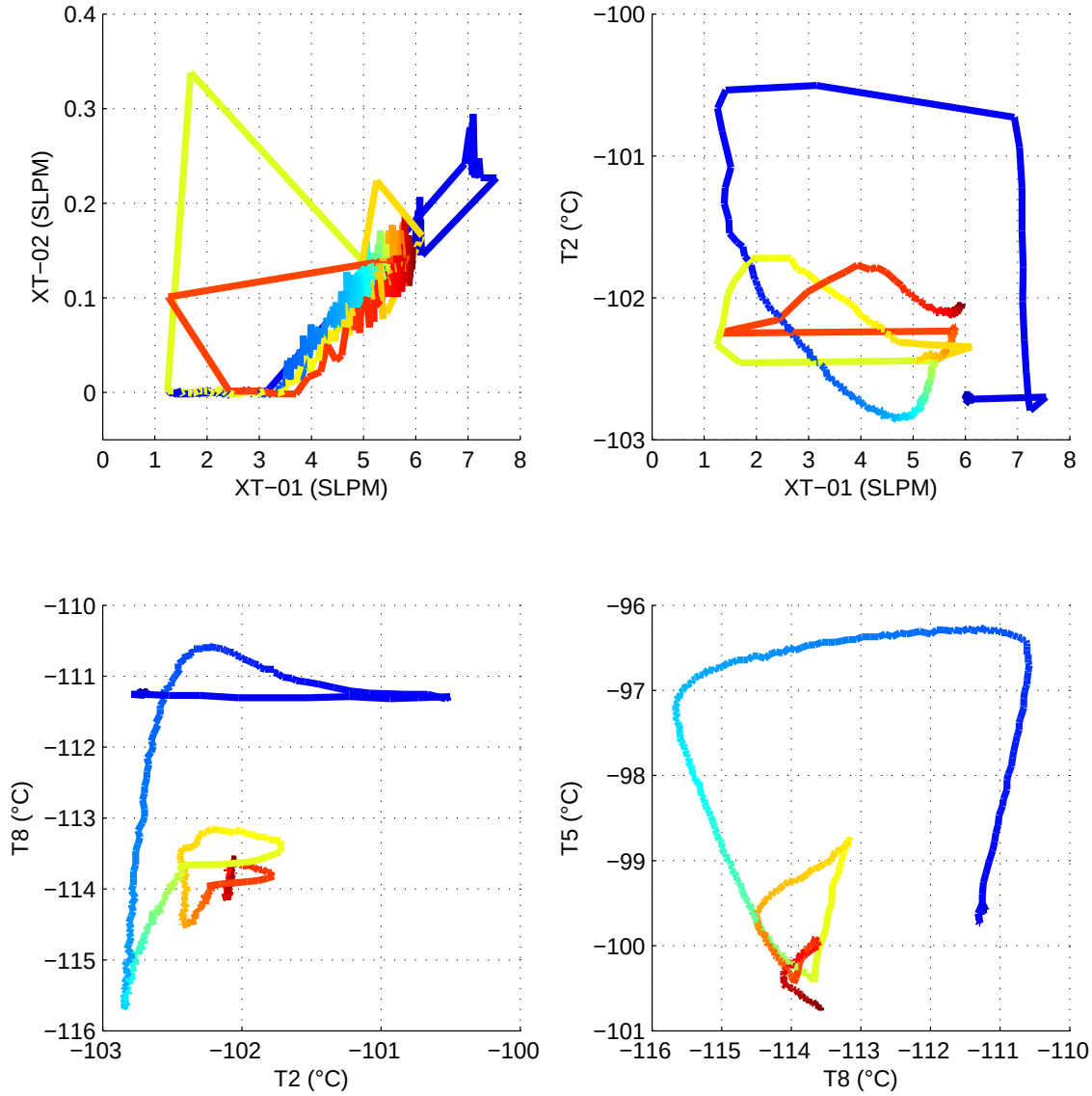

Figure 7.10: Time evolution (early to late, from blue to red) of temperatures and flows for the first flow interruption. Time period taken from Figure 7.9. Notice how the horizontal axis parameter usually changes first, before any change in the vertical axis. This illustrates the propagation of temperature changes going from the trap inlet towards the outlet. It would also be safe to assume the dependence of T2 (as well as other RTDs) on XT-01.

Table 7.3.

The largest Rn removal throughout the gaseous phases occurs between Regions II to V;

Region	Setpoint (°C)	ESC Pressure (mbar)	ESC Flow (SLPM)	Count Rate (cpm)	Comments
I	−100	1070	0.432	135.0 ± 0.5	First baseline
II	−100	1070	0.450	130.6 ± 0.6	Recovered from condensation
III	−110.9	1070	0.464	125.5 ± 0.6	
IV	−111.0	1060	0.461	120.8 ± 0.7	
V	−111.1	1060	0.458	120.8 ± 0.7	
VI	N/A	1060	0.234	76.2 ± 0.7	Warm up, pressurized vacuum
					7.5 ± 1.0 % removal (Region II → V)

Table 7.3: Run VI Results

an apparent 7.5 ± 1.0 % Rn removed. The main problem with this result is that Rn is significantly lost when trying to re-establish nominal conditions. Future tests should include a final baseline with the same conditions as the first baseline to see whether count rate is restored or not. Region VI defies what we would have expected, since it is a sudden drop in ^{218}Po after an increase in trap temperature from warming up to room temperature. The cause of this is not likely to be Rn removal from the Rn trap. For the time being, we suspect this to be caused by the venting of the vacuum which might have thermally shocked the trap and its fittings, possibly leaking out some XeRn gas. However, this remains unconfirmed.

7.5 Reduced Copper Wool Trap Test (Run VII)

A reduction system was installed in the SNOLAB facility at the Fraser building at Laurentian University by Dr. Brian Mong. Special care was taken to install the reduced Cu wool trap, keeping the wool from getting exposed to air and being oxidized again. A ball valve was installed before XRV-47 to supply argon gas for the installation. The xenon in the system had to be recovered to the expansion tank, then when the newly reduced trap was

ready for installation, a positive pressure of Ar was supplied to flow outward of the two trap openings in the vacuum enclosure.

Replacement diaphragm sensors were also installed for pressure gauges upstream and downstream of the trap, XP-18 and XP-19 respectively. These are both Pirani type vacuum gauges from Cole-Parmer Canada Inc. (sensor model #68801-53, controller model #68801-03). Pressures at these locations can now be recorded digitally and continuously during the length of a RnRun. The LabView program was also modified to read these new sensors.

Following these improvements, we were ready for "RnRun CuWool VII", where the properly reduced Cu wool trap will be tested. The data run lasted from January 27 to February 07. A full list of actions is found in Appendix F.4. The condensed list of actions is as follows:

- Mix Rn injection in 1000 mbar of Xe.
- Start data acquisition on DAQ and LabView PCs.
- Purify XeRn gas.
- Count first baseline at room temperature, Region I.
- Cool to $-100\,^{\circ}\mathrm{C}$ and count Region II.
- Change setpoint to $-112\,^{\circ}\mathrm{C}$, still counting Region II.
- Cool to $-113\,^{\circ}\mathrm{C}$, and condensation triggered.
- Warm to $-112\,^{\circ}\mathrm{C}$. Notice Xe evaporate and count Region IV.
- Warm up to room temperature and count final baseline, Region V.

The full run results are available for most variables in Figure 7.11 and count rates are shown in Table 7.4. There was a hiccup with the pressure gauges initially. XP-10 was noisy due to poor electrical contact. There is a sharp drop in XP-10 at $\sim$2.3 days where a corresponding drop occurs to ^{218}Po levels. The wires for the newly installed XP-18 and XP-19 gauges were also swapped initially on the DAQ input module. The problem was fixed

and the proper labels are reflected in Figure 7.11. However, there is still a brief jump at the 3-day mark when the gauges were physically swapped on their controllers (from a brief signal interruption).

^{218}Po count rates were calculated for 5 regions of interest during the run. However, regions I through III do not provide reliable baselines for count rates because 2nd order effects are at work here. Region I was intended as an initial baseline at room temperature, but to our surprise there was a clear rate of decrease in the ^{218}Po. Region II saw similar affects as Region I, and although one could argue that Region II should be further subdivided for its range of setpoints, the effect is seen throughout these setpoints. If there is any Rn trapping taking place in this region, it is evidently a very inefficient Rn removal process. This behaviour was thus labelled "faster-than-Rn decay" until a better explanation is proposed.

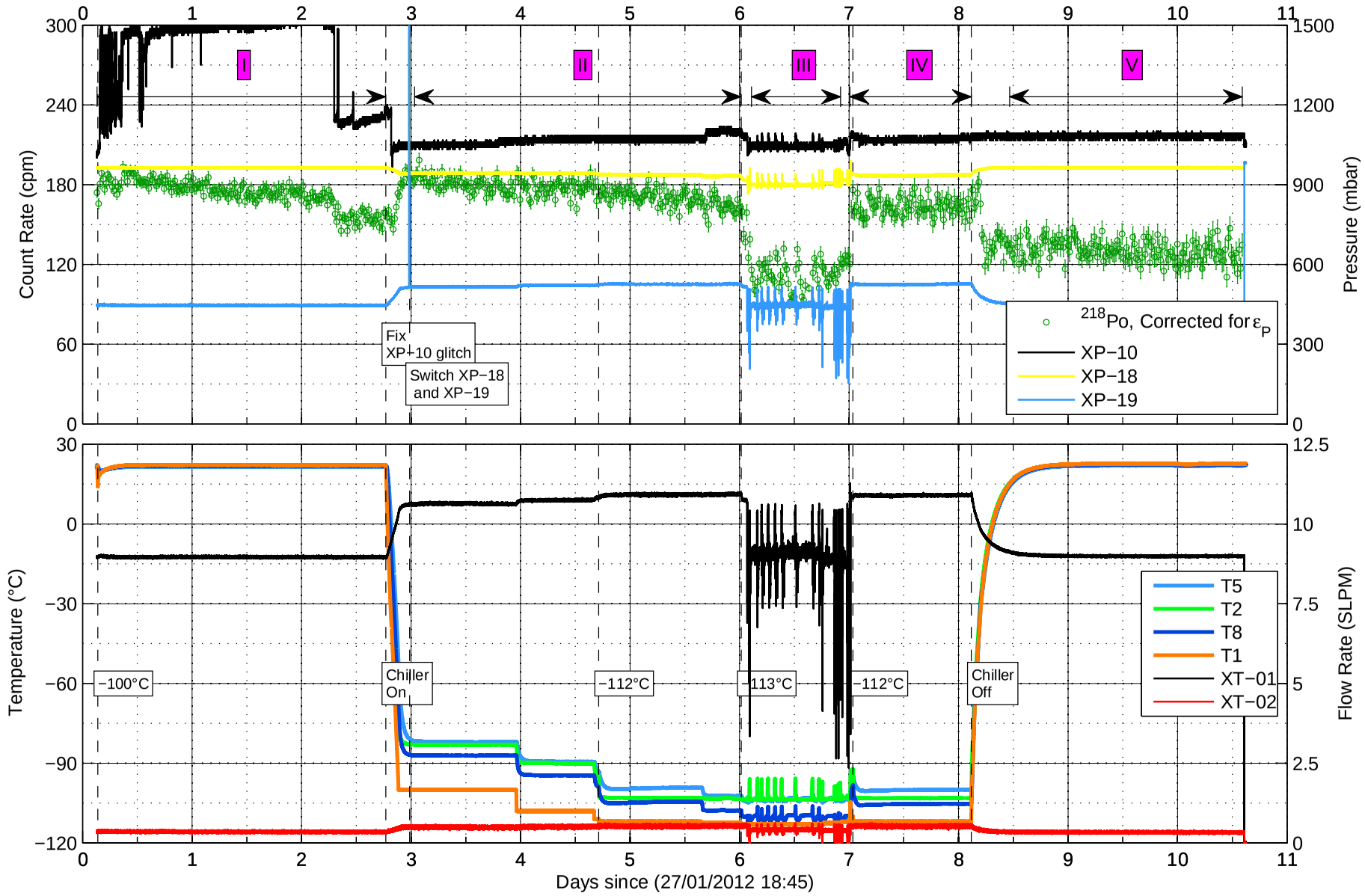

Figure 7.11: Run VII - Reduced Cu wool trap

Region	Setpoint (°C)	ESC Pressure (mbar)	ESC Flow (SLPM)	Count Rate (cpm)	Comments
I	N/A	N/A	0.349	172.9 ± 0.3	2nd order effects
II	$-100 \rightarrow -112.5$	1070	0.514	175.0 ± 0.4	2nd order effects
III	-113	1050	0.411	111.7 ± 0.7	Condensed Xe
IV	-112	1070	0.525	162.7 ± 0.8	System stable
V	N/A	1080	0.331	130.4 ± 0.6	Warm-up, end run
19.9 ± 0.7 % removal (Region IV $\rightarrow$ V)					

Table 7.4: Run VII Results

Stable count rates were counted by Region IV, after completely re-evaporating the Xe from the trap and cooling to $-112\,°C$. An unexpected result is observed, similar to RnRun CuWool VI, where a drop in Rn is seen by as much as 19.9 ± 0.7 % from Region IV to V. This does not hint at Rn removal from the trap, because adsorption enthalpy should only improve with decrease in temperature. There are two main interpretations from this run. First, the trap reduction attempt was not a success, possibly because of a leak at some point during installation causing the Cu to oxidise again. Second, the loss in count rate from Region IV to V cannot be justified by Rn removal. Perhaps there is something else at play here, such as impurities in the gas. In this case, the improved count rates in lower temperature regimes could be explained because of the impurities getting removed by the trap as temperature decreases. This scenario would suggest that either the purifier is not working effectively, or there is a leak in the system, or both. We would have to verify this hypothesis.

7.6 Decoupling Recirculation from Counting Efficiency (Run VIII)

At this stage, the cause of the faster-than-Rn decay was not clear, and this needed to be resolved before being able to properly test for Rn removal. The purpose of "RnRun CuWool VIII" is to test if the act of recirculating the gas has an effect on the counting efficiency of the ESC. The plan is to start with an injection of Rn in Xe as usual. The gas is then to be mixed and purified, and recirculation to be stopped for the first baseline.

The trap used in this run is still the same one in place from the previous run, reduced Cu wool, although we suspect the wool to be oxidized either from installation prior to the previous run, or from impurities in the gas. Data for RnRun CuWool VIII was collected from February 14 to March 1st, 2012. Actions performed during this run are listed in Appendix F.5. In short, the run consisted of the following:

- Start data acquisition on DAQ and LabView PCs.
- Mix Rn injection into 1000 mbar of Xe.
- Purify gas for 20 mins.
- Stop recirculation and count first baseline, Region I.
- Start recirculation and count Region II.
- Cool to $-100\,^{\circ}$C and count Region III.
- Stop cooling and count Region IV.
- Stop recirculation and count final baseline, Region V.

The results from this run are shown in Figure 7.12 and in Table 7.5. First, notice that there is still an apparent faster-than-Rn decays throughout the run; a difference of $\sim$4 cpm per day that cannot be accounted simply from exponential decay of ^{222}Rn. Recall that

Region	Setpoint (°C)	ESC Pressure (mbar)	ESC Flow (SLPM)	Count Rate (cpm)	Comments
I	N/A	1040	0	187.7 ± 0.3	No recirculation
II	N/A	1070	0.341	133.7 ± 0.3	Recirculation
III	-100	1060	0.477	167.7 ± 0.5	Cool to $-100\,^{\circ}$C
IV	N/A	1080	0.348	121.6 ± 0.4	Warm up
V	N/A	1030	0	135.8 ± 0.8	No recirculation

Table 7.5: Run VIII Results

corrections for Rn decay are already applied to these count rates. These 2$^{\text{nd}}$ order effects are persistent throughout the run.

Second, starting and stopping recirculation has a clear effect on counting efficiency. The transition from Region I to II causes a 28.7 ± 0.3 % drop in ^{218}Po simply from the act of starting recirculation. Turbulent flow was avoided as much as possible by restricting flow through the ESC to 0.341 SLPM. One idea could be that impurities in the system are affecting the drift of ^{218}Po ions when flowing into the ESC. Polar molecule such as H_2O or NO_2 are known to neutralize $^{218}Po^+$ ions [69], which would make them undetectable by the ESC. The act of starting recirculation could justify this loss in counting efficiency by allowing impurities to mix and bind with the ^{218}Po ions.

Third, the effect of cooling the trap to $-100\,^{\circ}$C seems to increase count rates by as much as 25.4 ± 0.6 % (from Region II to III) with an almost equal and opposite reaction after warming the trap up again. If the idea of impurities in the gas is correct, then cooling the trap could be removing these impurities due to their freezing points being above $-100\,^{\circ}$C. If this is true, the Rn trap has essentially become a cold trap for impurities in the gas.

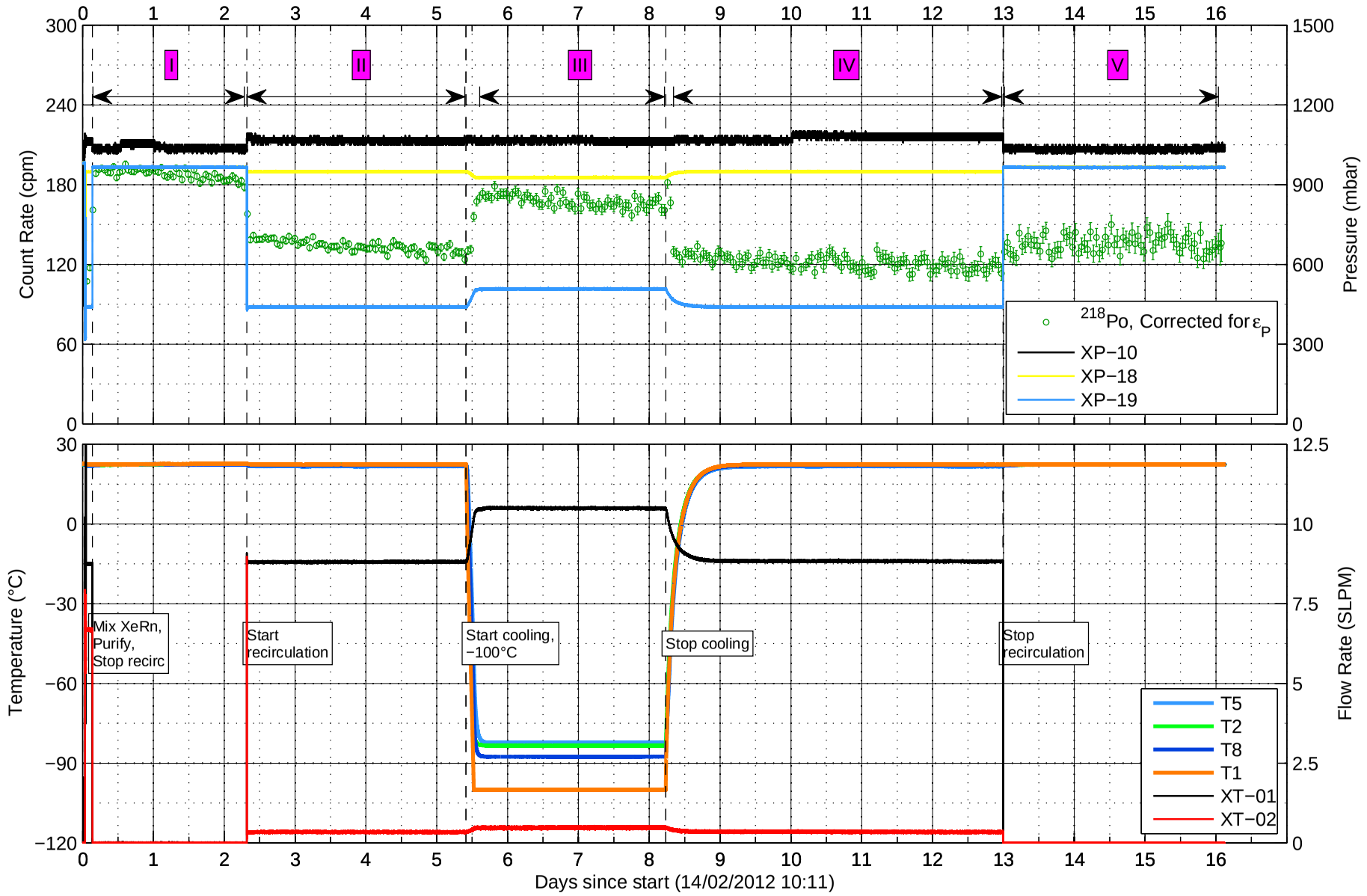

Figure 7.12: Run VIII - Decoupling $\epsilon_{\text{counting}}$ from recirculation

7.7 Decoupling Recirculation at Lower Pressure (Run IX)

"RnRun CuWool IX" was a run devised to help understand the aforementioned faster-than-Rn decay, while also attempting Rn removal at a lower pressure of 100 mbar of XeRn gas. The run plan is similar to the previous run, with the main exception that the test is performed at 100 mbar of gas, and the trap is isolated after the cooling period as an effort to keep any trapped contaminants inside a dead leg while the remainder of the gas is counted. Performed actions are detailed in Appendix F.6. The summary of actions is listed here:

- Inject Rn and mix with 100 mbar of Xe.
- Start data acquisition on DAQ and LabView PCs.
- Purify gas for 1 h 16 mins.
- Stop recirculation and count first baseline, Region I.
- Start recirculation and count Region II.
- Open flow through trap and throttle ESC inlet (regulating flow into ESC). Count Region III.
- Cool to $-100\,^{\circ}\mathrm{C}$ and count Region IV.
- Isolate trop and stop cooling. Count Region V.
- Stop recirculation and count final baseline, Region VI.

It became apparent during the course of this run that the XeRn system may not be used to run experiments at low pressures. To be specific, the thermodynamic system (cross-over heat exchanger, cold head, etc.) was designed to cool Xe at 1 atm, not necessarily for pressures close to 100 mbar. We can see this in the RTDs in Figure 7.13. Notice how the trap RTDs take upwards of one day to equilibrate after the refrigerator is turned on. T5 is

Region	Setpoint (°C)	ESC Pressure (mbar)	ESC Flow (SLPM)	Count Rate (cpm)	Comments
I	N/A	109	0	195.4 ± 0.3	No recirculation
II	N/A	111	0.037	181.1 ± 0.4	Recirculation
III	N/A	112	0.060	174.4 ± 0.5	Flow through trap
IV	−100	112	0.093	199.8 ± 0.5	Cool to −100 °C
V	N/A	111	0.658	193.8 ± 0.6	Warm up, Trap isolated
VI	N/A	110	0	192.5 ± 0.7	No recirculation

Table 7.6: Run IX Results

the slowest to plateau since it is the furthest RTD downstream of the trap. This gives an idea how long it takes for 100 mbar of gas to transport heat from the Cu spool to the rest of the plumbing in the vacuum enclosure.

There were also difficulties controlling the heater during this run. This is partly due to the PID settings. For this reason, the desired PID values were set as default into the LabView program for future runs.

Looking at the ^{218}Po count rates from Figure 7.13 and Table 7.6, we make a few familiar observations. First, we see faster-than-Rn decay again during periods of recirculation (Analysis Regions II, III, and IV). Region V is unique in that we are recirculating, yet count rates are steady, if not slightly on the *rise* during the interval. This supports the idea discussed in Section 5.2.3 that impurities in the gas could be causing faster-than-Rn decay, and the trap is acting as a purifier during Region III. Isolating the trap would have then caused these impurities to remain inside the trap while the rest of the gas is counted.

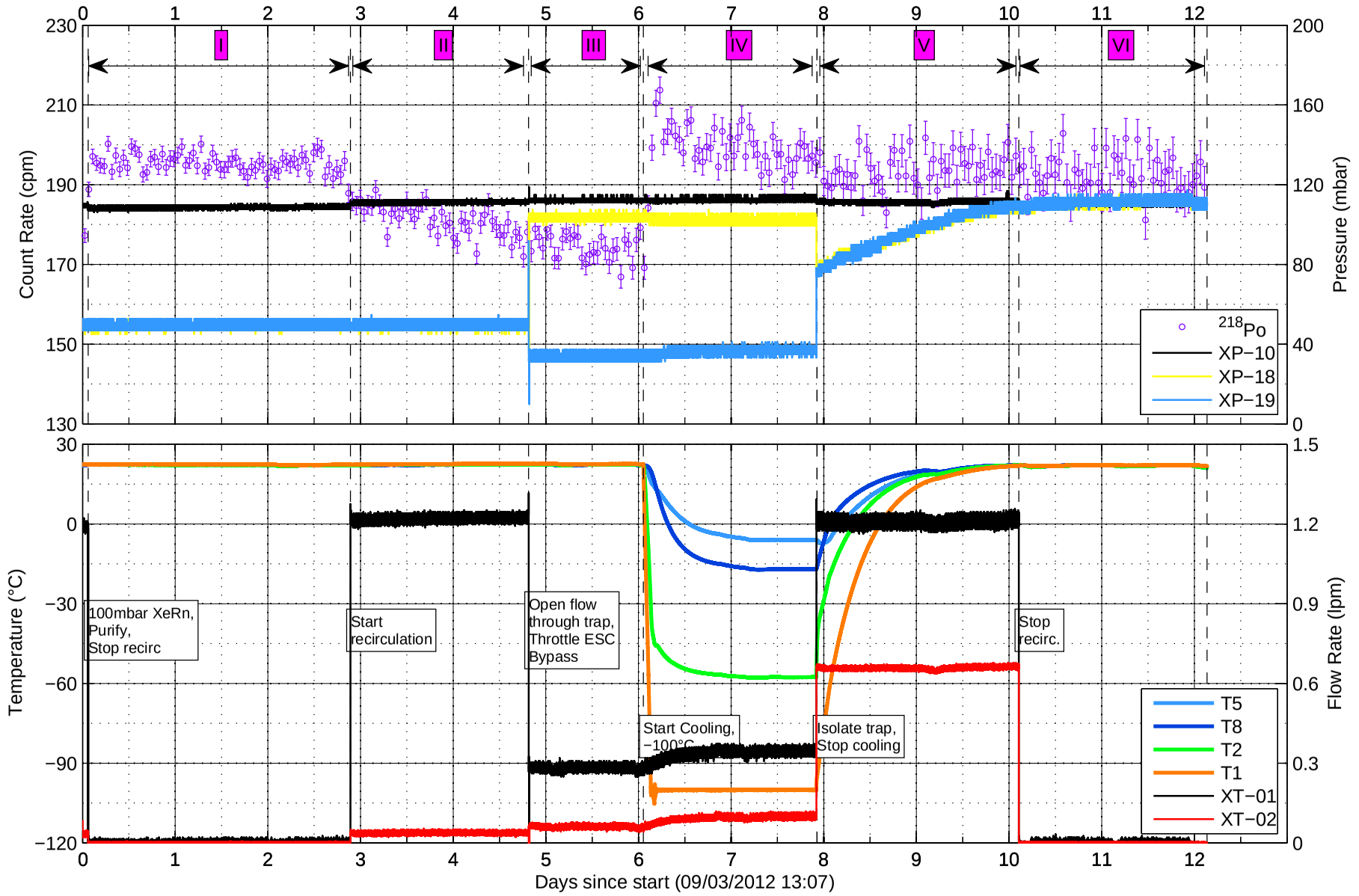

Figure 7.13: Run IX - Recirculation off for lower pressure

Average count rates were measured for the Regions of interest (Table 7.6). Note that Regions II, III, and IV are moving averages, and are not reliable as steady Rn activities. We see a slight 0.8 ± 0.4 % decrease in count rate from Regions I to V, and 1.5 ± 0.5 % decrease from Regions I to VI. Region I is considered as our first baseline to gauge our initial levels of Rn, and Region VI restores the same initial conditions to see if Rn was removed. Region V suggests that by isolating the Rn trap after a cooling period, we can trap impurities inside the trap, and recover the ESC's counting efficiencies.

7.8 Stopping Recirculation During Relevant Counting Regions (Run X)

By now faster-than-Rn decay is anticipated and we seek to mitigate its effects. In order to have analysable count rates, we now require recirculation to be stopped. The trap is also isolated when stopping recirculation in an attempt to keep any trapped substances inside that section of plumbing. It was on this basis that "RnRun CuWool X" was set up. The run went for a total of 19 days, beginning on March 28. Full run actions are provided in Appendix F.7. In short, the following actions were performed:

- Inject Rn and return Xe pressure to ∼165 mbar. Mix XeRn.
- Start data acquisition on DAQ and LabView PCs.
- Purify gas.
- Stop recirculation to count first baseline.
- Some difficulties with the heater when trying to cool to $-120\,^{\circ}\mathrm{C}$.
- Fill system to 1000 mbar of Xe, and respike with Rn (this procedure is defined in Appendix E).

- Purify gas again.
- Stop recirculation and count Region I (procedure also defined in Appendix E).
- Start cooling and recirculating through trap at $-109\,^{\circ}\mathrm{C}$.
- Isolate trap and start counting interval for Region II.
- Start cooling and recirculating through trap at $-60\,^{\circ}\mathrm{C}$.
- Isolate trap and start counting interval for Region III.
- Recirculate through trap for 1 day, before stopping and counting Region IV.

RnRun CuWool X was not without its fair share of obstacles. First, a heater failed during the cooling period on March 29, confirming that the current system is simply too unstable to run close to condensation point at low pressures. For the condensation point of Xe at $\sim$200 mbar approaching $-130\,^{\circ}\mathrm{C}$, the refrigerator cold head is approaching its peak in efficiency ($\sim$33 W cooling capacity quoted from [65]). The heater is being overpowered. One solution would be to install a Thermocoax wire heater element, which can withstand up to $1000\,^{\circ}\mathrm{C}$ without degrading, can easily provide the power we need, and can be brazed for better thermal contact and improved power. For example, the SEI 10/25 model will power a range of 25 to 100 W, given proper thermal contact [75]. The idea was contemplated, but installing the Thermocoax would also require a redesign of the Cu spool and substantial downtime.

For now, we are using an Omega® KHLV-105/10 flexible heater. With this heater, we must avoid exceeding 29 V AC on the VariAC, which was the safest voltage setting seen before the heater fried. We also discovered that the VariAC output voltage will vary depending on which power bar it is plugged into. This explains the 1-2 V discrepancy which might have led to the Xe plug forming on April 4 (during day 6).

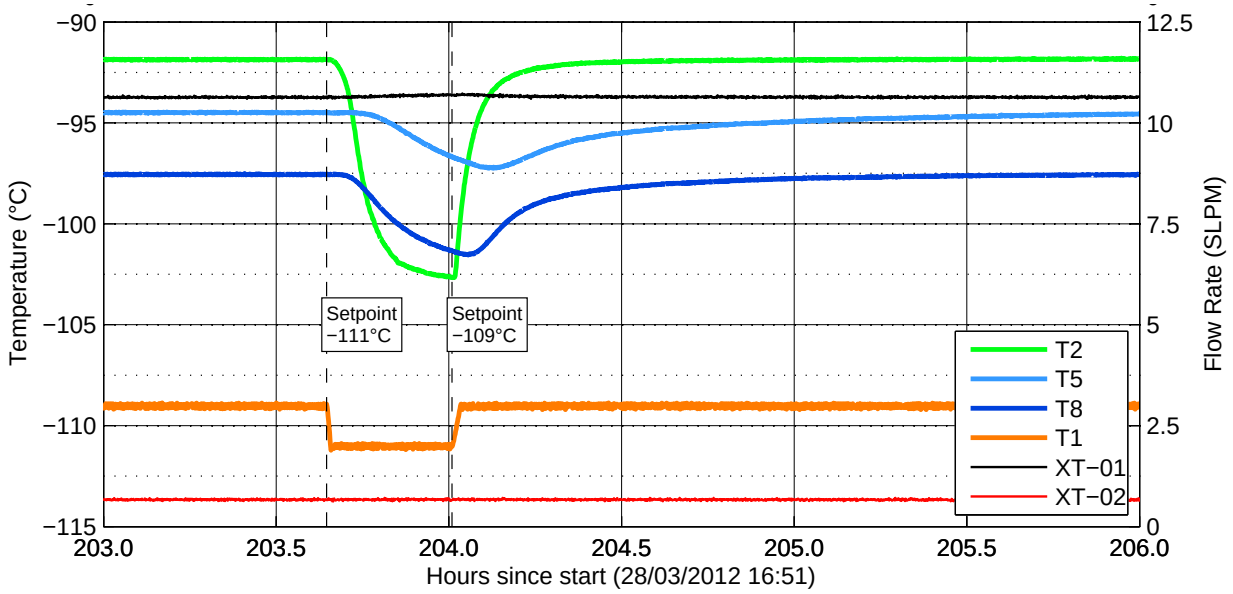

Figure 7.14: Condensation of Xe close to 204 hours after start of run. Notice the 11 °C drop in T2 after a meager 2 °C change in setpoint, and the inflection point on its way down.

Following the difficulties testing at 200 mbar, the run was re-purposed to return XeRn to 1000 mbar, and attempt trapping impurities such as H_2O or NO_2. The data for the first few days of the run at 200 mbar are not useful for this analysis, since there was only one count rate measured (nothing to compare to), and more Rn was added when pressurizing to 1000 mbar. Figure 7.15 only shows data for the 1000 mbar part of the run.

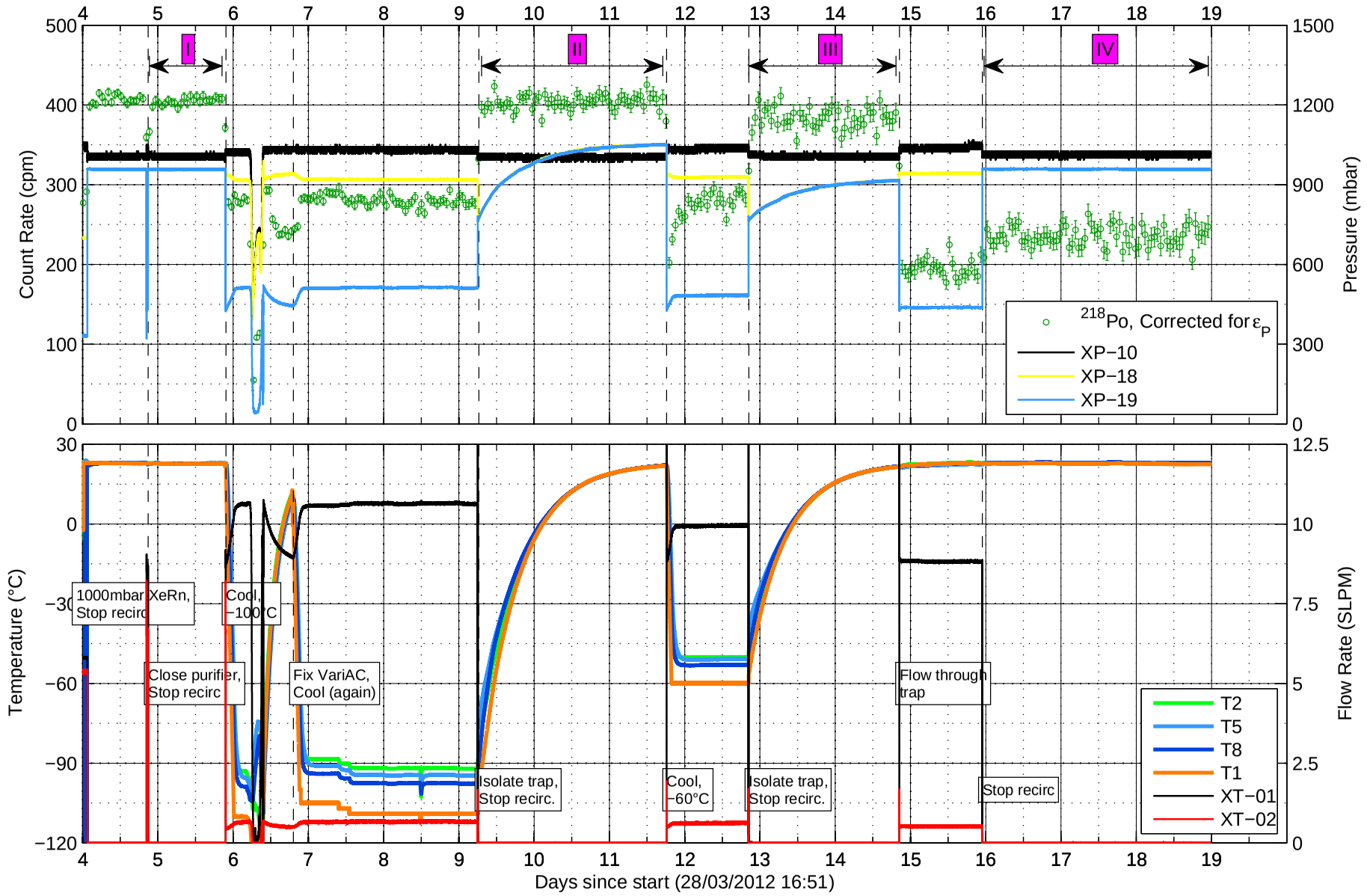

Figure 7.15: Run X - No recirculation during analysis regions

Region	Previous Setpoint (°C)	ESC Pressure (mbar)	Count Rate (cpm)	Difference from Region I (%)
I	N/A	1010	405 ± 1	
II	-109	1000	404 ± 1	-0.2 ± 0.5
III	-60	1010	383 ± 2	-5.3 ± 0.6
IV	N/A	1010	235 ± 1	-41.9 ± 0.5

Table 7.7: Results from RnRun CuWool X. "Previous Setpoint" refers to the setpoint of the cooling period immediately preceding the measured count rate. In all regions, flow is presumed to be 0 SLPM since recirculation has been stopped.

Since it was decided not to rely on count rates during periods of recirculation, analysis regions are now defined as the counting intervals *following* the desired changes made to the system. If trapping was attempted, then isolate the Rn trap before an analysis interval to prevent trapped agents from repopulating the gas being counted. In Table 7.7, we see the measured count rates corresponding to the analysis regions in Figure 7.15.

We see no significant loss in count rate from Regions I to II, 0.2 ± 0.5 %. Region III shows a decrease of 5.3 ± 0.6 % from Region I, and Region IV has a large departure of 41.9 ± 0.5 %. The explanation for this goes as follows: Region II preserved the purity of the gas by trapping impurities in the Rn trap during the recirculation period preceding it, when setpoints ranged from $-100\,^{\circ}\mathrm{C}$ to $-109\,^{\circ}\mathrm{C}$ (on the cusp of Xe condensation). We see the release of some contaminants before Region III while recirculating through the trap at $-60\,^{\circ}\mathrm{C}$, causing attachment of ^{218}Po ions before they can be detected by the ESC, and a slight decrease in counting efficiency as a result. Region IV follows a period of recirculation through the trap at room temperature, causign the ESC's counting efficiency to drop.

7.9 Cooling at Low Pressure (Run XI)

"RnRun CuWool XI" was shortened in scope due to a planned power outage at the SNOLAB surface labs. However, we had four days available for a data run, from April 16 to 20, which made it possible to attempt cooling at low pressures again, this time with the proper PID settings and with a more ideal voltage setting on the VariAC.

New procedures were formalized as a result of the previous RnRun. The procedures are defined in Appendix E. Detailed actions during RnRun CuWool XI are provided in Appendix F.8. A summary of actions goes as follows:

- Inject Rn and return Xe pressure to ∼130 mbar. Mix XeRn gas.
- Start data acquisition on DAQ and LabView PCs.
- Purify gas for 45 mins.
- Stop recirculation to count Region I.
- Start cooling and recirculating through trap.
- Attempt cooling to −120 °C but heating/cooling system unstable.
- Settle on −110 °C.
- Isolate trap and stop recirculation in order to count Region II.

From the events of April 17, it seemed clear after this run that we cannot test the system for Rn removal at low pressures. We attempted to bring the system close to condensation point with the proper PID and VariAC settings, but the system is not able to maintain −120, or even −110 °C for these low pressures. The coldest the system could be held with some stability was at −100 °C. Even at that, the plumbing in the vacuum enclosure would have taken days to stabilize, and it's questionable whether the trap would have cooled uniformly, as can be seen from the RTDs in Figure 7.16.

That said, there was little expectation of witnessing Rn removal in this run. The results of the counting intervals measured before and after the main period of recirculation is shown in Table 7.8. The main finding is that there is a slight removal of 1.2 ± 0.4 % after cooling to $-100\,^{\circ}\mathrm{C}$ (or at least cooling the Cu spool).

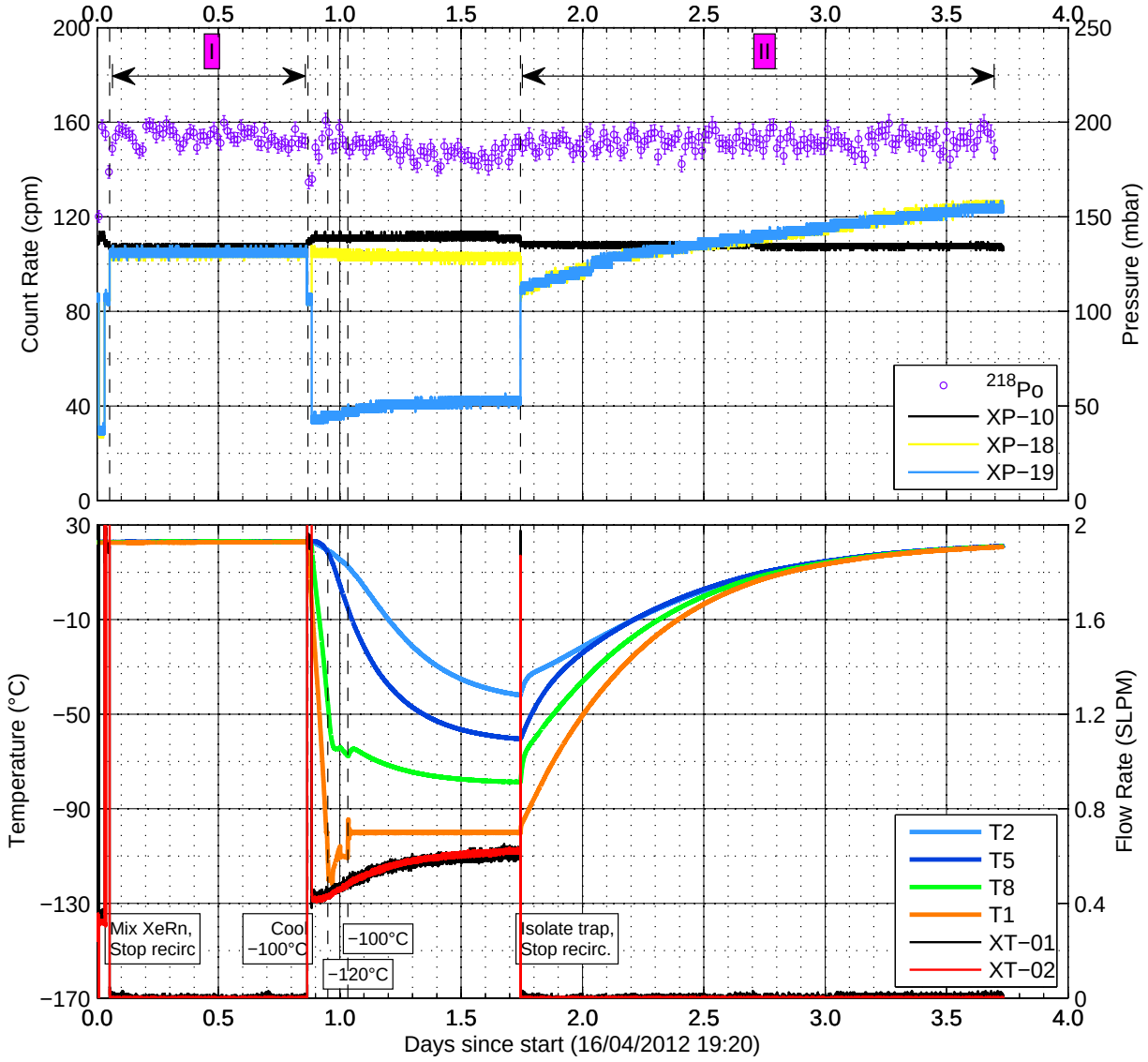

Figure 7.16: RnRun CuWool XI - Cooling at low pressure

Region	Previous Setpoint (°C)	ESC Pressure (mbar)	Count Rate (cpm)	Difference from Region I (%)
I	N/A	134	153.9 ± 0.4	
II	-100	135	151.9 ± 0.3	-1.2 ± 0.4

Table 7.8: Run XI Results

7.10 Temperature Scan (Run XII)

Based on previous results, we have a new strategy for counting ^{218}Po ions. We know we should only attempt cooling at pressures close to 1 atm, and to obtain a steady count rate for any analysis region, recirculation must be stopped. The purpose of "RnRun CuWool XII" is to characterize the counting efficiency of the ESC as a function of temperature, and possibly identify which impurities we have in the gas. The relative loss in counting efficiency could act as an indicator of what impurities are in the gas, depending on the previous temperature used in the cooling period. The run went from April 23 to May 20. The procedures defined in Appendix E are put to use multiple times here. For full run details, see Appendix F.8. In summary:

- Inject Rn and return Xe close to ∼1000 mbar. Mix XeRn gas.
- Start data acquisition on DAQ and LabView PCs.
- Purify gas.
- Stop recirculation to count Region I.
- Start cooling and recirculating through trap at $-70\,^{\circ}$C.
- Attempt cooling to $-120\,^{\circ}$C but heating/cooling system unstable.
- Isolate trap and stop recirculation in order to count Region II.
- Repeat the previous two steps for temperatures ranging from -60 to $-10\,^{\circ}$C in $10\,^{\circ}$C

increments

- Flow through trap at room temperature before isolating trap again and counting the final baseline, Region IX.

The operation of the XeRn system was fairly smooth for this run. We observed the same level of control over the heating/cooling system that we have seen in previous runs at atmospheric pressures. The first observation to make from Figure 7.17 and Table 7.9 is that count rates improve significantly when flowing the gas through the trap at low temperatures. In particular, the $-60\,^{\circ}\mathrm{C}$ and $-70\,^{\circ}\mathrm{C}$ setpoints (Regions II and III) show improvements compared to the initial count rate of XeRn gas mixed at room temperature. This clearly does not suggest any Rn removal. Rather, it supports our previous suspicion of contaminants in the gas affecting the ESC's counting efficiency.

Second, flowing the gas through the trap at $-50\,^{\circ}\mathrm{C}$ (Region IV) restores count rates to our baseline value (Region I), suggesting that our trapped contaminants might have been released again. However, the results from the analysis regions that followed (V through IX) were not expected. They show a progressively worse ^{218}Po count rate with each increase in setpoint. We restored the same initial conditions in Region IX as in Region I, yet we see a 25.7 ± 1.1 % reduction in ^{218}Po. The earlier claim that the contaminants were re-released from the trap by Region IV is now uncertain. It is still the possibility, but another interpretation could be the steady ingress of impurities from elsewhere in the XeRn system, such as from a leak in the plumbing.

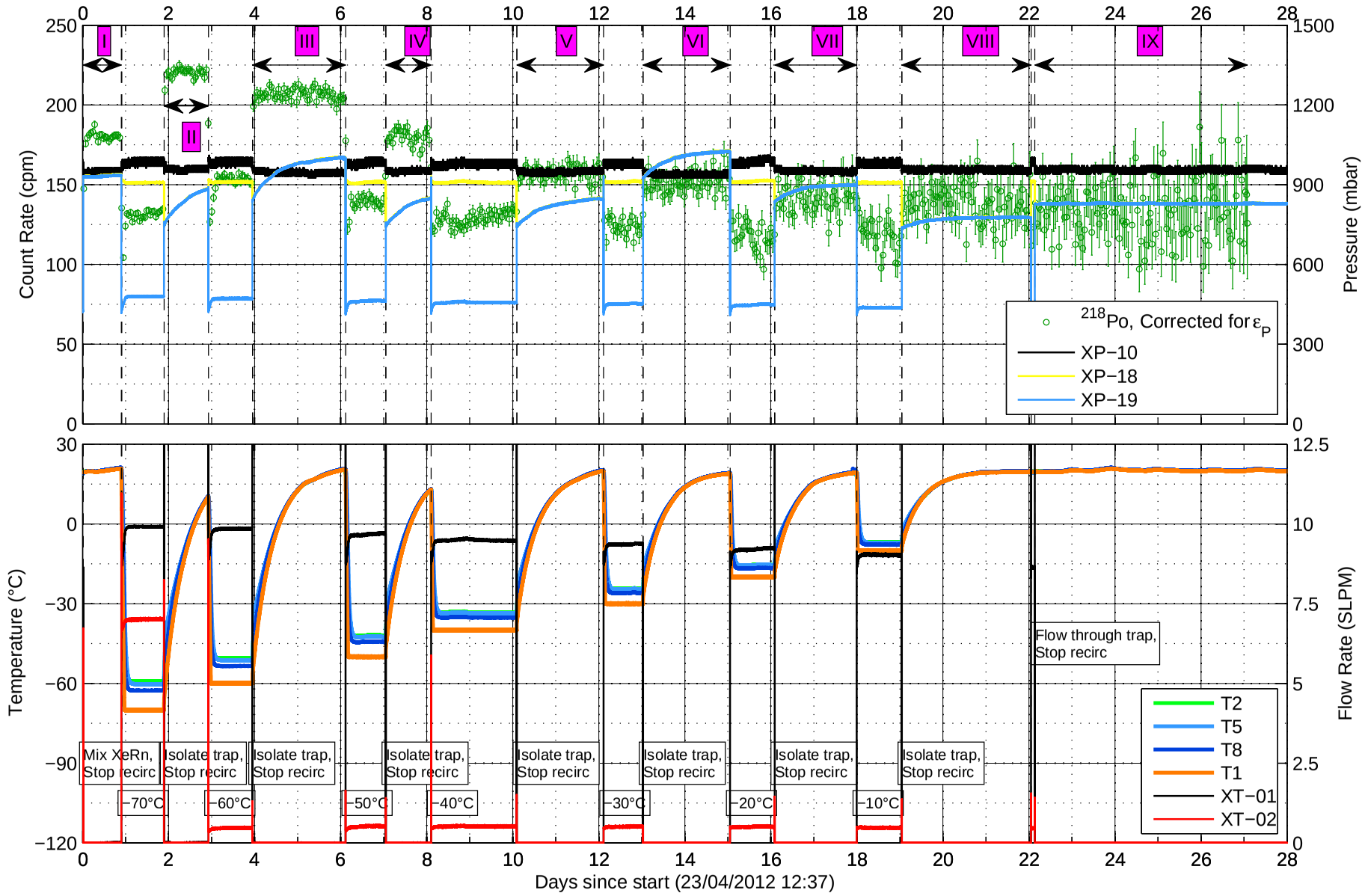

Figure 7.17: Run XII - Temperature scan

Region	Previous Setpoint (°C)	ESC Pressure (mbar)	Count Rate (cpm)	Difference from Region I (%)
I	N/A	950	179.9 ± 0.5	
II	-70	960	220.2 ± 0.6	$+22.4 \pm 0.6$
III	-60	950	206.6 ± 0.5	$+14.8 \pm 0.6$
IV	-50	950	179.6 ± 0.8	-0.2 ± 0.7
V	-40	950	156.7 ± 0.8	-12.9 ± 0.7
VI	-30	940	151.3 ± 1.0	-15.9 ± 0.8
VII	-20	950	141.7 ± 1.3	-21.3 ± 0.9
VIII	-10	960	138.1 ± 1.4	-23.3 ± 1.0
IX	N/A	960	133.6 ± 1.6	-25.7 ± 1.1

Table 7.9: Run XII Results

The fact that we could not restore our initial baseline from Region I to IX makes it difficult to identify the composition of the impurities in the gas at this point. The best approach would be to sample the gas with a residual gas analyser (RGA). Knowing the nature of the contaminants would be useful to know which approach to take to purifying the gas.

The current purifier on the system might have been exhausted. Perhaps the current purifier is also not sufficient for our purposes. We can try to answer these questions in the next run.

7.11 Purifier Test (Run XIII)

While we were in the process of procuring and installing an RGA to identify the impurities in the gas, a run was set up to test the effectiveness of the NuPure purifier on the XeRn system. Up until now, every RnRun has used the purifier solely during the gas mixing phase

before counting the first baseline, since the purifier is a known source of ^{222}Rn. What we would like to see here is first, if we can reproduce previous results of improved counting efficiencies at lower temperatures, and second, if count rates are affected at all by simply flowing through the purifier. "RnRun CuWool XIII" lasted twelve days from May 30 to June 11. See Appendix F.10 for full run details. In short, the run went as follows:

- Start LabView data acquisition.
- Inject Rn and return Xe close to ∼1000 mbar. Mix XeRn gas.
- Purify gas for 32 mins.
- Start ESC data acquisition.
- Stop recirculation to count Region I.
- Start cooling and recirculating through trap at −100 °C.
- Isolate trap and stop recirculation to count Region II.
- Flow through trap at room temperature for 41 mins, isolate trap, and stop recirculation. Count Region III.
- Flow through purifier for 37 mins, isolate, stop recirculation, and count Region IV.
- Start cooling and recirculating through trap at −100 °C.
- Isolate trap and stop recirculation to count Region V (same pre-conditions as Region II).

The results from this run are shown in Figure 7.18 and Table 7.10. It is good to see that our count rates are reproducible with similar system parameters. Both cooling regions (II and V) agree with each other, and room temperature analysis regions are also similar with each other (I, III, and IV).

We were able to reproduce our previous result of a sharp improvement in counting efficiency when cooling the trap to −100 °C. Region II shows a drastic 40.2±0.6 % improvement

Region	Previous Action	ESC Flow (SLPM)	ESC Pressure (mbar)	Count Rate (cpm)
I	Mix XeRn, purifying	0	960	170.1 ± 0.5
II	Cooling to $-100\,^{\circ}\mathrm{C}$	0	1000	238.5 ± 0.4
III	Flowing through trap	0	1000	157.3 ± 0.6
IV	Flowing through purifier	0	1000	176.4 ± 0.6
V	Cooling to $-100\,^{\circ}\mathrm{C}$	0	990	253.3 ± 0.8

Table 7.10: Results from RnRun CuWool XIII - "Previous Action" refers to the action immediately preceding the given analysis region before recirculation had to be turned off.

in count rate. Flowing through the trap and the purifier (Regions III and IV, respectively) once again shows the contaminants being re-released from the trap and returning counting rates to levels similar to Region I.

There is also a noticeable 12.2 ± 0.8 % improvement after flowing through the purifier, suggesting that the purifier does still have an effect on purity.

Cooling to $-100\,^{\circ}\mathrm{C}$ a second time (Region V) shows a dramatic improvement in the count rate, with a difference of 43.6 ± 0.9 % from Region IV. This along with the last few RnRuns in consideration, tells us that the purifier is having some marginal effect on the purity of the gas, but it is largely ineffective at removing contaminants. It is likely that the purifier is spent and needs to be regenerated, and that the XeRn system is saturated with contaminants, making it incapable of testing for Rn removal in its current state.

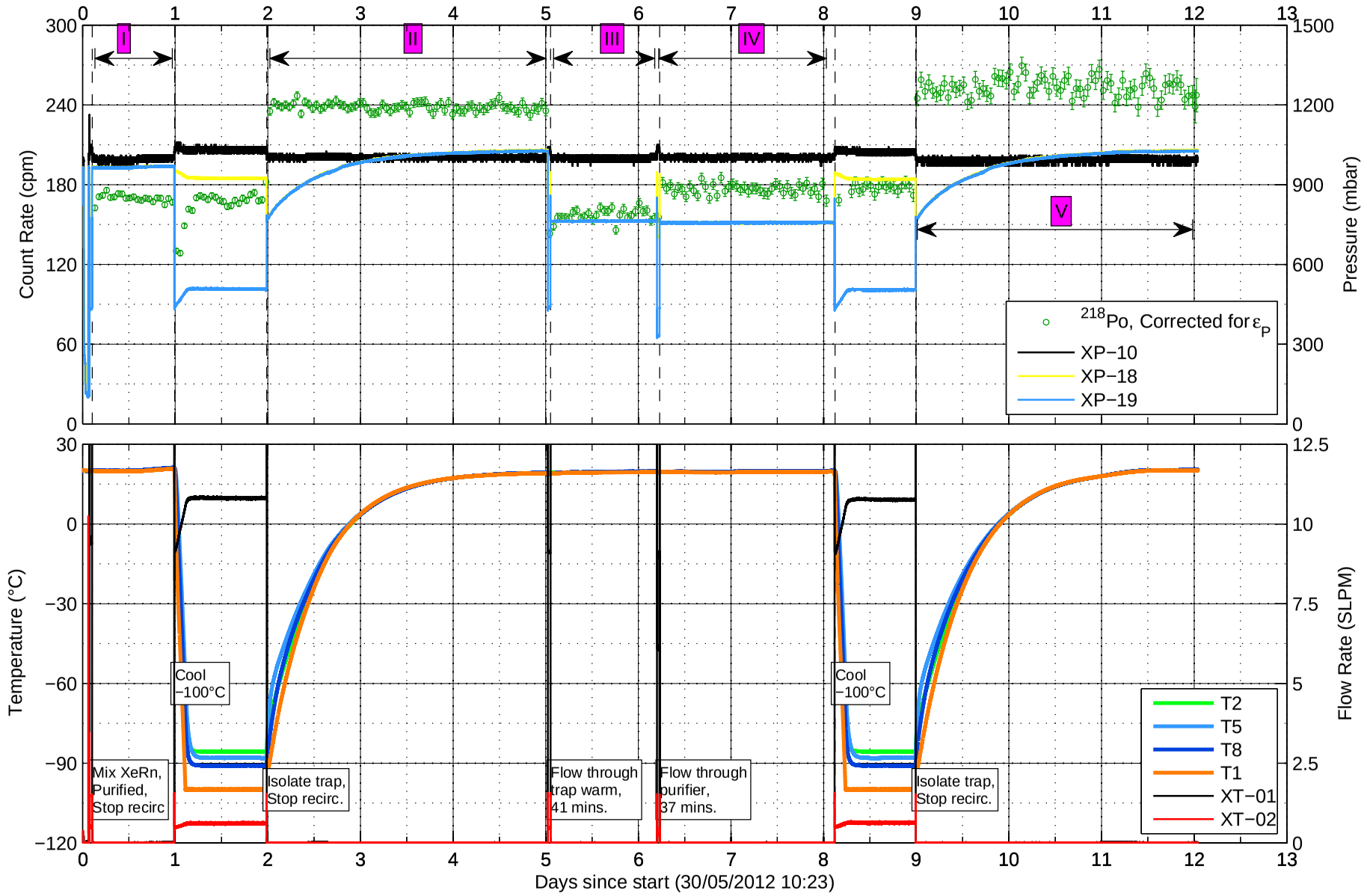

Figure 7.18: Run XIII - Purifier Test

Chapter 8

Conclusion

A summary of count rates from the RnRuns can be found in Table 8.1. A more thorough discussion on each data run is found in the previous chapter. We have observed Rn removal indicative of physical adsorption (up to 20 %) with the Cu wool trap, although the measurement was coupled with condensed gas, and the nominal count rate was not completely recovered (see Run V). The presence of contaminants in the gas (e.g. polar molecules such as H_2O and NO_2) are suspected to be affecting counting efficiencies by increasing the neutralization rate of Po in the ESC. New methods were developed to measure ^{218}Po count rates despite the presence of impurities, but these contaminants also affect trapping efficiency. Concentrations of impurities also change as we cool the trap, which makes decoupling the effect of impurities on count rates difficult.

RGA data could help us in developing a correction for counting efficiency as a function of impurity concentrations and knowing what contaminant to purify for. Purifying the gas would allow us to test a re-reduced Cu wool trap, or a trap containing Ni wool or activated charcoal. Purifying the gas either requires regenerating the NuPure purifier or purchasing and installing a new purifier, such as an Oxisorb® with a glass cartridge indicating the

state of the absorption material. The Oxisorb could also have the added benefit of *in situ* purification if it is demonstrated to be Rn-free.

A model of the electrostatic field in the ESC was made in MATLAB in order to help us understand the collection efficiencies of the ESC. Simulating the drift of $^{218}Po^{+}$ ions shows little difference in counting efficiency between using N_2 or Xe as a carrier gas.

[4]Beginning with run X, setpoint refers to the setpoint immediately *preceding* the region, before isolating the trap, stopping refrigeration and recirculation.

[5]Count rates are corrected for Rn decay, and corrected for pressure when ESC pressure is greater than 200 mbar (otherwise relative efficiency is at unity).

Run ID	Region	ESC Pressure (mbar)	Setpoint (°C)	Recirc? (Y/N)	Trap Open? (Y/N)	Count Rate[5] (cpm)	Comments	Conclusions
IV	I	1030	−100.0	Y	Y	216.6 ± 0.9		4.1 ± 2.9 % removal, likely due to condensation
	II	1030	−107.5	Y	Y	221.5 ± 1.9	Trap outlet throttled	
	III	950	−112.0	Y	Y	113.7 ± 3.5	ESC inlet throttled	
	IV	1030	−110.0	Y	Y	219.5 ± 2.0	ESC flow restored	
V	I	1030	−110.0	Y	Y	251.9 ± 0.9		19.5 ± 3.6 % Rn removal from adsorption. Need to reduce trap.
	II	1020	−112.0	Y	Y	224.8 ± 0.6	Trap outlet throttled	
	III	990	−113.0	Y	Y	173.4 ± 0.5		
	IV	1040	N/A	Y	Y	241.5 ± 6.4	Trap warming up	
VI	I	1070	−100.0	Y	Y	135.0 ± 0.5	First baseline	Need initial and final baselines to test Rn removal. Possible Rn outgassing in Region VI.
	II	1070	−100.0	Y	Y	130.6 ± 0.6	BL, after condensing	
	III	1070	−110.9	Y	Y	125.5 ± 0.6		
	IV	1060	−111.0	Y	Y	120.8 ± 0.7		
	V	1060	−111.1	Y	Y	120.8 ± 0.7		
	VI	1060	N/A	Y	Y	76.2 ± 0.7	Trap warming up	
VII	I	N/A	N/A	Y	Y	172.9 ± 0.3	2^{nd} order effects	Reduction does not show improvement. 2^{nd} order effects raise doubts on recirculation.
	II	1070	−112.5	Y	Y	175.0 ± 0.4	2^{nd} order effects	
	III	1050	−113.0	Y	Y	111.7 ± 0.7	Condensed Xe	
	IV	1070	−112.0	Y	Y	162.7 ± 0.8	System fairly stable	
	V	1080	N/A	Y	Y	130.4 ± 0.6	Warm up, end run	
VIII	I	1040	N/A	N	Y	187.7 ± 0.3	Recirculation OFF	2^{nd} order effects throughout run. Counting efficiency improved by cooling, but worsened by flow.
	II	1070	N/A	Y	Y	133.7 ± 0.3	Recirculation ON	
	III	1060	−100.0	Y	Y	167.7 ± 0.5	Cool to −100 °C	
	IV	1080	N/A	Y	Y	121.6 ± 0.4	Trap isolated	
	V	1030	N/A	N	Y	135.6 ± 0.8	Recirculation OFF	

Run ID	Region	ESC Pressure	Setpoint[4]	Recirc?	Trap Open?	Count Rate[5]	Comments	Conclusions
IX	I	109	N/A	N	N	195.4 ± 0.3	Recirculation OFF	System not ideal for low pressure. Trap removing contaminants from gas. New counting method established.
	II	111	N/A	Y	N	181.1 ± 0.4	Recirculation ON	
	III	112	N/A	Y	Y	174.4 ± 0.5	Flow through trap	
	IV	112	-100.0	Y	Y	199.8 ± 0.5	Cool to $-100\,^{\circ}\mathrm{C}$	
	V	111	N/A	Y	N	193.8 ± 0.6	Trap isolated	
	VI	110	N/A	N	N	192.5 ± 0.7	Recirculation OFF	
X	I	1010	N/A	N	N	404.9 ± 1.0	First baseline	New method works for counting ^{218}Po. Trap removing impurities.
	II	1000	-109.0	N	N	404.0 ± 1.1	-0.2 % difference	
	III	1010	-60.0	N	N	383.4 ± 1.6	-5.3 % difference	
	IV	1010	N/A	N	N	235.3 ± 1.4	-41.9 % difference	
XI	I	134	N/A	N	Y	153.9 ± 0.4	First baseline	System unstable cooling at low P.
	II	135	-100.0	N	N	151.9 ± 0.3	-1.2 % difference	
XII	I	950	N/A	N	Y	179.9 ± 0.5	First baseline	Counting efficiency improves when cooling trap (removing impurities from the gas). More contaminants released after IV. Suspect purifier is spent.
	II	960	-70.0	N	N	220.2 ± 0.6	+22.4 % difference	
	III	950	-60.0	N	N	206.6 ± 0.5	+14.8 % difference	
	IV	950	-50.0	N	N	179.6 ± 0.8	-0.2 % difference	
	V	950	-40.0	N	N	156.7 ± 0.8	-12.9 % difference	
	VI	940	-30.0	N	N	151.3 ± 1.0	-15.9 % difference	
	VII	950	-20.0	N	N	141.7 ± 1.3	-21.3 % difference	
	VIII	960	-10.0	N	N	138.1 ± 1.4	-23.3 % difference	
	IX	960	N/A	N	N	133.6 ± 1.6	-25.7 % difference	

Run ID	Region	ESC Pressure	Setpoint[4]	Recirc?	Trap Open?	Count Rate[5]	Comments	Conclusions
XIII	I	960	N/A	N	N	170.1 ± 0.5	After purifying	Purifier needs regeneration or upgrade. RGA would help identify impurities.
	II	1000	-100.0	N	N	238.5 ± 0.4		
	III	1000	N/A	N	N	157.3 ± 0.6	Flowed through trap	
	IV	1000	N/A	N	N	176.4 ± 0.6	After purifying	
	V	990	-100.0	N	N	253.3 ± 0.8		

Table 8.1: Summary of experimental results

Chapter 9

Bibliography

[1] EXO Collaboration, M. Auger et al. An improved measurement of the $2\nu\beta\beta$ half-life of Xe-136 with EXO-200. arXiv:1306.6106.

[2] Rabindra N. Mohapatra and Palash B. Pal. *Massive Neutrinos in Physics and Astrophysics*. World Scientific Publishing, 3rd edition, 2004.

[3] James Chadwick. Possible Existence of a Neutron. *Nature*, 129(3252):312–312, 1932.

[4] Michael F. L'Annunziata. *Radioactivity: Introduction and History*. Elsevier Science, 1st edition, 2007.

[5] Carlo Giunti and Chung W. Kim. *Fundamentals of Neutrino Physics and Astrophysics*. Oxford University Press, 2007.

[6] Kan Chang Wang. A Suggestion on the Detection of the Neutrino. *Physical Review*, 61(1-2):97–97, October 1941.

[7] C.L. Cowan et al. Detection of the Free Neutrino: a Confirmation. *Science*, 124(3212):103–104, July 1956.

[8] C.L. Cowan and F. Reines. The Neutrino. *Nature*, 178:446–449, September 1956.

[9] G. Danby et al. Observation of High-Energy Neutrino Reactions and the Existence of Two Kinds of Neutrinos. *Physical Review Letters*, 9(1):36–44, June 1962.

[10] DONuT Collaboration, K. Kodama et al. Observation of Tau Neutrino Interactions. *Physics Letters B*, 504(3):218–224, April 2001.

[11] DONuT Collaboration, K. Kodama et al. Final Tau-Neutrino Results from the DONuT Experiment. *Physical Review D*, 78(5), September 2008.

[12] Donald D. Clayton. *Principles of Stellar Evolution and Nucleosynthesis*. University of Chicago Press, 1983.

[13] John N. Bahcall and Aldo M. Serenelli. New Solar Opacities, Abundances, Helioseismology, and Neutrino Fluxes. *The Astrophysical Journal*, 621:L85–L88, 2005.

[14] R. Mitalas and K.R. Sills. On the Photon Diffusion Time Scale for the Sun. *The Astrophysical Journal*, 401(2):759–760, June 1992.

[15] Raymond Davis. The Search for Solar Neutrinos. *Annals of the New York Academy of Sciences*, 655:209234. doi:10.1111/j.1749-6632.1992.tb17073.x.

[16] SAGE Collaboration, J.N. Abdurashitov et al. Measurement of the Solar Neutrino Capture Rate with Gallium Metal. *Physical Review C*, 60:055801, October 1999.

[17] GALLEX Collaboration, W. Hampel et al. GALLEX Solar Neutrino Observations: Results for GALLEX IV. *Physics Letters B*, 447:127–133, February 1999.

[18] GNO Collaboration, M. Altmann et al. GNO solar neutrino observations: results for GNO I. *Physics Letters B*, 490(1-2):16–26, September 2000.

[19] Super-Kamiokande Collaboration, S. Fukuda et al. Solar ^{8}B and hep Neutrino Measurements from 1258 Days of Super-Kamiokande Data. *Physical Review Letters*, 86(25):5651–5655, June 2001.

[20] Super-Kamiokande Collaboration, Y. Fukuda et al. Evidence for Oscillation of Atmospheric Neutrinos. *Physical Review Letters*, 81(8):1562–1567, August 1998.

[21] SNO Collaboration, Q.R. Ahmad et al. Measurement of the Rate of $\nu_e + d \rightarrow p + p + e^-$ Interactions Produced by ^{8}B Solar Neutrinos at the Sudbury Neutrino Observatory. *Physical Review Letters*, 87(7):071301, August 2001.

[22] SNO Collaboration, Q.R. Ahmad et al. Direct Evidence for Neutrino Flavor Transformation from Neutral-Current Interactions in the Sudbury Neutrino Observatory. *Physical Review Letters*, 89(1):011301, June 2002.

[23] Bruno Pontecorvo. Mesonium and Anti-mesonium. *Soviet Journal of Experimental and Theoretical Physics*, 6:429, 1957.

[24] Bruno Pontecorvo. Neutrino Experiments and the Problem of Conservation of Leptonic Charge. *Soviet Journal of Experimental and Theoretical Physics*, 26:984, May 1968.

[25] V. Gribov and B. Pontecorvo. Neutrino astronomy and lepton charge. *Physics Letters B*, 28(7):493–496, January 1969.

[26] Z. Maki, M. Nakagawa, and S. Sakata. Remarks on the Unified Model of Elementary Particles. *Progress of Theoretical Physics*, 28(5):870–880, 1962.

[27] Daya-Bay Collaboration, Xinheng Guo et al. A precision measurement of the neutrino mixing angle θ_{13} using reactor antineutrinos at Daya-Bay. January 2007. Proposal to DoE. arXiv:hep-ex/0701029.

[28] V.N. Aseev et al. An Upper Limit on Electron Antineutrino Mass from Troitsk Experiment. *Physical Review D*, 84(112003), 2011.

[29] K. Eitel. Direct Neutrino Mass Experiments. *Nuclear Physics B - Proceedings Supplements*, 143:197–204, June 2005.

[30] Uroš Seljak, Anže Slosar, and Patrick McDonald. Cosmological Parameters from Combining the Lyman-α Forest with CMB, Galaxy Clustering and SN Constraints. *Journal of Cosmology and Astroparticle Physics*, 10, 2006.

[31] Øystein Elgarøy and Ofer Lahav. Neutrino Masses from Cosmological Probes. *New Journal of Physics*, 7(61), 2005. arXiv:hep-ph/0412075.

[32] R.D. McKeown and P. Vogel. Neutrino masses and oscillations: Triumphs and challenges. *Physics Reports*, 394:315–356, May 2004. arXiv:hep-ph/0402025.

[33] Steven R. Elliott and Petr Vogel. Double Beta Decay. *Annual Review of Nuclear and Particle Science*, 52:115–151, December 2002. arXiv:hep-ph/0202264.

[34] M. Redshaw et al. Mass and Double-Beta Decay Q-Value of ^{136}Xe. *Physical Review Letters*, 98(5):053003, 2007.

[35] Particle Data Group, J. Beringer et al. 2012 Review of Particle Physics. *Physical Review D*, 86(010001), 2012.

[36] S.M. Bilenky and Carlo Giunti. Neutrinoless double-beta decay. A brief review. Unpublished. arXiv:1203.5250.

[37] Heidelberg-Moscow Collaboration, H.V. Klapdor-Kleingrothaus et al. Latest Results from the Heidelberg-Moscow Double-Beta-Decay Experiment. *The European Physical Journal A*, 12(2):147–154, 2001.

[38] H.V. Klapdor-Kleingrothaus et al. Evidence for Neutrinoless Double Beta Decay. *Modern Physics Letters A*, 16(37):2409–2420, December 2001.

[39] C.E. Aalseth et al. Comment on "Evidence for Neutrinoless Double Beta Decay". *Modern Physics Letters A*, 17(22):1475–1478, July 2002.

[40] I.V. Kirpichnikov. Klapdor's Claim for the Observation of the Neutrinoless Double Beta-Decay of ^{76}Ge. Analysis and corrections. *preprint*, June 2010. arXiv:1006.2025.

[41] H.L. Harney. Reply to Comment on "Evidence for Neutrinoless Double Beta Decay. *Modern Physical Letters A*, 16:2409, May 2001.

[42] H.V. Klapdor-Kleingrothaus and I.V. Krivosheina. The Evidence for the Observation of $0\nu\beta\beta$ Decay: The Identification of $0\nu\beta\beta$ Events from the Full Spectra. *Modern Physics Letters A*, 21(20):1547–1566, March 2006.

[43] C. Dorr and H.V. Klapdor-Kleingrothaus. New Monte-Carlo simulation of the HEIDELBERG-MOSCOW double beta decay experiment. *Nuclear Instruments and Methods in Physics Research A*, 513:596–621, November 2003.

[44] GERDA Collaboration, M. Agostini et al. Results on neutrinoless double beta decay of ^{76}Ge from GERDA PHASE I. arXiv:1307.4720.

[45] EXO Collaboration, M. Auger et al. Search for Neutrinoless Double-Beta Decay in ^{136}Xe with EXO-200. *Physical Review Letters*, 109(3):032505, July 2012. arXiv:1205.5608.

[46] KamLAND-Zen Collaboration, A. Gando et al. Measurement of the Double-β decay half-life of ^{136}Xe with the KamLAND-Zen Experiment. *Physical Review C*, 85:045504, April 2012.

[47] E. Conti et al. Correlated fluctuations between luminescence and ionization in liquid xenon. *Physical Review B*, 68(5), August 2003.

[48] Heidelberg-Moscow Collaboration, A.M. Bakalyarov et al. Results of the Experiment on Investigation of Germanium-76 Double Beta Decay. Experiment Data of Heidelberg-Moscow Collaboration. November 1995 - August 2001.

[49] C. Arnaboldi et al. Results from a Search for the $0\nu\beta\beta$-decay of ^{130}Te. *Physical Review C*, (78):035502, 2008.

[50] R. Bernabei et al. Investigation of $\beta\beta$ Decay Modes in ^{134}Xe and ^{136}Xe. *Physics Letters B*, 546(1-2):23–28, October 2002.

[51] EXO Collaboration, M. Auger et al. Observation of Two-Neutrino Double-Beta Decay in ^{136}Xe with the EXO-200 Detector. *Physical Review Letters*, 107(21):212501, November 2011.

[52] R. Neilson et al. Characterization of large area APDs for the EXO-200 detector. *Nuclear Instruments and Methods in Physics Research A*, 608(1):68–75, September 2009. dx.doi.org/10.1016/j.nima.2009.06.029.

[53] 3M HFE-7000. `http://www.3m.com/`.

[54] EXO Collaboration, M. Auger et al. The EXO-200 detector, part I: Detector Design and Construction. *Journal of Instrumentation*, 7(P05010), May 2012. arXiv:1202.2192.

[55] D.S. Leonard et al. Systematic study of trace radioactive impurities in candidate construction materials for EXO-200. *Nuclear Instruments and Methods in Physics Research Section A*, 591(3), July 2008.

[56] Ashok K. Jain and Balraj Singh. Nuclear Data Sheets for A = 218. *Nuclear Data Sheets*, 107(4):1027–1074, April 2006.

[57] P Barbeau et al. Assessment of the Need for a Radon Trap in EXO-200. Internal Report for EXO, June 2012.

[58] The XMASS Collaboration, K. Abe et al. Radon Removal from Gaseous Xenon with Activated Charcoal. *Nuclear Instruments and Methods in Physics Research A*, 661:50–57, 2012.

[59] R. Eichler and M. Schadel. Adsorption of Radon on Metal Surfaces: A Model Study for Chemical Investigations of Elements 112 and 114. *Journal of Physical Chemistry B*, 106(21):5413–5420, April 2002.

[60] A. Staudt, K. Muto, and H.V. Klapdor-Kleingrothaus. Calculation of 2ν and 0ν Double-Beta Decay Rates. *Europhysics Letters*, 13(1):31–36, September 1990.

[61] Xin Yang. Highly Efficient Trace Radon Removal in High Pressure Xenon in the Search for Neutrinoless Double Beta Decay. B.Sc. Dissertation.

[62] Jian-Xiong Wang, Tom C. Andersen, and John J. Simpson. An Electrostatic Radon Detector Designed for Water Radioactivity Measurements. *Nuclear Instruments and Methods in Physics Research A*, 421:601–609, 1999.

[63] J. Farine and B. Aharmim. Radon emanation of NuPure's Eliminator-0600-CG Elog # 349, September 2005. `http://thoron.phys.laurentian.ca/~jfarine/exo/rep/eliminator.pdf`.

[64] Cross-over heat exchanger and trap enclosure drawings. `http://thoron.phys.laurentian.ca:8080/XeRn+INFO/11`.

[65] CryoTiger Brochure. http://thoron.phys.laurentian.ca:8080/XeRn+INFO/22.

[66] LabView Instructions. http://thoron.phys.laurentian.ca:8080/XeRn+INFO/30.

[67] Tom Andersen. *Development of Systems for the Sudbury Neutrino Observatory*. PhD thesis, University of Guelph, 1997.

[68] William H. Press et al. *Numerical Recipes in C: The Art of Scientific Computing*. Cambridge University Press, 1992.

[69] Kai-Dee Chu and Philip K. Hopke. Neutralization Kinetics for Polonium-218. *Environmental science & technology*, 22(6):711–717, 1988.

[70] *CRC Handbook of Chemistry and Physics*. CRC Press, 1978.

[71] A.J. Howard and W.P. Strange. Heavy-Ion Migration through Argon and Helium in Weak Electric Fields. *Journal of Applied Physics*, 69(9), 1991.

[72] G.A. Eiceman and Z. Karpas. *Ion Mobility Spectrometry*. CRC Press, 2nd edition.

[73] Sukhjeet Singh, A.K. Jain, and Jagdish K. Tuli. Nuclear Data Sheets for A = 222. *Nuclear Data Sheets*, 112(11):2851–2886, November 2011.

[74] *LabVIEW® PID and Fuzzy Logic Toolkit User Manual*. National Instruments, June 2009.

[75] Thermocoax. http://www.thermocoax.com/pdf/E013_10_HE_English.pdf.

Appendix A

XeRn System Flowsheet

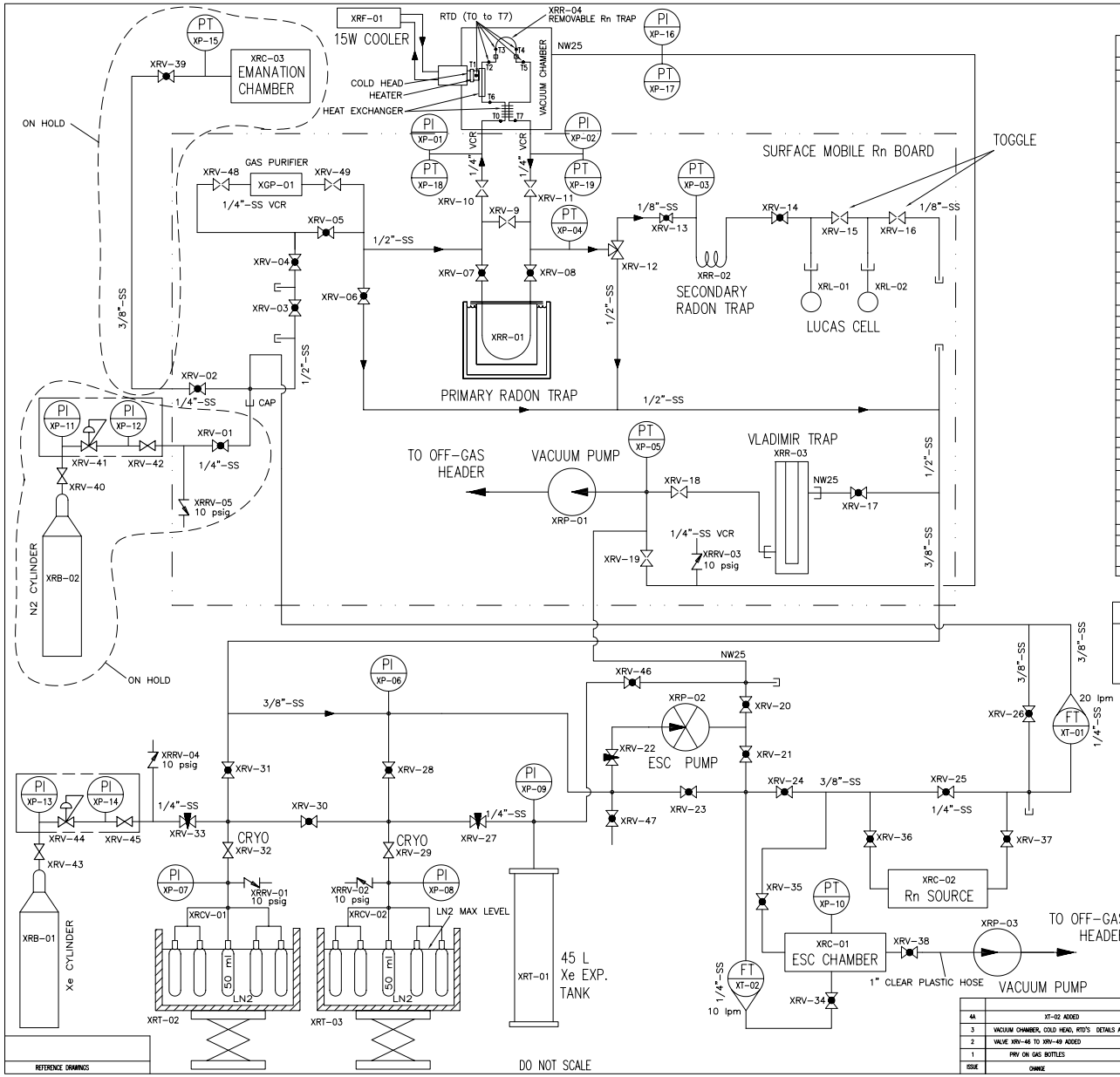

VALVE LIST

VALVE No.	P/N	DESCRIPTION
XRV-01	SWAGELOK p/n SS-1RS4	BALL, 1/4" SWG
XRV-02	SWAGELOK p/n SS-31RS4	BALL, 1/4" SWG
XRV-03 XRV-04 XRV-05 XRV-06 XRV-07 XRV-08	SWAGELOK p/n SS-45S8	BALL, 1/2" SWG
XRV-09 XRV-10 XRV-11	SWAGELOK p/n SS-4BK-V51	BELLOWS, 1/4" FVCR
XRV-12	SWAGELOK p/n SS-45XS8	BALL, 1/2" SWG
XRV-13 XRV-14	SWAGELOK p/n SS-41S2	BALL, 1/8" SWG
XRV-15 XRV-16	SWAGELOK p/n SS-0GS2	TOGGLE, 1/8" SWG
XRV-17	SWAGELOK p/n SS-63-TS8	BALL, 1/2" SWG
XRV-18 XRV-19	LESKER p/n SA0100MVQF	BELLOWS, FLUOROCARBON, QF25
XRV-20 XRV-21	SWAGELOK p/n SS-43GS6-1466	BALL, 3/8" SWG
XRV-22	SWAGELOK p/n SS-1RS4-AG-HL	NEEDLE, 1/4" SWG
XRV-23 XRV-24	SWAGELOK p/n SS-43GS6-1466	BALL, 3/8" SWG
XRV-25	SWAGELOK p/n SS-42S4	BALL, 1/4" SWG
XRV-26	SWAGELOK p/n SS-43GS6-1466	BALL, 3/8" SWG
XRV-27	SWAGELOK p/n SS-1RS4-AG-HL	NEEDLE, 1/4" SWG
XRV-28	SWAGELOK p/n SS-43GS6-1466	BALL, 3/8" SWG
XRV-29	SWAGELOK p/n SS-6UW	CRYO, 3/8" SWG
XRV-30	SWAGELOK p/n SS-44S6	BALL, 3/8" SWG
XRV-31	SWAGELOK p/n SS-43GS6-1466	BALL, 3/8" SWG
XRV-32	SWAGELOK p/n SS-6UW	CRYO, 3/8" SWG
XRV-33	SWAGELOK p/n SS-1RS4RG-NL	NEEDLE, 1/4" SWG
XRV-34 XRV-35	SWAGELOK p/n B-6P6T	BALL, 3/8" SWG
XRV-36 XRV-37	SWAGELOK p/n SS-4P4T	BALL, 1/4" SWG
XRV-38		
XRV-39	SWAGELOK p/n B-44S6	BALL, 3/8" SWG
XRV-40		COMES WITH BOTTLE
XRV-41 XRV-42		REGULATOR CGA 580 TO 1/4" SWG
XRV-43		COMES WITH BOTTLE
XRV-44 XRV-45		REGULATOR CGA 580 TO 1/4" SWG
XRV-46	SWAGELOK p/n SS-4558	BALL, 1/2" SWG
XRV-47		BALL, 3/8" SWG
XRV-48 XRV-49	SWAGELOK p/n SS-4BK-V51	BELLOWS, 1/4" FVCR

PUMP, FLOW METER LIST

PUMP No.	P/N	DESCRIPTION
XRP-01	ALCATEL, MODEL: 2010	NW25 PORTS
XRP-02	KNF, MODEL: UN035 TTR	DIAPHRAGM, 3/8" SWG PORTS
XRP-03	ALCATEL, MODEL: 2010	NW25 PORTS
XT-01	AALBORG, p/n GFM37	20 lpm XENON
XT-02	AALBORG, p/n GFM17	10 lpm XENON

EQUIPMENT IDENTIFICATION SYSTEM

First two letters XR stands for Xenon-Radon and
XRV-valve
XRR-Trap
XRP-Pump
XRL-Lucas cell
XRC-Chamber
XRB-Bottle
XRT-Tank
XRF-Freezer
XRCV-Receiver tank
XRRV-Relief valve
XGP-Gas Purifier
XP/-pressure gauge or transmitter
XT-Flow meter

NOTE:

1. OPERATING PRESSURE RANGE - 10^-6 Torr - 15 psig
2. OPERATING TEMPERATURE RANGE - 10°C TO 40°C, EXCEPT LN2 TANKS.
3. THIS GAS SYSTEM IS NOT WITHIN THE SCOPE OF TSSA, AND IS NOT REGISTERED.
4. PRESSURE REGULATOR NOT TO BE SET ABOVE 10 PSIG.
   THIS NOTE MUST ALSO BE ON REQULATOR TOO.

ISSUE	CHANGE	DATE
4A	XT-02 ADDED	JAN. 25/11
3	VACUUM CHAMBER, COLD HEAD, RTD'S DETAILS ADDED	APR. 17/09
2	VALVE XRV-46 TO XRV-49 ADDED	SEPT. 12/08
1	PRV ON GAS BOTTLES	APR. 14/08

APPROVED DATE
SUBMITTED DATE
DRAWN OLEG LI DATE

MATERIAL
DRAWN OLEG LI DATE JULY 16/07 SUBMITTED APPD
FINISH
TOL. FABRICATIONS +- 0.0625 U.N.O. MACHINED SURFACES +- 0.005 U.N.O. ANGLES +- 30' U.N.O.
SCALE ——
ALL DIMENSIONS ARE IN IMPERIAL UNITS
SNOLAB—CARLETON UNIVERSITY
OTTAWA, ONTARIO, K1S-5B6, CANADA
TITLE Xe TRAP ASSEMBLY FLOWSHEET
DRAWING NUMBER SLDO-EXO-FL-7127-01 Rev 4A
SHEET OF

Appendix B

Script for Calculating the Electrostatic Potential Using the Relaxation Method

```
% Uses the relaxation method to solve the Laplace equation in cylindrical
% coordinates.

% Inputs: none.
% Modifications required where desired, specifically to dr & dz (grid spacing)
   ,
% and maxIter (maximum number of passes through all grid points).

% Output: a grid of potentials within the rho,z space of the ESC (potential
% is rotationally symmetric about phi).
% Use ESCPotPlots.m to plot and print contour plot and log-scale plot.

% 130529 Revisions after reviewing Perl script from J. Farine

addpath([docroot '/techdoc/creating_plots/examples'])
close all
start = cputime;

dr = 0.0005; dr2 = dr^2; % 0.5mm grid spacing
```

```
19 dz = 0.0005; dz2 = dz^2;
20
21 bigR = 0.1397;      % Big radius inside ESC (meters).
22 smallR = 0.0508;    % Small radius inside ESC (meters).
23 mainR = 0.1651;     % Radius of main ESC hemisphere (meters).
24 bigGap = mainR - smallR; % Offset for small radius (smallR) in ESC.
25 smallGap = mainR - bigR;  % Offset for large radius (bigR) in ESC.
26 alBuf = 0.010;       % Buffer layer for edges of ESC.
27 diodeEdge = 0.018;  % diode edge length 18mm.
28 diodeSA = diodeEdge^2;
29 diodeR = sqrt(diodeSA/pi);  % diode is approximated to a circle for
       cylindrical ...
30 % coordinate system. Surface area is kept consistent to preserve charge
       density.
31 diodeT = 0.002;      % diode thickness
32 diodeH = 0.002;      % diode height above ESC hemisphere.
33
34 holeR = 0.03175;     % Radius of hole cut out at top of ESC (meters).
35 teflonR = 0.02875;  % Radius of teflon supporting the diode (estimate).
36 ceramicR = 12.75;    % Radius of white ceramic piece holding diode.
37 lipH = 0.0012;          % Height of lip coming at edge of ceramic.
38 lipT = 0.001;            % Thickness of lip at edge of ceramic (estimate).
39 holeH = 0.01862;     % Height of hole cut out of ESC.
40 edgeR = 0.00381;       % Rounded edge of lid inner hole, near diode.
41
42 totalWidth = mainR + alBuf;
43 totalHeight = alBuf + bigR + smallR + holeH + alBuf;
44
45 r = 0:dr:totalWidth;
46 z = 0:dz:totalHeight;
47
48 numR = length(r);
49 numZ = length(z);
50 maxIter = 10*numZ;      % MxN passes may be needed. (play with this until
       convergence is found)
51
52 % Create grid of boolean values, calcGrid, to determine whether potential is
       variable
53 % (1) or fixed (0).
54 % VGrid is initially a grid of zeros everywhere, except for 1000V at diode
55 % (set below).
56 [rGrid,zGrid] = meshgrid(r,z);
57 rGrid = rGrid';
58 zGrid = zGrid';
59 calcGrid = zeros(size(rGrid));
60 VGrid = zeros(size(rGrid));
61
62 % set calcGrid = 1 for all of ESC cavity.
63 zCavCenter = alBuf+bigR;
```

```
calcGrid( zGrid<=zCavCenter & (rGrid-smallGap).^2 + (zGrid-zCavCenter).^2 <=
    bigR^2 ) = 1;
calcGrid( zGrid>=alBuf      & zGrid<=zCavCenter & rGrid<=smallGap ) = 1;
calcGrid( (rGrid-bigGap).^2 + (zGrid-zCavCenter).^2 <= smallR^2 ) = 1;
zCavTop = alBuf+bigR+smallR;
calcGrid( zGrid>=zCavCenter & zGrid<=zCavTop & rGrid<=bigGap ) = 1;
calcGrid( zGrid>=zCavTop & zGrid<=(totalHeight-alBuf) & rGrid<=holeR ) = 1;
calcGrid( zGrid>zCavTop & zGrid<(zCavTop+edgeR) & rGrid<(holeR+edgeR) & (rGrid
    -holeR-edgeR).^2 + (zGrid-zCavTop-edgeR).^2 >= edgeR^2 ) = 1;
VGrid( zGrid>=(zCavTop+diodeH) & zGrid<=(zCavTop+diodeH+diodeT) & rGrid<=
    diodeR ) = 1000;
calcGrid( VGrid==1000 ) = 0;

drdz2 = dr*dz2;
rdz2 = r.*dz2;
rdr2 = r.*dr2;

a = (2.*rdz2) + (2.*rdr2) + drdz2;
b = rdz2 + drdz2;
c = rdz2;
d = rdr2;

initNorm = 0;
% Compute initial Norm of residual of VGrid to find a terminating condition.
for j = numZ:-1:1
    for i = 1:numR
        if calcGrid(i,j) == 1
            if r(i) == 0
                res = drdz2*(VGrid(i,j) - VGrid(i+1,j));
                initNorm = initNorm + abs(res);
            else
                res = a(i)*VGrid(i,j) - b(i)*VGrid(i+1,j) - c(i)*VGrid(i-1,j)
                    - d(i)*(VGrid(i,j+1) + VGrid(i,j-1));
                initNorm = initNorm + abs(res);
            end
        end
    end
end

epsilon = 1e-6; % Level of stability before terminating algorithm.
omega = 1; % Factor for SOR (Successive Over-Relaxation)
% Jacobi radius helps determine the next value for omega (SOR)
rJaco2 = ((cos(pi/numR) + (dr/dz)^2*cos(pi/numZ))/(1+(dr/dz)^2))^2;

% V update algorithm
for k = 1:maxIter         % main loop for number of passes through all grid
    points
    newNorm = 0;
```

```
107     for j = numZ:-1:1       % Iterate from top of ESC to bottom to start
            closer to diode
108         for i = 1:numR      % Iterate through all rho values.
109             if calcGrid(i,j) == 1 && mod(i+j,2) == mod(k,2)
110                 if r(i) == 0
111                     res = drdz2*(VGrid(i,j) - VGrid(i+1,j));
112                     newNorm = newNorm + abs(res);
113                     VGrid(i,j) = VGrid(i,j) - (omega*res/drdz2);
114                 else
115                     res = a(i)*VGrid(i,j) - b(i)*VGrid(i+1,j) - c(i)*VGrid(i
                            -1,j) - d(i)*(VGrid(i,j+1) + VGrid(i,j-1));
116                     newNorm = newNorm + abs(res);
117                     VGrid(i,j) = VGrid(i,j) - (omega*res/a(i));
118                 end
119             end
120         end
121     end
122
123     % Increase overrelaxation parameter to accelerate convergence.
124     if k == 1
125         omega = 1/(1-(rJaco2/2));
126     else
127         omega = 1/(1-(rJaco2*omega/4));
128     end
129
130     if newNorm < epsilon*initNorm, break, end
131 end
132 stop = cputime-start % display time elapsed for code to run.
```

Appendix C

Script to Rebin LabView Data

```
function [ A, B ] = rebinLabView( lv, esc )
% Bins LabView data to make it one-to-one with ESC data
% This could prove useful for finding correlations between
% LabView and ESC data, or for corrections to Count Rates.

escIVLs = length(esc.ivl);
lvFields = fieldnames(lv);
numFields = numel(lvFields);

escFields = fieldnames(esc);
numFields2 = numel(escFields);
B = esc;

% Initialize
for i = 1:numFields
    A.(lvFields{i}) = zeros(escIVLs,1);
end

% For each ESC interval, find LabView data points that fit within the
% interval.

for i = 1:escIVLs
    escStart = esc.rel_day(i) - esc.hw_day(i);
    escStop  = esc.rel_day(i) + esc.hw_day(i);
    lvStart = find( lv.rel_day > escStart, 1, 'first' );
    hLVStart = find( lv.hrel_day > escStart, 1, 'first' );

    if any(lvStart)
        lvStop = find( lv.rel_day < escStop, 1, 'last' );
        hLVStop = find( lv.hrel_day < escStop, 1, 'last' );

```

```
32          for j = 1:numFields
33              if strfind(lvFields{j}, 'h')
34                  param = mean( lv.(lvFields{j})( hLVStart:hLVStop ) );
35                  A.(lvFields{j})(i) = param;
36              else
37                  param = mean( lv.(lvFields{j})( lvStart:lvStop ) );
38                  A.(lvFields{j})(i) = param;
39              end
40          end
41
42      else
43          for j = 1:numFields
44              A.(lvFields{j}) = A.(lvFields{j})(1:i);
45          end
46
47          for j = 1:numFields2
48              B.(escFields{j}) = B.(escFields{j})(1:i);
49          end
50
51          break
52      end
53  end
```

Appendix D

RTD Locations in Vacuum Chamber

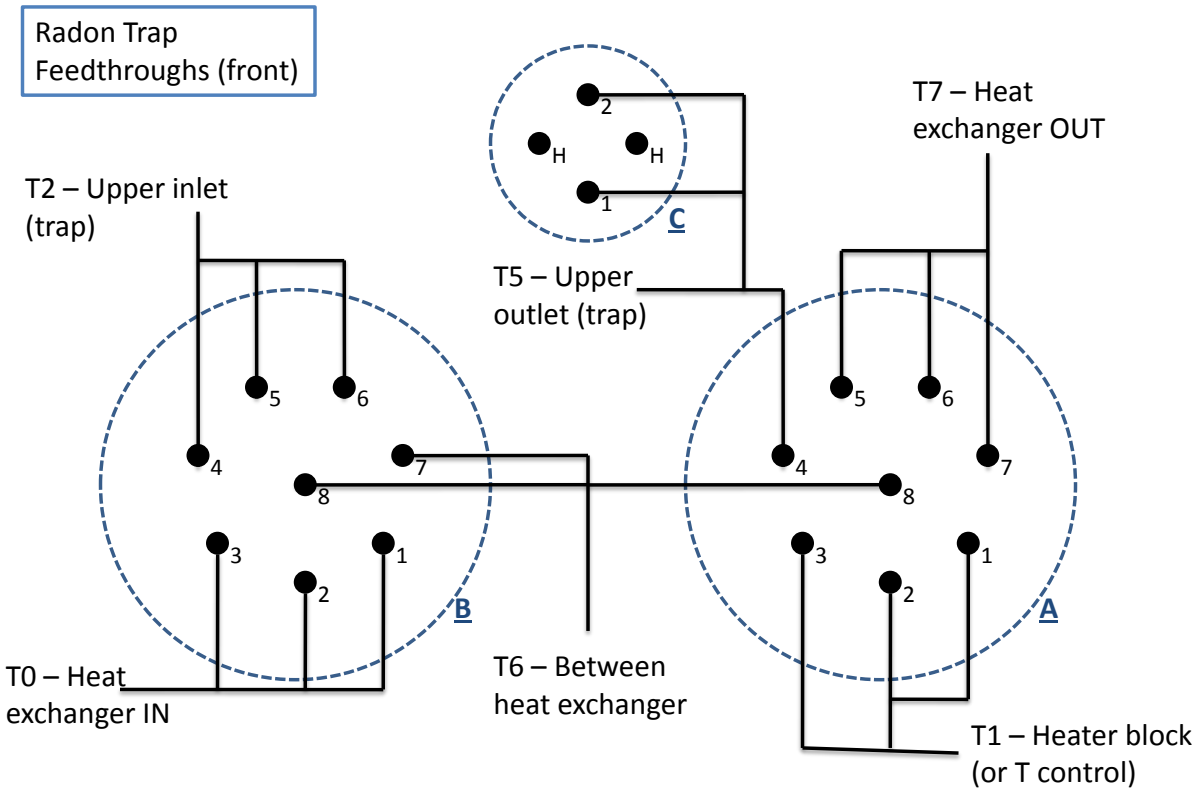

Figure D.1: Front panel of the vacuum enclosure with feedthroughs to different RTDs

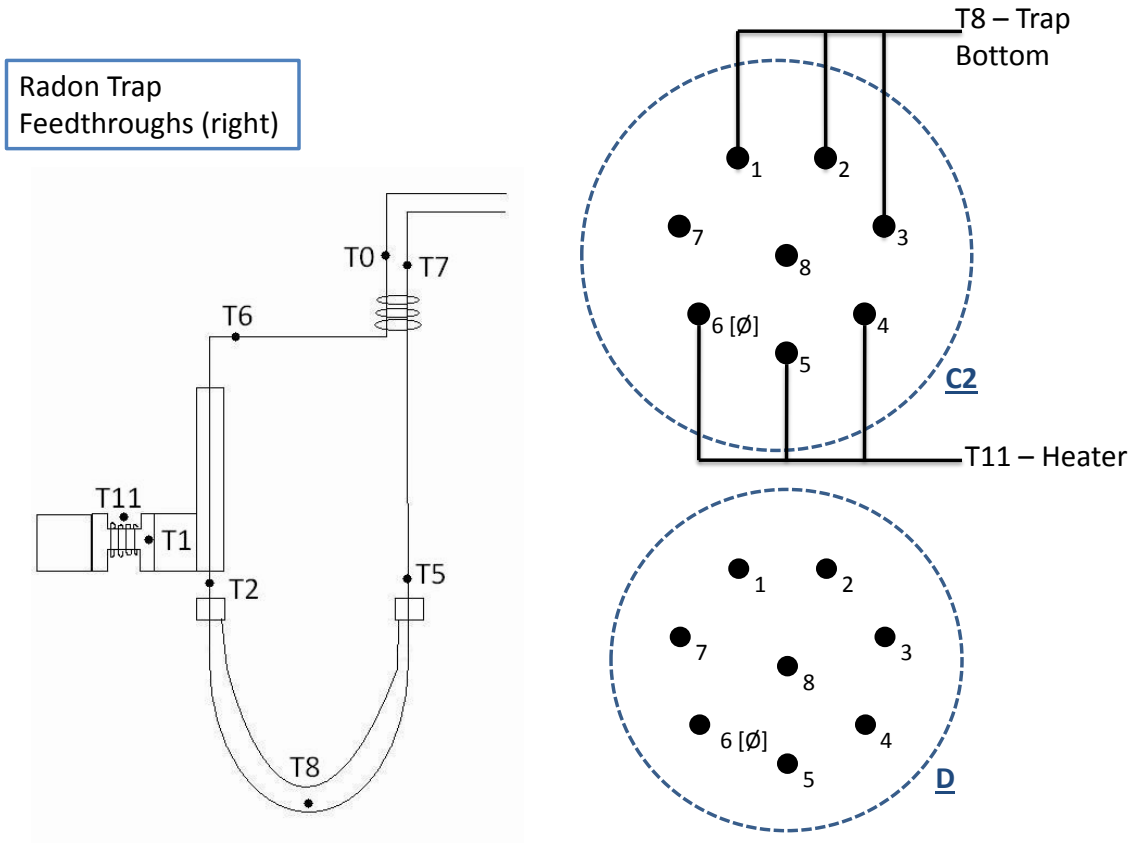

Figure D.2: Side panel of vacuum enclosure and diagram of RTD locations inside the vacuum enclosure

Appendix E

Summarized RnRun Procedures

For full, detailed procedures, see for example the eLog entry: `http://thoron.phys.laurentian.ca:8080/XeRn+INFO/35`

E.1 Start cooling and recirculating through trap at ## °C

1. Start recirculation pump.
2. Open flow through trap (open XRV-10, open XRV-11, and close XRV-9).
3. Verify that the VariAC output is ∼25 V AC (it must not exceed 28 V with current heater).
4. Set setpoint to desired temperature, ## °C.
5. Turn on refrigerator.
6. Plug heater in and start VariAC again.

E.2 Isolate trap and start counting interval

1. Isolate trap (close XRV-9, open XRV-10, and open XRV-11).
2. Stop recirculation pump.
3. Turn off refrigerator.
4. Once PID switches off, turn off VariAC.
5. Unplug heater

Appendix F

Actions Performed During RnRuns

All times were read from the wall clock, unless otherwise specified.

F.1 RnRun CuWool IV

March 14, 2011

17:43 Start recirculation pump.

17:48 Start LabView run.

17:54 High voltage applied to ESC #3, −1001 V.

17:55 ESC #3 run started, saving in 5 min intervals (**18:40** on DAQ PC).

19:47 Inject Rn.

20:28 Flow through purifier.

20:54 Re-establish normal flow.

20:55 Start cooling with setpoint −100 °C.

March 15, 2011

08:37 Change setpoint to −107.5 °C.

09:12 Throttle trap outlet (XRV-11). This was done to cause an increase in pressure through the trap, which was postulated to lead to more Rn removal, and also bring Xe pressure closer to that used in EXO-200 (∼1100 mbar).

11:20 Change setpoint to −112 °C.

11:35 Open ESC bypass valve (XRV-24). Throttle ESC inlet valve (XRV-34) until ESC flow (XT-02) reads 0.4 SLPM.

13:22 Change setpoint to −110 °C.

15:22 Stop refrigeration to warm up trap and end run.

F.2 RnRun CuWool V

April 4, 2011

17:37 ESC #3 run started, saving in 5 min intervals (**17:24** on DAQ PC).

17:46 Clocks read synchronously to be **17:46**LV = **17:34**PC (LV: LabView time, PC: DAQ PC time).

17:58 Start LabView run.

18:10 Recirculation path established. Start Rn injection.

18:28 Start flowing gas through purifier.

18:36 Start refrigerator and power heater relay and VariAC.

18:41 Set setpoint to −110 °C in LabView.

18:43 Stop flowing through purifier. Resume normal flow. Throttle ESC Inlet (XRV-34) until ESC flow (XT-02) reads 0.33 SLPM

18:50 Read 138 mV and 53 mV on controllers corresponding to pressure sensors upstream and downstream of trap (XP-18 and XP-19, respectively).

April 5, 2011

10:45 Throttle ESC Inlet (XRV-34) so that ESC flow (XT-02) increases from 0.15 SLPM to 0.33 SLPM.

11:11 Condensation point of Xe was calculated to be −109 °C based on ESC Pressure. Temperature of the heater block (T1) was deemed to be 11 °C above $T_{condensing}$. Change setpoint to −120 °C.

11:32 Xe condensing, judging by pressure drop from ESC.

11:39 Stop refrigerator. Let system warm up.

12:13 Pressure recovered in ESC. Set setpoint to −112 °C. Start refrigerator.

12:23 Close ESC Bypass (XRV-24) to force flow through ESC.

12:25 Fully open ESC Inlet (XRV-34).

15:08PC Turn XRV-11 1-3/4 turn to increase pressure in trap.

15:24PC Adjust XRV-11 from 1-3/4 to 1-1/2 turns closed to recover ESC Pressure.

April 6, 2011

15:53 Change setpoint to $-114\,^{\circ}\mathrm{C}$.

16:14 Suspect Xe condensation from drops in pressure and flows. Change setpoint to $-113\,^{\circ}\mathrm{C}$.

16:16 Stop refrigeration.

16:37 Pressure and flows have recovered; start refrigeration again.

16:57 Open ESC Bypass (XRV-24) and throttle ESC Inlet (XRV-34) until ESC Flow (XT-02) reads 0.4 SLPM (later 0.33 SLPM), similar to previous flow.

April 7, 2011

17:43 Throttle trap outlet (XRV-11) from 1-1/2 to 1-5/4.

22:06 Notice Xe started to condense not long ago.

22:09 Stop refrigeration to warm up trap and end run.

F.3 RnRun CuWool VI

May 9, 2011

15:00 Clocks read synchronously to be **15:00:18**wall = **15:00:30**LV = **14:42:25**PC (wall: wall clock time, LV: LabView time, PC: DAQ PC time).

15:03 Setpoint set to $-100\,^{\circ}\mathrm{C}$ (heater will not turn on until refrigerator brings T1 below this point; refrigerator currently OFF). PID set to K_c, T_i, T_d = 100.0, 0.001, 0.0 (P, I, and D terms respectively).

15:04 Start LabView run.

14:38PC Start ESC #3 run, saving in 5 min intervals.

15:35 Recirculation path established. Start ESC pump. XP-10 (ESC pressure) reads 1100 mbar. Pump seems noisy; stop ESC pump. De-pressurize slightly to 1000 mbar of gas.

15:39 Start ESC pump again. XP-10 returns to 1100 mbar after starting recirculation. Sounds okay.

- Flow through trap; bypass closed.
- Throttle ESC inlet valve (XRV-34) so that ESC flow (XT-02) reads 0.33 SLPM.
- Rn injection not necessary; using Rn from previous run. Proceed to purification.

16:45 Flow gas through purifier for 20 mins at 6.3 SLPM.

- Re-establish normal flow.
- Start evacuation of vacuum enclosure.

16:20 Start refrigerator, and power to heater relay and VariAC (setpoint already $-100\,^{\circ}\mathrm{C}$).

May 10, 2011

13:45 System stable from $-100\,^{\circ}\mathrm{C}$ setpoint overnight. Change setpoint to $-113\,^{\circ}\mathrm{C}$.

14:01 Throttle XRV-11 by 1-3/4 turns.

14:22 XP-10 down to 980 mbar; pressure downstream of trap (XP-19) drops from 79 mV to 66 mV, corresponding to at least 100 mbar decrease. Suspect Xe condensation. Change setpoint to $-112\,^{\circ}\mathrm{C}$.

17:22 First "flow interruption" observed, where mass flow surges abruptly, followed by sharp collapse close to zero, and recovers. Similar structures appear throughout flowmeters and temperature sensors (except for T1; only RTDs in contact with gas). Change setpoint to $-111\,^{\circ}\mathrm{C}$ in response.

18:46 Final setpoint change to $-111.5\,^{\circ}\mathrm{C}$.

19:41 System appears to be stable again.

May 11, 2011

09:00 Notice more flow interruptions having occurred overnight, at a fairly periodic rate of once every $\sim 1\frac{1}{2}$ hours.

13:17 Change setpoint to $-111.3\,^{\circ}\mathrm{C}$ to try to stop condensation.

May 12, 2011

11:19 Still more flow interruptions. Change setpoint to $-111.1\,^{\circ}\mathrm{C}$.

17:25 Change setpoint to −110.9 °C

May 13, 2011

- Flow interruptions appear to have ceased since last setpoint change. New plan is return system to initial baseline conditions to fully evaporate any ice that might still be in the trap, then approach condensation point from above.

12:09 Change setpoint to −100 °C.

May 14, 2011 - 12:09 Change setpoint to −110.9 °C.

May 15, 2011 - 12:09 Change setpoint to −111.0 °C.

May 16, 2011 - 12:09 Change setpoint to −111.1 °C.

May 17, 2011

14:04 Turn off refrigerator and power down heater to bring system back to room temperature.

14:14 Turn off Alcatel vacuum pump. Mistakenly pressurized vacuum enclosure while trap is still cold.

F.4 RnRun CuWool VII

January 27, 2012

- ESC filled with Xe through open Rn source to inject with Rn.

15:26 Start ESC #3 run, saving in 20 min intervals (**15:18**PC).

16:16 End gas purification.

16:29 Resume normal flow configuration. Fully open ESC bypass (XRV-24) and throttle ESC inlet (XRV-34) until ESC flow (XT-02) reads 0.37 SLPM. System flow (XT-01) reads 9.1 SLPM.

18:44PC Upon ESC #3 procedure failing, restart ESC #3 run.

January 30, 2012

- Connect and power heater system. Set setpoint to −100 °C. Confirm LabView PID settings are K_c, T_i, T_d = 100.0, 0.001, 0.0.

13:13 Clocks read synchronously to be **13:13:36**wall = **13:14:00**LV = **13:06:26**PC.

13:21 Start refrigerator.

14:45 Notice ESC pressure (XP-10) drop from 1180 to 1025 mbar when connecting cable for XP-05 (or from stopping vacuum pump). Reconnect XP-05 cables. XP-10 no longer jumping. XP-10 must have had a bad contact since the start of run.

18:25 Notice XP-18 and XP-19 readings are switched in LabView. Pressure upstream (XP-18) is reading lower than pressure downstream (XP-19). Switch wires going to controllers and fix labels.

January 31, 2012

17:54 Change setpoint to $-108\,^{\circ}\mathrm{C}$.

February 1, 2012

- Calculate $T_{cond} = -114\,^{\circ}\mathrm{C}$ for a trap pressure of 695 mbar (interpolated between XP-18 and XP-19).

∼10:55 Random power glitch occurs: UPS beeps briefly, lights flicker, but power returns everywhere in the system. Nothing has stopped or tripped.

10:58 Change setpoint to $-111\,^{\circ}\mathrm{C}$.

11:15 A second power glitch. Nothing in the lab has tripped. We learn later that these are SNOLAB generator tests, generally performed once a week.

11:59 Change setpoint to $-112\,^{\circ}\mathrm{C}$, after system is deemed to be fairly stable and to again approach condensation point.

February 2, 2012

10:28 Change setpoint to $-112.5\,^{\circ}\mathrm{C}$.

19:13 Change setpoint to $-113.0\,^{\circ}\mathrm{C}$.

19:20 Pressures seem to have dropped slightly since before setpoint change. XP-10 dropped by 17 ± 20 mbar ($1100 \rightarrow 1083$), XP-18 down by 9 ± 4 mbar ($932 \rightarrow 923$), and XP-19 down by 5 ± 4 mbar ($525 \rightarrow 518$). Not significant but possibly due to condensation.

- System still fairly stable to be left overnight.

February 3, 2012

- It turns out that spikes in flows, pressures, and temperatures began at some point overnight, except for T1 which is dead on setpoint at $-113.0 \pm 0.1\,^{\circ}\mathrm{C}$. Xe condensation most likely the case.

13:15 Change setpoint to $-112.5\,^{\circ}\mathrm{C}$.

17:11 System still not stable. Change setpoint to $-112.0\,^{\circ}\mathrm{C}$.

18:51 System still not stable. Turn off refrigerator to let trap warm up above condensation point (safer this way than increasing setpoint too high and risking heater failure).

19:09 Turn refrigerator back on, after T1 reaches $-105\,^{\circ}\mathrm{C}$. Setpoint now $-110.0\,^{\circ}\mathrm{C}$.

19:21 System stable again (regained steady flows, pressures, and temperatures).

19:42 Change setpoint to $-112.0\,^{\circ}\mathrm{C}$, which we know kept Xe in the gas phase before.

February 4, 2012

21:40 Turn off refrigerator to let trap warm up and end run.

F.5 RnRun CuWool VIII

February 14, 2012

10:10 Start LabView run.

10:30 Cryopump Xe, inject Rn, and return Xe into system.

11:00 Start recirculation pump with purifier open.

10:58 Turn on high voltage, set to -1001 V.

11:12 Start ESC #3 run, saving in 20 min intervals (**10:59**PC).

11:20 Close and isolate purifier.

13:32 Stop recirculation pump, after ESC saves interval 007 (**13:19**PC).

February 16, 2012

16:18PC Start recirculation pump.

- Open ESC bypass (XRV-24). Throttle ESC inlet (XRV-34) until XT-02 reads on average 0.38 SLPM.

18:10 Clocks read synchronously to be **18:10:40**wall = **18:10:32**LV = **17:58:39**PC.

February 19, 2012

- Measure resistance of the Kapton heater to be 16.0 Ω.
- Plug heater into VariAC; turn on VariAC.

20:05 Set setpoint to −100 °C.

20:10 Turn on refrigerator.

22:45 T1 reaches setpoint after $2^1/_2$ hours.

February 22, 2012

15:48 Turn off refrigerator; turn off VariAC; unplug heater. Leave system to warm up to see count rates at room temperature (recirculation still going).

February 24, 2012

13:09PC ESC #3 DAQ procedure fails.

- After inspection of HV supplies and memory in DAQ PC, everything determined to be okay.

14:15PC Start ESC #3 run.

February 27, 2012

10:02 Turn off recirculation pump. Fully open XRV-35.

F.6 RnRun CuWool IX

March 9, 2012

13:00 Cryopump Xe, inject Rn, and return Xe to 110 mbar on XP-10.

13:05 Start recirculation pump with flow bypassing Rn trap, through purifier, and through ESC (with ESC bypass also open).

13:07 Start LabView run.

13:01PC Start ESC #3 run, saving in 20 min intervals.

13:17 Clocks read synchronously to be **13:17:00**wall = **13:17:06**LV = **13:05:50**PC.

14:21PC Stop recirculation pump, after ESC saves interval 004. Close and isolate purifier.

March 12, 2012

11:32 Start recirculation pump (after ESC saves interval 207 at **10:18**PC).

March 14, 2012

9:40 Start flow through Rn Trap and close trap bypass.

9:50 Throttle ESC inlet to increase flow through ESC until XT-02 reads 0.09 LPM.

March 15, 2012

- Plug heater into VariAC, check VariAC is at notched 18 V setting, and turn on VariAC.

15:24 Turn on refrigerator (**14:12**PC). Set setpoint to −100 °C.

17:20 Heater first turns on. T1 reaches setpoint after 2 hours.

- Heater behaviour is suspect for the next hour or so. The PID is hardly turning it off at all. RTD above heater element (T11) creeping up above 100 °C

18:13 Turn off refrigerator, turn off VariAC, unplug heater, and plug VariAC into available power bar (not to relay box). Measure VariAC output to be 20.22 V AC. Increase voltage until Digital Multimeter reads 22.50 V AC.

18:20 Return VariAC to relay box, plug heater in, and turn refrigerator back on.

- Notice the PID settings were back to default values, which explains why the PID has been reacting slow all day.

18:45 Set PID gains to K_c, T_i, T_d = 100.0, 0.001, 0.0 for quicker response (these values were specified before in §7.5).

- PID cycles are now much shorter: ∼1 min on, 10 s off. T1 now finds a nice sawtooth function centered on the setpoint. Heater now declining slowly, having peaked slightly above 160 °C. System now deemed safe to leave overnight.

March 17, 2012

12:14 Isolate Rn trap. Turn off refrigerator. Wait for PID to turn heater off, then turn off VariAC, and unplug heater.

March 19, 2012

16:38 Turn off recirculation pump.

F.7 RnRun CuWool X

March 28, 2012

16:06 Cryopump Xe from system, inject Rn, and return Xe to ∼165 mbar.

16:51 Start LabView run.

16:54 Start recirculation pump, with trap, ESC and purifier all opened, and all bypasses closed.

17:30 After a proper amount of XeRn mixing, stop recirculation.

16:20PC Start ESC #3 run, saving in 20 min intervals.

17:41 Clocks read synchronously to be **17:40:35**wall = **17:42:30**LV = **16:30:50**PC

March 29, 2012

16:46PC Start recirculation just after ESC saves interval 73 (∼**18:00**LV).

- Measure 22.50 V AC coming from the VariAC. Plug heater into VariAC, turn on refrigerator, and set setpoint to −130 °C (for now).

18:23 Set setpoint to −100 °C. After consulting PT curve for 170 mbar, the goal is to approach condensation at −120 °C, but we want to first see if system is stable at −100 °C.

20:17 Change setpoint to −120 °C.

20:50 T11 plateau-ing near 155 °C, but T1 is slowly falling below setpoint.

- Several trials follow in an attempt to get T1 to stay on setpoint, and avoiding T11 from reaching our safety margin of 200 °C. This involves turning off the refrigerator and heater when T1 slips too low or T11 creeps up too high, and possibly turning up the VariAC setting. The full log entry is found on /XeRn Log/140.

21:43 Measure infinite resistance from heater; confirming it is fried following a VariAC setting change from 28.6 V AC to 33.0 V AC.

- Turn refrigerator off. Run is over until heater can be replaced.

March 31, 2012

- Finish replacing heater as specified in §7.1 and reinstalling vacuum enclosure.

14:45 Fill XeRn system to 1000 mbar with Xe.

- Restart recirculation through purifier, with ESC bypass closed.

14:50 New Rn injection made

April 1, 2012

18:17 Finish work in vacuum enclosure. Start turbomolecular pump.

18:25 Stop recirculation pump to acquire first baseline.

- Notice after leaving lab that purifier was left open (which is a known source of Rn).

April 2, 2012

13:20 Start recirculation, open purifier bypass, and close purifier.

13:46 Stop recirculation.

April 3, 2012

- Adjust VariAC to 20.36 V AC. Measure 16.5 Ω on heater. Plug in VariAC.

14:29 Start recirculation pump (just after DAQ saves interval 207 at **13:16**PC). Open ESC bypass.

14:33 Turn on refrigerator. Set setpoint to −110 °C. Turn on VariAC.

17:05 T1 first reaches setpoint.

April 4, 2012

- Pressures and flows collapsed from ice plug forming, due to heater's inability to keep up with refrigerator.
- Turn off refrigerator and VariAC to let XeRn recondense.
- Turn on refrigerator and VariAC.
- Found VariAC to be set to 18.8 V AC. Changed to 24 V AC.

∼**02:00** Different setpoints ranging from -106 to −114 °C with no success. Let system warm up before trying again.

10:56 All RTDs are now reading above 5 °C.

- Measure VariAC to be set at 25.05 V AC (1 V higher than 9 hours ago). Comment on this later.

12:05 Set setpoint to −100 °C. Turn on refrigerator.

14:26 Set setpoint to −105 °C (after T1 and T11 appear safe from previous setpoint). Estimate condensation point to be −109 °C from XP-18 and PT curve.

April 5, 2012

02:30 Set setpoint to −107 °C, watching remotely.

05:53 Set setpoint to −109 °C.

April 5, 2012

04:31 Set setpoint to −111 °C, watching remotely.

- T1 decreased by 2 °C, yet T2 dropping by ∼11 °C. Suspect Xe to be condensing (Figure 7.14).

04:55 Revert to −109 °C.

April 6, 2012

22:52 Just after DAQ saves interval 446 (**21:39**PC), isolate trap, stop recirculation, and turn off refrigeration. Once PID cycles off, also turn off VariAC.

April 9, 2012

11:05 Start recirculation, open flow through trap (with bypass closed), start refrigeration, set setpoint to −60 °C. Plug heater into VariAC and turn on VariAC.

April 10, 2012

13:11 Isolate trap, stop recirculation, turn off refrigeration, turn off heater and VariAC.

April 12, 2012

13:17 Start recirculation and open flow through trap (with bypass closed).

April 13, 2012

15:45 Stop recirculation.

F.8 RnRun CuWool XI

April 16, 2012

19:14 Cryopump Xe from system, inject Rn, and return Xe to ∼130 mbar.

19:15 Start recirculation pump, with trap, ESC and purifier all opened, and all bypasses closed.

19:20 Start LabView run.

18:10PC Start ESC #3 run, saving in 20 min intervals.

19:29 Clocks read synchronously to be **19:29:18**wall = **19:26:00**LV = **18:15:29**PC.

20:00 Isolate purifier.

20:35 Stop recirculation pump.

April 17, 2012

16:12 Start cooling and recirculating through trap at −100 °C.

18:00 T1 reaches setpoint, heater turns on.

18:05 Change setpoint to −115 °C.

18:10 Change setpoint to −120 °C. Recall that this was the setpoint that caused the heater failure in the previous run, for a pressure of 170 mbar and VariAC setting that was too high.

18:30 Heater is constantly on (not cycling off from PID), and T1 is slipping below setpoint, −120.4 °C and slowly falling.

18:38 Turn off refrigerator. Let T1 warm up to −105 °C.

19:06 Change setpoint to −110 °C.

19:23 T1 approaches −105 °C. Turn refrigerator on again.

20:03 After appearing to maintain setpoint for a few minutes, T1 starts slipping again, falling below setpoint by at least half a degree.

20:06 Turn off refrigerator. T1 still falling and accelerating.

20:20 T1 has warmed up to −95 °C. Turn on refrigerator and change setpoint to −100 °C.

20:34 T1 showing a sawtooth function along setpoint. Heater cycling on for ∼2 min, off for 5 s.

April 18, 2012

13:17 Isolate trap and start counting interval.

April 20, 2012

- Stop ESC #3 run and power down XeRn system for power outage.

F.9 RnRun CuWool XII

April 23, 2012

11:39 Inject Rn and return Xe close to 1000 mbar.

12:19 Start recirculation pump, with trap, ESC and purifier all opened, and their bypasses closed.

12:37 Start LabView run.

12:48PC Start ESC #3 run, saving in 20 min intervals.

12:50 Clocks read synchronously to be **12:49:44**wall = **12:49:44**LV = **12:53:00**PC.

13:01 Stop recirculation pump.

April 24, 2012 - 10:13 Start cooling and recirculating through trap at $-70\,^{\circ}$C.

April 25, 2012 - 10:01 Isolate trap and start counting interval.

April 26, 2012 - 10:51 Start cooling and recirculating through trap at $-60\,^{\circ}$C.

April 27, 2012 - 11:26 Isolate trap and start counting interval.

April 29, 2012 - 15:22 Start cooling and recirculating through trap at $-50\,^{\circ}$C.

April 30, 2012 - 11:26 Isolate trap and start counting interval.

May 1, 2012 - 15:07 Start cooling and recirculating through trap at $-40\,^{\circ}$C.

May 3, 2012 - 14:51 Isolate trap and start counting interval.

May 5, 2012 - 15:17 Start cooling and recirculating through trap at $-30\,^{\circ}$C.

May 6, 2012 - 13:20 Isolate trap and start counting interval.

May 8, 2012 - 13:50 Start cooling and recirculating through trap at $-20\,^{\circ}$C.

May 9, 2012 - 13:20 Isolate trap and start counting interval.

May 11, 2012 - 12:36 Start cooling and recirculating through trap at $-10\,^{\circ}$C.

May 12, 2012 - 13:41 Isolate trap and start counting interval.

May 15, 2012

13:50 Start recirculation pump and open flow through trap (open XRV-11, open XRV-10, and close XRV-9).

15:55 Isolate trap and start counting interval.

F.10 RnRun CuWool XIII

May 30, 2012

10:23 Start LabView run.

11:47 Inject Rn and return Xe close to 1000 mbar.

12:18 Start recirculation pump, with trap, ESC and purifier all opened, and their bypasses closed.

12:50 Isolate purifier (open XRV-05, close XRV-48, and close XRV-49).

12:53 Stop recirculation pump.

13:11PC Start ESC #3 run, saving in 20 min intervals.

13:01 Clocks read synchronously to be **13:00:30**wall = **12:57:00**LV = **13:01:50**PC.

May 31, 2012 - 10:15 Start cooling and recirculating through trap at $-100\,^{\circ}\mathrm{C}$.

June 1, 2012 - 10:09 Isolate trap and start counting interval.

June 4, 2012

10:56 Start recirculation and flow through trap (open XRV-11, open XRV-10, and close XRV-09).

11:37 Isolate trap (open XRV-09, close XRV-10, XRV-11) and stop recirculation.

June 5, 2012

15:10 Start recirculation. Flow through trap and purifier.

15:54 Isolate purifier and trap. Stop recirculation.

June 7, 2012 - 13:13 Start cooling and recirculating through trap at $-100\,^{\circ}\mathrm{C}$.

June 8, 2012 - 10:13 Isolate trap and start counting interval.

June 11, 2012 - 11:13 Stop ESC #3 run.